60 GHZ RSS LOCALIZATION WITH

OMNI-DIRECTIONAL AND HORN ANTENNAS

BY

FANG HONGZHAO, RAY

A THESIS SUBMITTED FOR THE DEGREE OF
MASTER OF ENGINEERING
DEPARTMENT OF ELECTRICAL AND COMPUTER ENGINEERING
NATIONAL UNIVERSITY OF SINGAPORE
2010

Acknowledgements

I express my gratitude and appreciation to all those around me who made this project possible.

First and foremost, I would like to give my sincerest thanks to my supervisor, Dr Koenraad Mouthaan for his guidance, encouragement and mind stimulating discussions during my post graduate studies. It is difficult to forget the moments when the path forward seems impossible that turned out possible with an additional nudge of faith and encouragement.

I also thank A*Star and the principal investigator, Dr, Lin Fujiang for the funding extended to this project. The project would not have been possible without the financial support.

Special thanks to my colleagues, Cao Guopeng, Ebrahim A. Gharavol and Kevin Tom, for their wisdom and counsel in driving the direction of the project.

Last, but not least, I have my family and wife to thank, who provided me stability that only a family can provide.

Contents

Acknowledgements ii

Contents…… iii

Summary…… vi

List of Tables.. viii

List of Figures ix

Chapter 1 Introduction 1

1.1 Background and need 1

1.2 Theoretical analysis 3

1.3 Purpose 5

1.4 Significance 5

1.5 Scope of this work 6

Chapter 2 System setup 7

2.1 Frequency of choice 7

2.2 Localization methods 8

2.2.1 Time of Arrival (TOA) 8

2.2.2 Time Difference of Arrival (TDOA) 8

2.2.3 Angle of Arrival (AOA) 8

2.2.4 Received Signal Strength (RSS) 9

2.3 Range of localization 9

2.4 System setup 10

2.4.1 Area of localization 10

2.4.2 Unilateral versus multilateral configuration 11

2.4.3 1.5” Wooden base 11

2.4.4 Plastic stands with 20 cm height 16

2.4.5 Siepel mm-wave absorber 17

2.5 Hardware 19

2.5.1 Transmitters and receivers 19

2.5.2 Antenna type 20

2.5.3 Baseband signal generator - FPGA development board 22

2.5.4 Data acquisition equipment 22

2.6 Software 23

Chapter 3 System architecture and localization concept 24

3.1 Localization system architecture and setup 24

3.2 Localization concept: Offline and online phase 27

3.2.1 Offline phase 27

3.2.2 Online phase 30

Chapter 4 RSS-based localization methods 32

4.1 Introduction to RSS-based localization methods 32

4.1.1 Fingerprinting 32

4.1.2 Trilateration 32

4.2 RSS-based localization methods used in this project 34

4.2.1 Method 1: Centre of Gravity (COG) 34

4.2.2 Method 2: Weighted Centre of Gravity (WCOG) 34

4.2.3 Method 3: Iterated Weighted Centre of Gravity (IWCOG) 37

4.2.4 Method 4: Removing the circle from the lowest signal 38

Chapter 5 60 GHz RSS localization with omni-directional antennas 39

5.1 Localization with two-dimensional spline in V or dBV 39

5.2 Localization with 20 cm stands 40

5.3 Localization with Siepel mm-wave absorber 44

5.4 Comparison between 20 cm stands and Siepel mm-wave absorber 48

5.5 Mean error and standard error deviation 48

5.6 Limitations 50

5.6.1 Localization speed 50

5.6.2 Localization accuracy due to multipath effects 50

5.6.3 Accuracy of measured RSS data 51

5.7 Conclusion and discussion 51

Chapter 6 60 GHz RSS localization with horn antennas – Range extension 54

6.1 Motivation 54

6.2 System architecture and localization concept 55

6.2.1 System considerations with directive antennas 55

6.2.2 Additional hardware 56

6.2.3 Range of localization 59

6.2.4 Fingerprinting method for RSS based localization with horn antennas 62

6.2.5 Baseline setup 66

6.3 Localization with three-dimensional spline in V and dBV 68
6.4 Angle of horn antennas 75
6.5 Spline versus interpolated data for look-up table 77
6.6 Localization with and without Siepel mm-wave absorber 78
6.7 Conclusion and discussion 80

Chapter 7 Conclusions and recommendations 83

Bibliography…… 89
Publications…… 93
Glossary…… 94

APPENDIX A RSS of measured and spline versus distance on 20 cm stands (V and dBV) 95
APPENDIX B Time needed for transmitters to power-up 104
APPENDIX C RSS surface plots belonging to the four transmitters mounted with AT6010H horn antennas at 45°, interpolated with a resolution of 0.5 cm from 437 measured points on a 5 cm grid 109
APPENDIX D Measured RSS surface plots of the four transmitters mounted with AT6010H horn antennas measured on a 5 cm grid 112
APPENDIX E Surface plots of measured RSS and spline-fit of the four transmitters mounted with AT6010H horn antennas at 27° (in V) 115
APPENDIX F Surface plots of measured RSS and spline-fit of the four transmitters mounted with AT6010H horn antennas at 27° (in dBV) 120
APPENDIX G Surface plots of measured RSS and spline-fit of the four transmitters on Siepel mm-wave absorber mounted with AT6010H horn antennas at 27° (in dBV) 125

Summary

Location estimation using RSSI has been attempted and studied extensively, but usually at the WiFi band, WiMax band and UWB. At 60 GHz, the studies are mostly simulations without much consideration of practical hardware constraints. In addition, the publications mainly show delay spread measurements which are only useful for systems utilizing the Time-of-Arrival (TOA), Time-Difference-of-Arrival (TDOA) and Angle-of-Arrival (AOA) methods.

This research aims to develop a 60 GHz RSS-based localization system with commercially available transmitters, receivers and antennas. Preliminary RSSI measurements are obtained with omni-directional antennas over metal, various thicknesses of wood, mm-wave absorber from Siepel and on 20 cm high plastic stands. The conditions that result in minimal RSS fluctuations are chosen for the system.

Initial development started with using omni-directional antennas at all the transmitters and receivers. Through measurements, RSS look-up tables are formed, and propagation models are created with spline approximations that represent the various transmitters. Various algorithms are developed surrounding the concept of trilateration. Together with the look-up tables, localization is shown to work at 60 GHz with mean accuracies of 2.2 cm to 3.1 cm, depending on the algorithm. The localization area is however, limited to a 60 cm by 60 cm area due to the high attenuation at this frequency.

To increase the localization area of the system, the omni-directional antennas at the transmitters are replaced with directional antennas. This modification allows localization

area to be increased to 1 m^2. The trilateration method, however, is difficult to implement because of the radiation pattern belonging the directional antennas. Thus, the fingerprinting method is used instead. Three-dimensional look-up tables are measured and surface splines are generated to represent each transmitter. During localization, these tables are sifted through to obtain the distance and position estimates. It is found that the azimuth angle of the horn antennas contributes significantly to the overall accuracy of the localization system. In addition, surface splines generated from lower resolution measurements did not result in significant degradation of localization errors. This shows measurement effort in creating the look up tables can be reduced without compromising significantly on accuracy.

The demonstrator developed in this work clearly demonstrates the feasibility of RSS localization at 60 GHz. While the system currently localizes on a planar surface, the experimental results paves the way for future development of a three-dimensional localization system.

List of Tables

Table 1: Mean errors of methods 1 to 4, measured on 20 cm stands and Siepel mm-wave absorber. 49

Table 2: Standard deviation error of methods 1 to 4, measured on 20 cm stands and Siepel mm-wave absorber.. 50

List of Figures

Figure 1.1: Growing mobile phone subscribers. 1

Figure 1.2: Comparison of attenuation at 2 GHz and at 60 GHz. 4

Figure 2.1: Oxygen absorption spectrum at 60 GHz [19]..... 7

Figure 2.2: Measured RSSI versus distance. 10

Figure 2.3: System configuration. 11

Figure 2.4: Measurement setup. 12

Figure 2.5: RSSI and corresponding residue for 0.5” thick wooden base up to 1 m in steps of 0.5 cm. 13

Figure 2.6: RSSI and corresponding residue for 1” thick wooden base up to 1 m in steps of 0.5 cm. 14

Figure 2.7: RSSI and corresponding residue for 1.5” thick wooden base up to 1 m in steps of 0.5 cm. 14

Figure 2.8: RSSI and corresponding residue for 2” thick wooden base up to 1 m in steps of 0.5 cm. 15

Figure 2.9: RSSI measured on metal and on 1.5” thick wooden base up to 1 m in steps of 0.5 cm 15

Figure 2.10: 20 cm high plastic stand. 16

Figure 2.11: RSSI measured with 20 cm high stands on 1.5” wooden base versus only on 1.5” wooden base. 17

Figure 2.12: RSSI measured with Siepel mm-wave absorber on 1.5” wooden base versus only on 1.5” wooden base. 18

Figure 2.13: Comparison of RSSI measured with Siepel mm-wave absorber and 20 cm stands on 1.5” wooden base. 19

Figure 2.14: (a) Flann MD249 omni-directional antenna (b) corresponding radiation pattern. 20

Figure 2.15: Quinstar QWA-15 waveguide to coaxial adaptor. 21

Figure 2.16: Comotech (a) receiver and (b) transmitter tuned to 60.5 GHz mounted with MD249 omni-directional antennas. 21

Figure 2.17: Xilinx ML523 FPGA development board. 22

Figure 2.18: Data acquisition equipment (a) Agilent U2352A IO board (b) U2902A interface board. 22

Figure 3.1: System architecture block diagram. 25

Figure 3.2: Localization system. 26

Figure 3.3: Localization setup with 20 cm high stands and 1.5” thick wooden base. 26
Figure 3.4: Localization setup on Siepel mm-wave absorber and 1.5” thick wooden base. 27
Figure 3.5: Measured RSS and spline-fit of TX1 (in V) on 20 cm stands with inset showing the expected distance error. 28
Figure 3.6: Measured RSS and spline-fit of TX1 (in dBV) on 20 cm stands with inset showing the expected distance error. 29
Figure 3.7: Timing diagram of the online phase. 31
Figure 4.1: Ideal case of trilateration. 33
Figure 4.2: Non-ideal case of trilateration. 33
Figure 4.3: Centre of gravity (COG) method of four intersecting circles. 34
Figure 4.4: Weighted COG method of circles estimated by TX1, TX2 and TX3. 35
Figure 4.5: Weighted COG method of circles estimated by TX2, TX3 and TX4. 36
Figure 4.6: Weighted COG method of circles estimated by TX1, TX3 and TX4. 36
Figure 4.7: Weighted COG method of circles estimated by TX1, TX2 and TX4. 37
Figure 4.8: Final position, P, composed from the four points acquired by weighted COG. 37
Figure 5.1: Error CDF of method 1 on 20 cm stands using splines derived from measured RSS in V and dBV. 40
Figure 5.2: Vector plot of localization error on 20 cm stands using method 1. 41
Figure 5.3: Vector plot of localization error on 20 cm stands using method 2. 42
Figure 5.4: Vector plot of localization error on 20 cm stands using method 3. 42
Figure 5.5: Vector plot of localization error on 20 cm stands using method 4. 43
Figure 5.6: Error CDFs of the four methods on 20 cm stands. 43
Figure 5.7: Vector plot of localization error on Siepel mm-wave absorbers using method 1. 45
Figure 5.8: Vector plot of localization error on Siepel mm-wave absorbers using method 2. 46
Figure 5.9: Vector plot of localization error on Siepel mm-wave absorbers using method 3. 46
Figure 5.10: Vector plot of localization error on Siepel mm-wave absorbers using method 4. 47
Figure 5.11: Comparing the error CDFs of the four methods on Siepel mm-wave absorber. 47

Figure 5.12: Error CDFs of method 3 on 20 cm stands and Siepel mm-wave absorber. 48

Figure 5.13: Mean and standard deviation error of the four methods on 20 cm stands and Siepel mm-wave absorber. 49

Figure 6.1: AT6010H horn antenna from Comotech. (a) top-view (b) WR-15 mount (c) front view. 56

Figure 6.2: Radiation pattern of AT6010H Horn antenna supplied by Comotech. 57

Figure 6.3: (a) Mis-alignment of receiver and transmitter antennas (b) After rectification. 58

Figure 6.4: Final setup with Siepel mm-wave absorbers. 59

Figure 6.5: RSS plot interpolated from 437 measurements with a resolution of 0.5 cm. (a) Surface plot of TX3 at an angle of 45° in V interpolated from measured RSS values (inset) (b) top-view. 61

Figure 6.6: (a) 3D spline-fitted surface plot of TX3 at an angle of 45° (b) Top view. 66

Figure 6.7: (a) 3D surface plot of TX3's measured RSSI at an angle of 27° in V (b) Top view (c) Spline-fitted curve (d) Top view of spline. 70

Figure 6.8: (a) 3D surface plot of TX3's measured RSSI at an angle of 27° in dBV (b) Top view of spline (c) Spline-fitted curve (d) Top view of spline. 72

Figure 6.9: Plot of mean distance error, standard deviation and maximum distance error of localization using a look-up table derived from measured RSS values in dBV and V. 73

Figure 6.10: Error CDF of localization from using a look-up table derived from measured RSS in dBV and V. 74

Figure 6.11: Plot of mean distance error, standard deviation and maximum distance error of localization with direction of horn antennas at 27° and 45°. 76

Figure 6.12: Error CDF of localization with horn antennas directed 27° and 45° from the axis on the left of each transmitter. 76

Figure 6.13: Error CDF of localization from using look-up tables derived from RSS values measured on 5 cm grid (21 x 21 values), 10 cm grid (11 x 11 values) and 20 cm grid (6 x 6 values). 78

Figure 6.14: Plot of mean distance error, standard deviation and maximum distance error of localization with and without Siepel mm-wave absorbers. 79

Figure 6.15: Error CDF of localization with and without Siepel mm-wave absorbers. 80

Figure A.1: Measured RSS and spline-fit of TX1 in V on 20 cm stands with inset showing the expected distance error. 95

Figure A.2: Measured RSS and spline-fit of TX2 in V on 20 cm stands with inset showing the expected distance error. 96

Figure A.3: Measured RSS and spline-fit of TX3 in V on 20 cm stands with inset showing the expected distance error. 96
Figure A.4: Measured RSS and spline-fit of TX1 in V on 20 cm stands with inset showing the expected distance error. 97
Figure A.5: Measured RSS and spline-fit of TX1 in dBV on 20 cm stands with inset showing the expected distance error. 97
Figure A.6: Measured RSS and spline-fit of TX2 in dBV on 20 cm stands with inset showing the expected distance error. 98
Figure A.7: Measured RSS and spline-fit of TX3 in dBV on 20 cm stands with inset showing the expected distance error. 98
Figure A.8: Measured RSS and spline-fit of TX4 in dBV on 20 cm stands with inset showing the expected distance error. 99
Figure A.9: Measured RSS and spline-fit of TX1 in V on Siepel mm-wave absorbers with inset showing the expected distance error. 99
Figure A.10: Measured RSS and spline-fit of TX2 in V on Siepel mm-wave absorbers with inset showing the expected distance error. 100
Figure A.11: Measured RSS and spline-fit of TX3 in V on Siepel mm-wave absorbers with inset showing the expected distance error. 100
Figure A.12: Measured RSS and spline-fit of TX4 in V on Siepel mm-wave absorbers with inset showing the expected distance error. 101
Figure A.13: Measured RSS and spline-fit of TX1 in dBV on Siepel mm-wave absorbers with inset showing the expected distance error. 101
Figure A.14: Measured RSS and spline-fit of TX2 in dBV on Siepel mm-wave absorbers with inset showing the expected distance error. 102
Figure A.15: Measured RSS and spline-fit of TX3 in dBV on Siepel mm-wave absorbers with inset showing the expected distance error. 102
Figure A.16: Measured RSS and spline-fit of TX4 in dBV on Siepel mm-wave absorbers with inset showing the expected distance error. 103
Figure B.1: Test points A, B and C to determine time needed for transmitter to turn on. 104
Figure B.2: Time needed for digital signal to reach power switches. 105
Figure B.3: Total time needed for 5 V supply to reach transmitters. 106
Figure B.4: Total time needed to power-up TX1. 107
Figure B.5: Total time needed to power-up TX2. 107
Figure B.6: Total time needed to power-up TX3. 108
Figure B.7: Total time needed to power-up TX4. 108

Figure C.1: Interpolated surface plot of TX1's measured RSS at an angle of 45° in V. Inset shows top view. 109

Figure C.2: Interpolated surface plot of TX2's measured RSS at an angle of 45° in V. Inset shows top view. 110

Figure C.3: Interpolated surface plot of TX3's measured RSS at an angle of 45° in V. Inset shows top view. 110

Figure C.4: Interpolated surface plot of TX4's measured RSS at an angle of 45° in V. Inset shows top view. 111

Figure D.1: Surface plot of TX1's measured RSS at an angle of 45° in V. 112

Figure D.2: Surface plot of TX2's measured RSS at an angle of 45° in V. 113

Figure D.3: Surface plot of TX3's measured RSS at an angle of 45° in V. 113

Figure D.4: Surface plot of TX4's measured RSS at an angle of 45° in V. 114

Figure E.1: Surface plot of TX1's measured RSS at an angle of 27° in V. Inset shows top view. 115

Figure E.2: Surface plot of TX2's measured RSS at an angle of 27° in V. Inset shows top view. 116

Figure E.3: Surface plot of TX3's measured RSS at an angle of 27° in V. Inset shows top view. 116

Figure E.4: Surface plot of TX4's measured RSS at an angle of 27° in V. Inset shows top view. 117

Figure E.5: Spline-fit of TX1's measured RSS at an angle of 27° in V. Inset shows top view. 117

Figure E.6: Spline-fit of TX2's measured RSS at an angle of 27° in V. Inset shows top view. 118

Figure E.7: Spline-fit of TX3's measured RSS at an angle of 27° in V. Inset shows top view. 118

Figure E.8: Spline-fit of TX4's measured RSS at an angle of 27° in V. Inset shows top view. 119

Figure F.1: Surface plot of TX1's measured RSS at an angle of 27° in dBV. Inset shows top view. 120

Figure F.2: Surface plot of TX2's measured RSS at an angle of 27° in dBV. Inset shows top view. 121

Figure F.3: Surface plot of TX3's measured RSS at an angle of 27° in dBV. Inset shows top view. 121

Figure F.4: Surface plot of TX4's measured RSS at an angle of 27° in dBV. Inset shows top view. 122

Figure F.5: Spline-fit of TX1's measured RSS at an angle of 27° in V. Inset shows top view. 122
Figure F.6: Spline-fit of TX2's measured RSS at an angle of 27° in V. Inset shows top view. 123
Figure F.7: Spline-fit of TX3's measured RSS at an angle of 27° in V. Inset shows top view. 123
Figure F.8: Spline-fit of TX4's measured RSS at an angle of 27° in V. Inset shows top view. 124
Figure G.1 Surface plot of TX1's measured RSS on Siepel mm-wave absorber at an angle of 27° in dBV. Inset shows top view. 125
Figure G.2 Surface plot of TX2's measured RSS on Siepel mm-wave absorber at an angle of 27° in dBV. Inset shows top view. 126
Figure G.3 Surface plot of TX3's measured RSS on Siepel mm-wave absorber at an angle of 27° in dBV. Inset shows top view. 126
Figure G.4 Surface plot of TX4's measured RSS on Siepel mm-wave absorber at an angle of 27° in dBV. Inset shows top view. 127
Figure G.5 Spline-fit of TX1's measured RSS on Siepel mm-wave absorber at an angle of 27° in dBV. Inset shows top view. 127
Figure G.6 Spline-fit of TX2's measured RSS on Siepel mm-wave absorber at an angle of 27° in dBV. Inset shows top view. 128
Figure G.7 Spline-fit of TX3's measured RSS on Siepel mm-wave absorber at an angle of 27° in dBV. Inset shows top view. 128
Figure G.8 Spline-fit of TX4's measured RSS on Siepel mm-wave absorber at an angle of 27° in dBV. Inset shows top view. 129

Chapter 1 Introduction

1.1 Background and need

There are two major communication trends that are influencing the wireless industry today. First, wireless has become an integral part of everyday life, among consumers and businesses. For example, as shown in Figure 1.1, the number of new mobile phone subscribers grew 1 billion from year 2005 to 2007 [1].

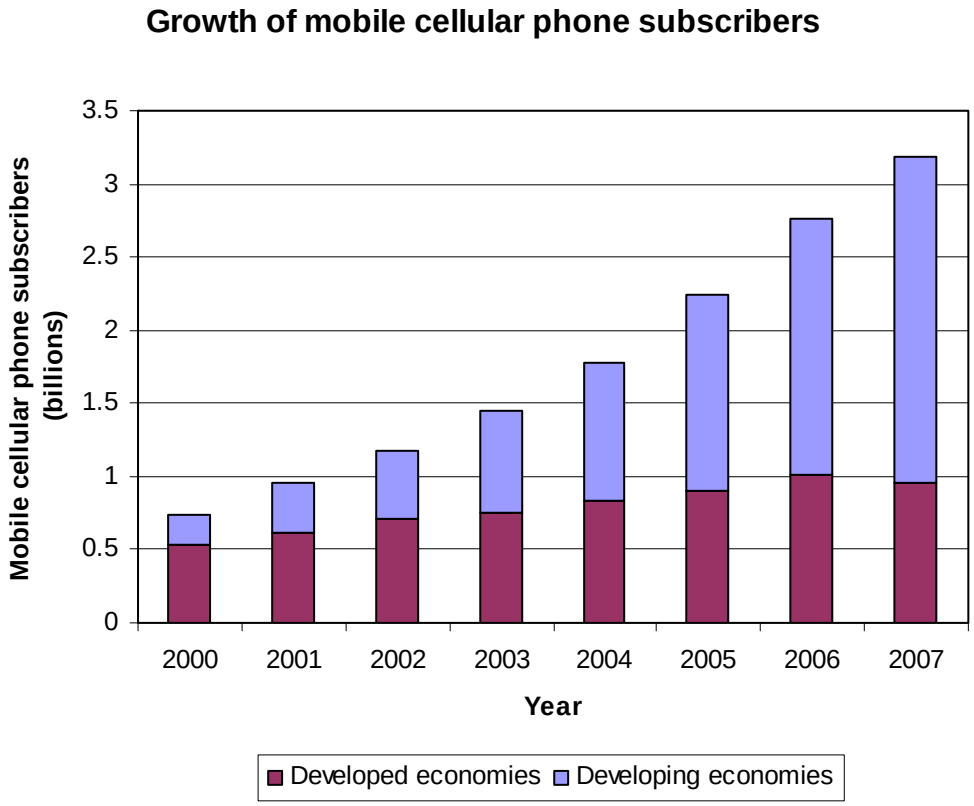

Figure 1.1: Growing mobile phone subscribers [1].

Second, with the ever increasing high definition video, automotive radar and high resolution imaging markets, there is a need for very large bandwidths, low cost and low power wireless devices. However, conventional Wi-Fi available today has a maximum data rate of 54 Mbps. The most recent release of 802.11n has a maximum data rate of 600

Mbps using MIMO techniques [2]. UWB technology, as an alternative is limited to data rates of only 480 Mbps due to the lower transmit power. Such data rates are insufficient, for high definition television (HDTV) streaming at about 2 Gbps, as discussed in IEEE 802.15.3c [3]. Hence, in order to satisfy the future need for speed, capacity and security, new mm-wave solutions are required.

The 60 GHz band has unique characteristics that make it significantly different from traditional 2.4 GHz and 5 GHz license free bands and other licensed bands.

Some unique characteristics include:

- 20 to 40 dB increased path loss due to the high frequency.
- 10 to 30 dB/km atmospheric absorption, depending on atmospheric conditions.
- Low multipath effects in the outdoor environment.
- Large bandwidth allocated: 57 – 64 GHz in US and Korea, 59 – 66 GHz in Europe and Japan.
- Unlicensed.
- High transmit powers up to 40 dBm.
- Less interference because there are fewer applications in that spectrum.

Some of these characteristics translate to the following advantages [4]:

- Decreased interference due to the high attenuation in space which results in greater security and greater frequency reuse.
- Robust against fog, as compared to optical technology.
- Cheap and fast implementation as there are no licensing costs.
- Data rates larger than 1 Gbps are feasible.

- Ability to exploit high antenna directivity to obtain larger distance and higher interference immunity.

However, the unique characteristics also imply various disadvantages:

- NLOS (Non-Line-Of-Sight) communications are difficult due to decreased multipath.
- Internationally inconsistent allocated bands.

1.2 Theoretical analysis

The additional 10 to 30 dB path loss per kilometer encountered at 60 GHz is theoretically proven by a modified Friis path loss equation to model 60 GHz wave propagation [5]:

$$P_r(dBm) = -32.4 - 30\alpha + P_t + G_t + G_r - 10\alpha \log_{10} d - 20\log_{10} f - \gamma d \qquad (1)$$

where α = 2.2

γ = 15.09 dB/km

P_t = transmitted power (dBm)

G_t, G_r = gains of the transmitting and receiving antennas (dBi) respectively

d = distance (km)

f = frequency (GHz)

On the assumption of a transmitted power of 30 dBm and unity gain antennas at 2 GHz and 60 GHz, the expected power received from 10 cm to 100 cm are plotted in Figure 1.2. The 60 GHz signal is observed to exhibit an additional attenuation of approximately 30 dB due to the high frequency. This 30 dB difference increases when the distance increases due to the additional oxygen attenuation.

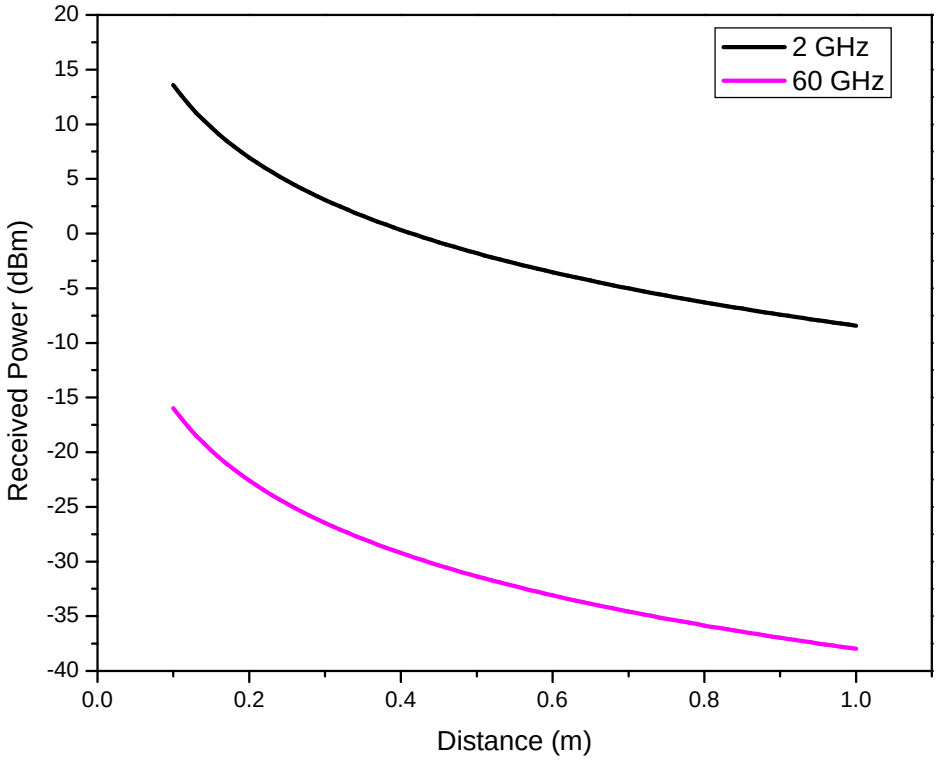

Figure 1.2: Comparison of attenuation at 2 GHz and at 60 GHz.

Millimeter-wave frequencies are attractive because of its high data rate as implied by Shannon's Law:

$$C = BW.\log_2(1+SNR) \tag{2}$$

Where C = channel capacity (bps)

BW = bandwidth (Hz)

SNR = Signal-Noise Ratio

Shannon's law shows that the data rate can be increased by increasing the bandwidth and/or the SNR. Bandwidth is readily available at the V-band where there are less applications and a 7 GHz bandwidth has been allocated by the FCC. Hence, data transmission in the V-band can provide higher data rates.

The data rate is also affected by the overall SNR. At 60 GHz, received signals suffer from greater attenuation due to the high frequency and additional oxygen absorption, resulting

in a lower SNR. However, the larger attenuation also reduces the level of interferences as well as multi-path effects, hence, balancing out the SNR. These reasons show the potential for short range, high speed wireless communications at millimeter wave frequencies.

1.3 Purpose

As part of a larger project to develop an “Intelligent mm-wave platform for home entertainment and assistive technology”, a working localization system at 60 GHz was required to be built and implemented. The platform uses a single localization scheme and is meant as a first step towards a system to wirelessly perform localization and monitor the large number of health parameters of elderly people in an indoor environment. The realistic system though, should finally incorporate multiple localization schemes that are complementary. In addition, it can potentially provide real-time gigabit-rate connection between different home appliances and for interactive gaming.

1.4 Significance

Localization at mm-wave frequencies is challenging and under-researched. Few papers have been published with measured results of the wave propagation characteristics at 60 GHz [6]-[8]. If available, they only show measured results starting from 1 meter [9], [10]. While many localization attempts have been made in the Wi-Fi band, WiMax band and UWB [11]-[14], few attempts have been made to localize at 60 GHz. Moreover, these attempts offer results mainly from simulations with few hardware constraints [15]-[16]. Thus, more empirical results and studies are critical for developing useful wireless

applications utilizing RSSI.

1.5 Scope of this work

The potential of utilizing the 60 GHz band for high speed wireless communications and localization provides the impetus for further research in this frequency band. As previously stated, studies in using RSSI at the 60 GHz band have been limited. Thus, this work focuses on developing a RSS-based localization system operating at 60 GHz. First, the relationship between distance and RSSI readings is established through measurements and modeling using a transmitter and receiver pair mounted with omni-directional antennas. The effects of fading due to reflections can be seen in the RSSI data. A couple of attempts are made to mitigate these effects with significant improvements. Consequently, localization is optimized with various trilateration methods and results presented.

In the event of range extension, the omni-directional antennas at the transmitters are changed to directional antennas. The relationship between distance and RSSI readings has to be re-established and modeled. In the process, other critical issues arise and are mitigated. Localization is attempted with the fingerprinting method and results are presented.

Chapter 2 System setup

2.1 Frequency of choice

Many atmospheric studies have been performed using microwave temperature profilers (MTP), studying wave propagation characteristics in the 60 GHz spectrum [17]-[19]. The oxygen absorption spectrum shown in Figure 2.1 was reported in [19]. It illustrates the attenuation of mm-waves due to oxygen at various altitudes. Maximum wave absorption of 15.2 dB/km (3.5 Np/km) is observed at approximately 60.5 GHz. Since the additional attenuation provides many added advantages, this will be the centre frequency of the localization system to be developed.

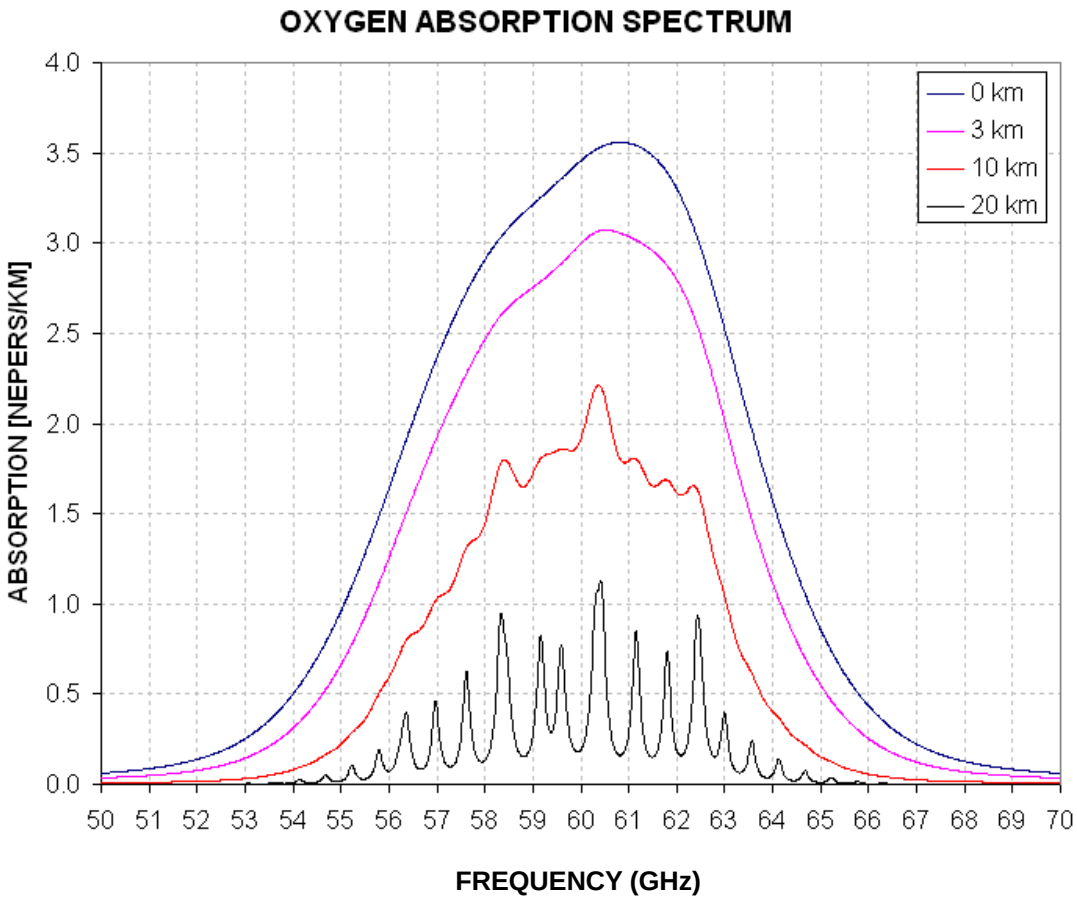

Figure 2.1: Oxygen absorption spectrum at 60 GHz [19].

2.2 Localization methods

Methods for localization are: Time of Arrival (TOA), Time-Difference of Arrival (TDOA), Angle of Arrival (AOA) and Received Signal Strength (RSS). These methods are reviewed briefly in the following subsections.

2.2.1 Time of Arrival (TOA)

The TOA method uses the transit time between transmitter and receiver directly to find the distance [20]. The distance is obtained by multiplying the speed of wave propagation with the time taken for the signal to reach the receiver. Therefore, precise clock synchronization becomes critical for a reliable TOA measurement. This can require expensive hardware and complex signal processing.

2.2.2 Time Difference of Arrival (TDOA)

The TDOA method calculates the location from the differences of the arrival times measured on pairs of transmission paths between the target and fixed terminals [20]. Similar to the TOA method, precise clock synchronization is also needed, which may require expensive hardware and complex processing methods.

2.2.3 Angle of Arrival (AOA)

An AOA measurement provides the angle of the incoming signal, rather than range information. This method does not require clock synchronization. However, it requires an antenna array with directivity operating at 60 GHz which is commercially unavailable.

2.2.4 Received Signal Strength (RSS)

The RSS-based approach uses the relationship between RSS and distance to estimate the distance between the transmitter and the receiver. This method is advantageous because it can be easily implemented without additional hardware, timing synchronization issues and complex algorithms. Only the ability to read the RSSI (Received Signal Strength Indicator) on the receiver and a location estimation program to interpret the reading is required.

A main disadvantage of this method is its large variation in signal strength due to interference and multipath effects especially at long distances.

The RSS method is also location specific, and its accuracy will depend on how well the location estimation program is tailored to the place where the system is being used.

RSS localization utilizes much simpler algorithms and relatively inexpensive hardware. In order to limit the scope of the project and to align it with the delivery schedule, this dissertation will focus on RSS localization.

2.3 Range of localization

For the RSS method of localization, the distance information is contained in the relationship between RSS and the distance between transmitter and receiver. This information reduces when the gradient reduces. Figure 2.2 shows the measured relationship between RSS and distance of a typical transmitter-receiver pair with omni-directional antennas. It is observed that the RSS attenuates quickly within the first 20 cm and gradually tapers off beyond 60 cm. While the steep RSS gradient below 20 cm

provides good localization accuracy, the flatter RSSI values beyond 80 cm contain little distance information. It is also in this region that the RSS experiences the constructive and destructive interference from the direct wave and an indirect wave. This can corrupt distance estimation. The localization system developed here is limited to distances up to 80 cm.

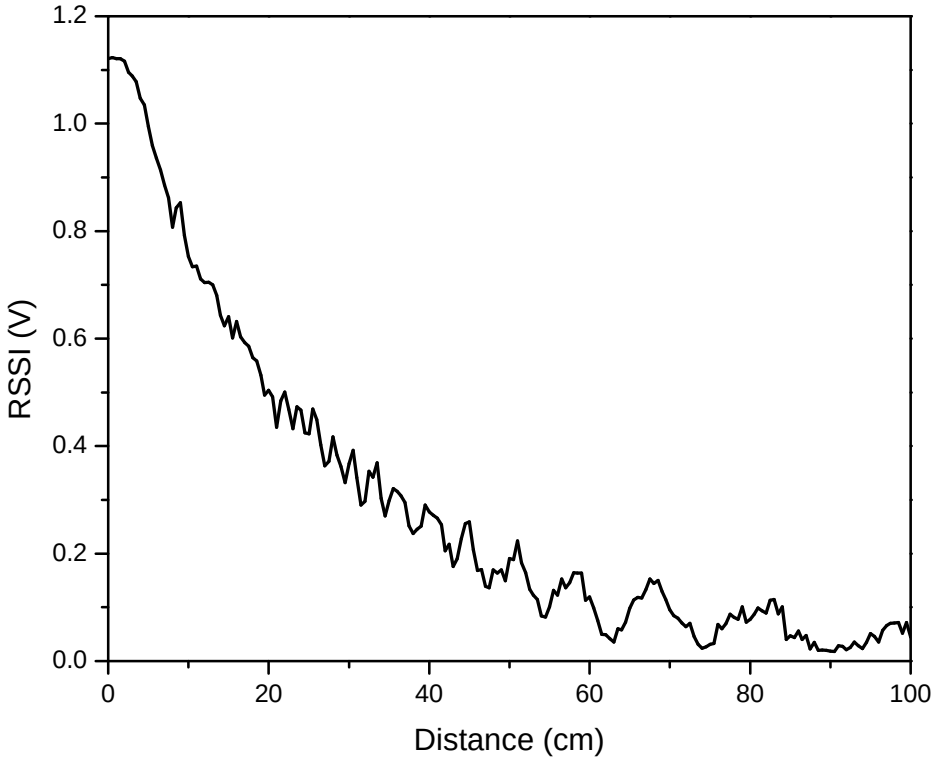

Figure 2.2: Measured RSSI versus distance.

2.4 System setup

2.4.1 Area of localization

Because the range of localization is up to 80 cm, a system of four transmitters or receivers will be capable of performing localization when placed at the four corners of a 60 cm by 60 cm square area, as inferred from the Pythagoras theorem.

2.4.2 Unilateral versus multilateral configuration

In a multilateral configuration, the target is a transmitter whose location is calculated from the RSSI values of multiple receivers with known positions. In a unilateral configuration a receiver receives signals from multiple transmitters with known positions and calculates its location.

For data transmission, the 60 GHz transmitters used in this project require a data input larger than 200 Mbps. Because the transmitters are driven by an FPGA, it is impractical to implement the multilateral configuration.

Therefore, the unilateral configuration is implemented in this work. The system consists of four transmitters, fixed at the four corners of a 60 cm by 60 cm square area with the receiver in the square. The configuration is shown in Figure 2.3.

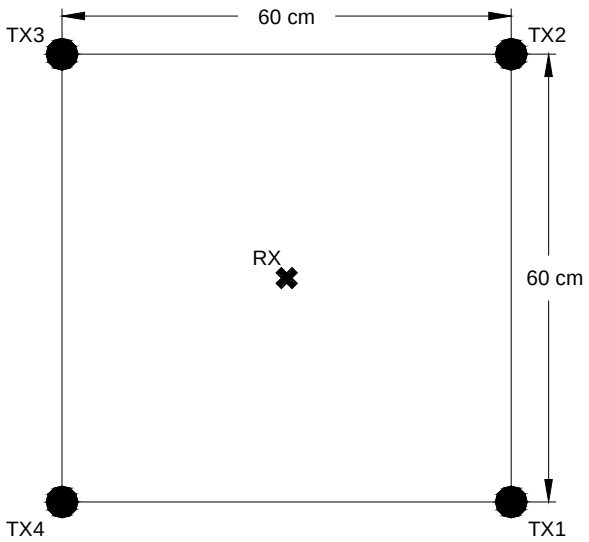

Figure 2.3: System configuration.

2.4.3 1.5” Wooden base

In order to reduce multipath effects, a wooden base is used in the experiments. Wood

provides 20 to 40 dB of absorption at 60 GHz depending on the thickness [21]-[23]. Thus, thick wood may provide a base to ensure consistent signal propagation characteristics.

Experiments were conducted to determine the required thickness. The same TX-RX pair is measured on a wooden base with a thickness of 0.5”, 1”, 1.5” and 2”. Each measurement was performed twice: once on a formica-laminated table and another with a metal (aluminium) sheet in-between the wooden base and the formica-laminated table. This forms two RSS curves for each wooden base where the difference is related to the amount of reflections that arise from the aluminium sheet below the wooden base. Thus, the ideal thickness will result in minimal difference between the two RSS curves. The measurement setup is shown in Figure 2.4.

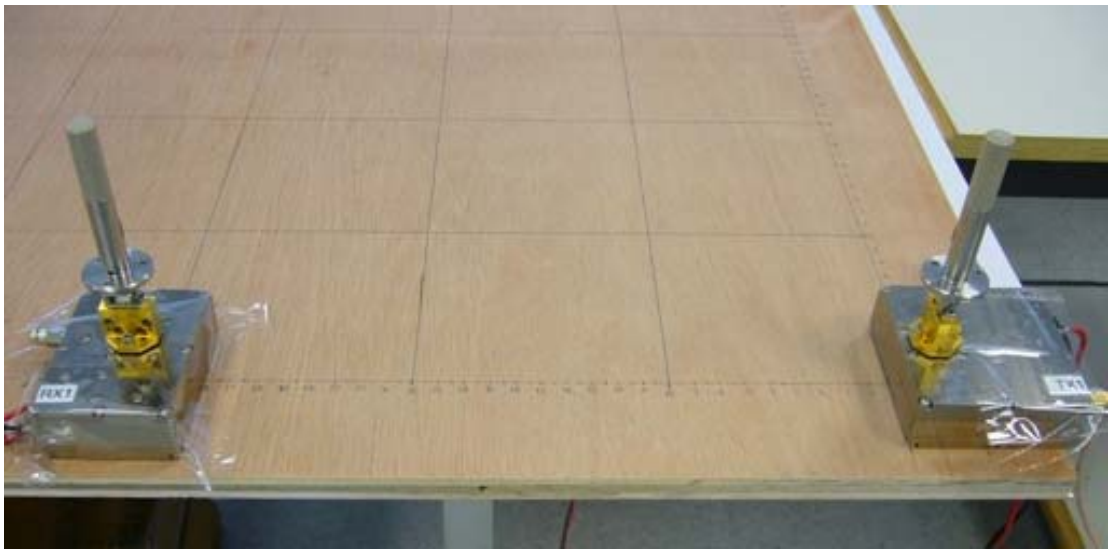

Figure 2.4: Measurement setup.

The measured RSSI values for the four thicknesses are shown in Figures 2.5 to 2.8. Each plot shows the RSSI values with and without the metal sheet. The optimum wooden base should display no significant change in RSSI when the metal sheet is inserted.

In the same figures, the residue of the RSSI for each wood thickness with and without the

metal sheet is shown. For thicknesses of 0.5” and 1”, significant residue is observed. For thicknesses of 1.5” and 2”, residue is observed to be minimal when a metal sheet is inserted. Since there is no significant advantage of using the thicker base when the 1.5” thick base suffices, the wooden base of 1.5” is used.

Figure 2.9 shows a comparison of RSS measurements on metal with and without the 1.5” thick wooden base. It highlights the severity of signal fluctuations on metal beyond a distance of 20 cm resulting from multipath effects caused by the aluminium sheet’s highly reflective surface.

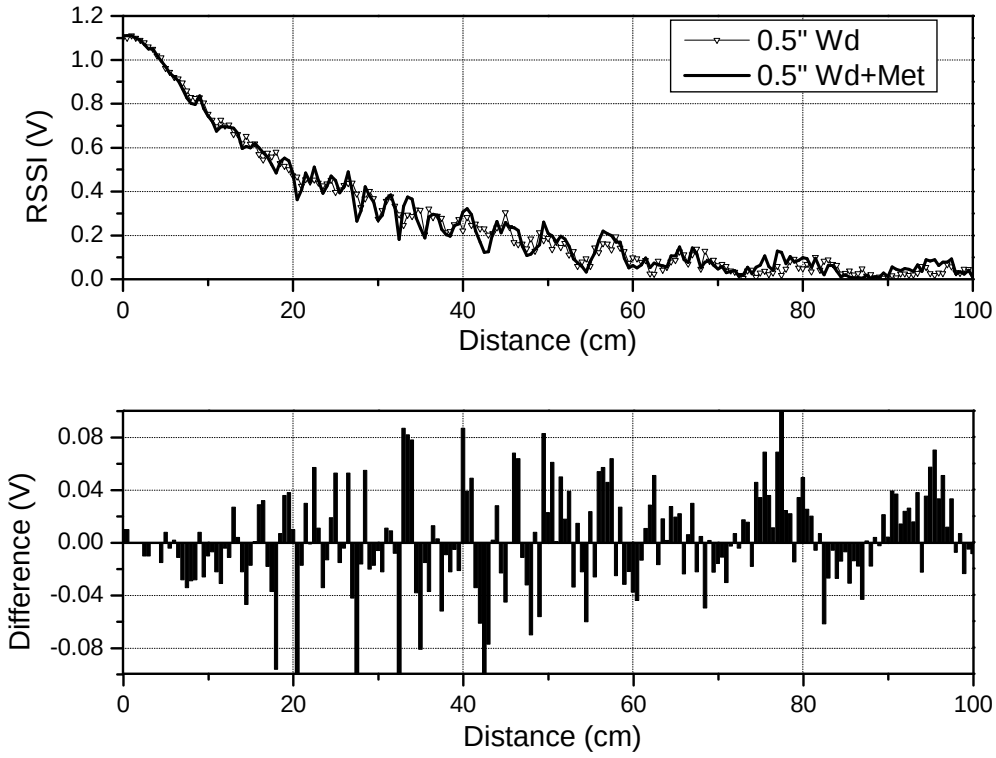

Figure 2.5: RSSI and corresponding residue for 0.5” thick wooden base up to 1 m in steps of 0.5 cm.

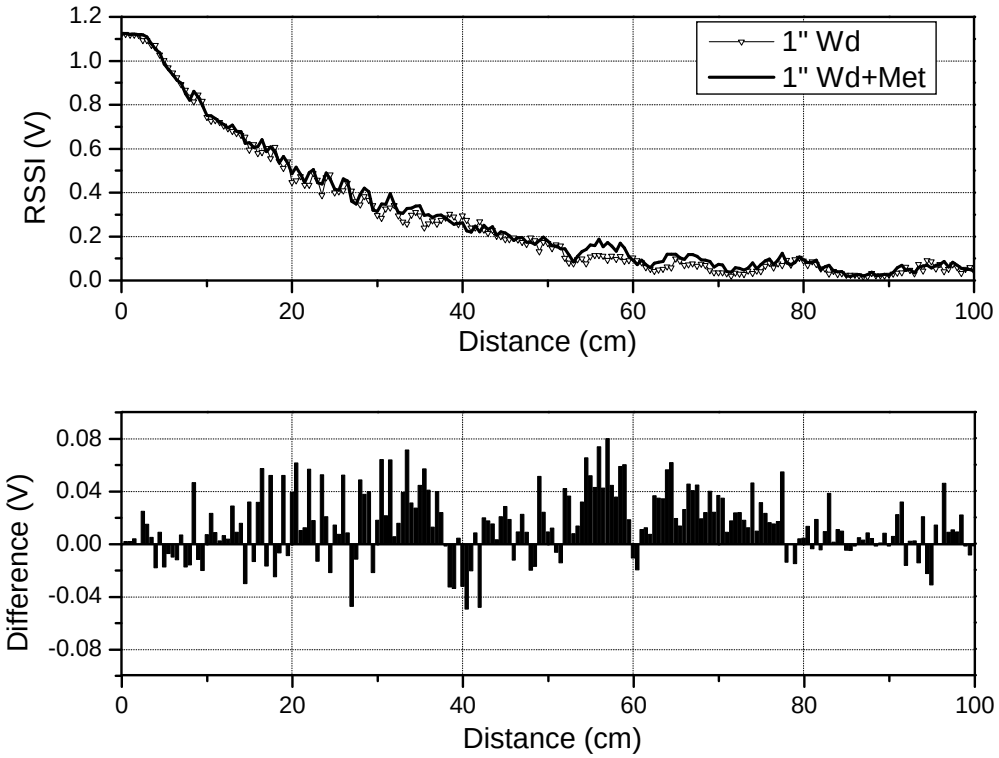

Figure 2.6: RSSI and corresponding residue for 1” thick wooden base up to 1 m in steps of 0.5 cm.

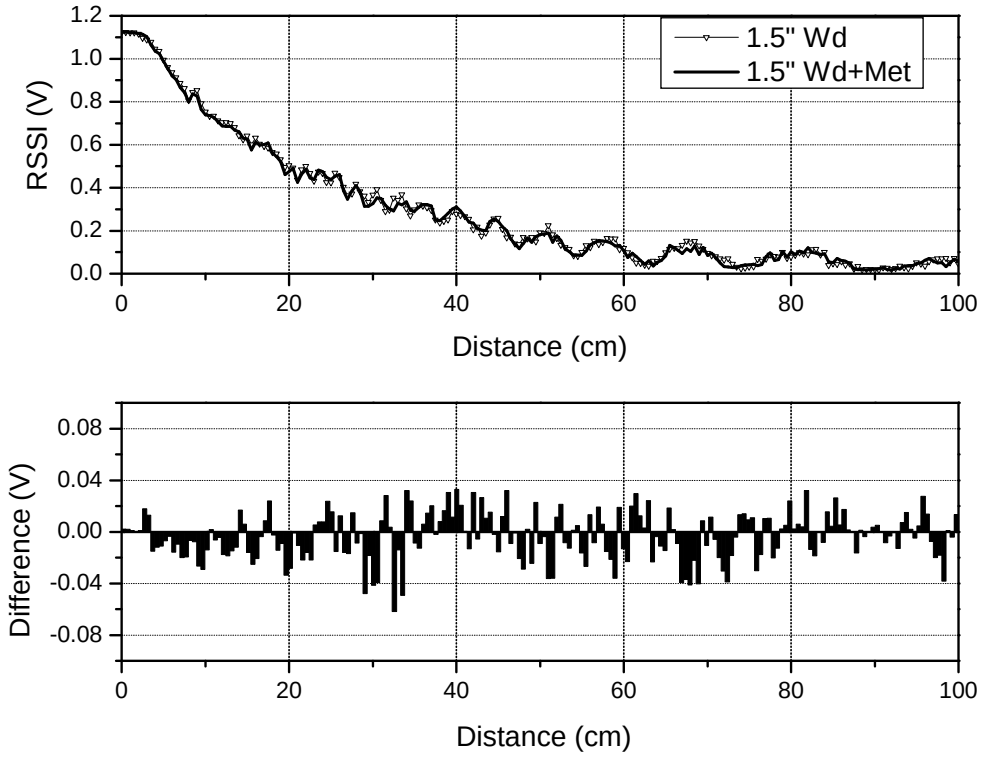

Figure 2.7: RSSI and corresponding residue for 1.5” thick wooden base up to 1 m in steps of 0.5 cm.

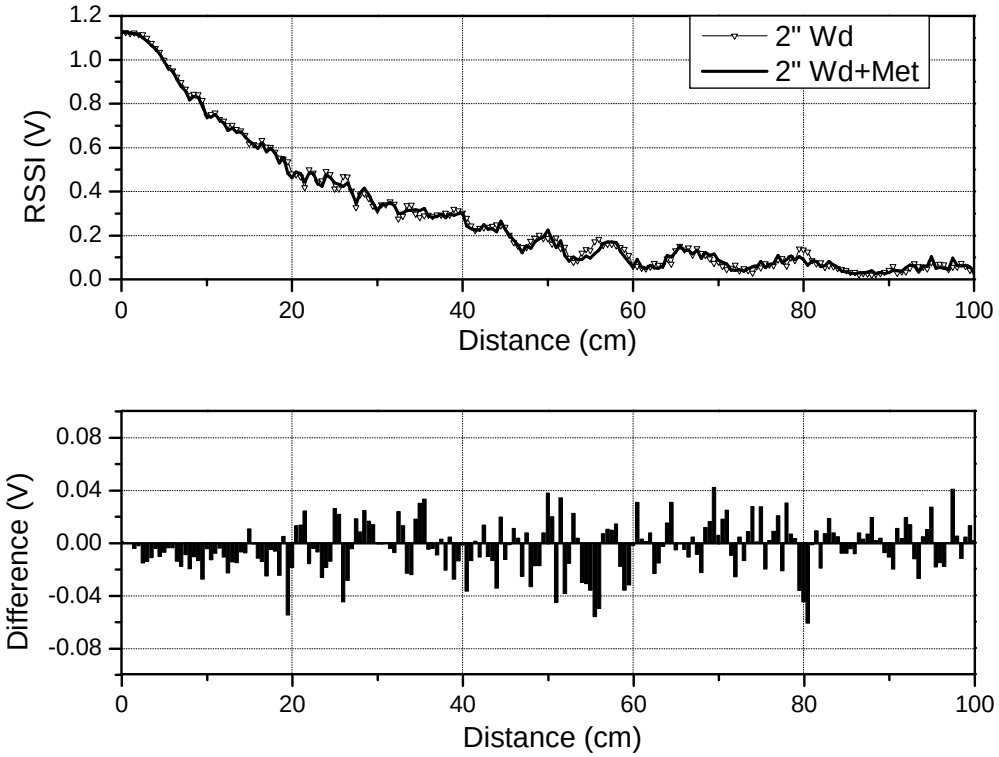

Figure 2.8: RSSI and corresponding residue for 2” thick wooden base up to 1 m in steps of 0.5 cm.

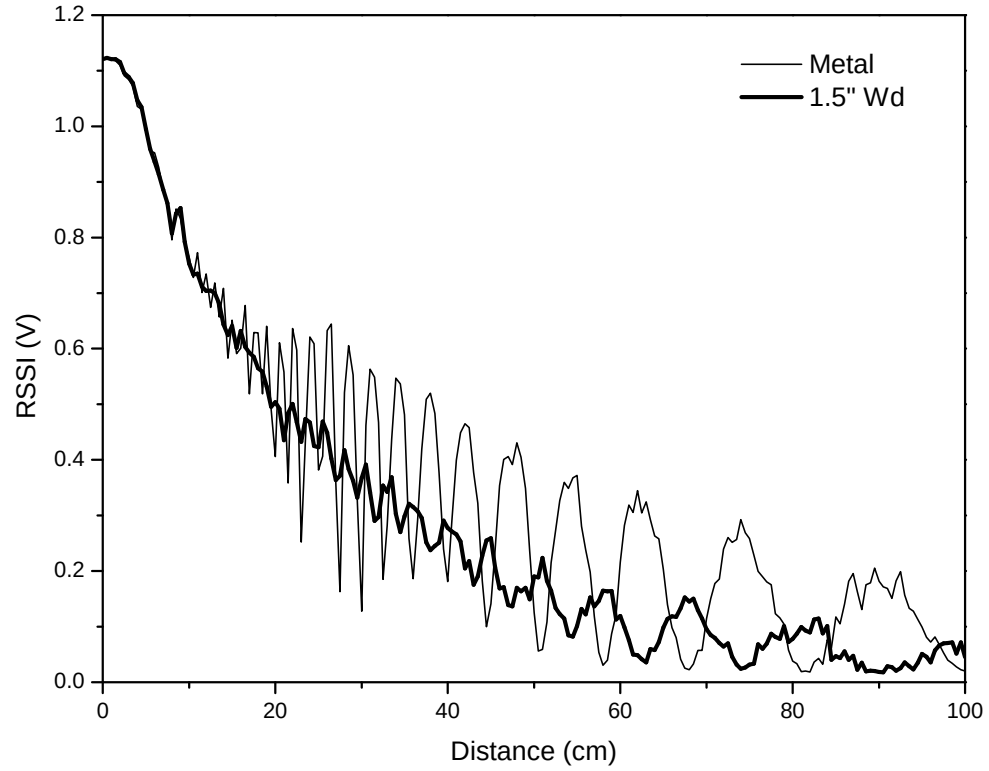

Figure 2.9: RSSI measured on metal and on 1.5” thick wooden base up to 1 m in steps of 0.5 cm

2.4.4 Plastic stands with 20 cm height

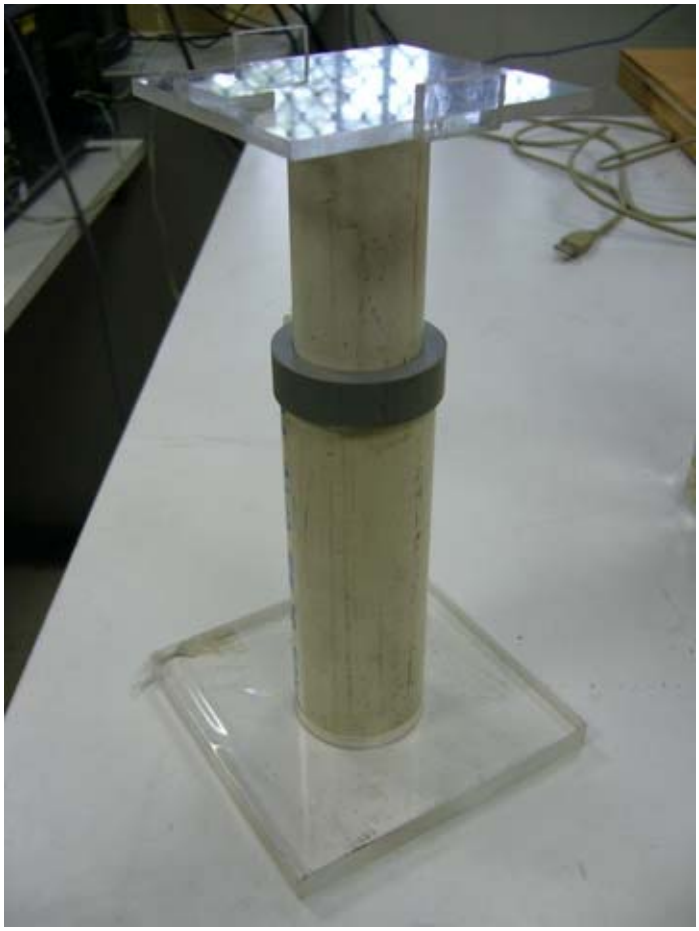

Figure 2.10: 20 cm high plastic stand.

From Section 2.2.4, the RSS method of localization results in higher accuracy if multipath effects of signal variation can be reduced or eliminated.

In order to reduce reflections from the base, the height of the transmitters and the receivers was raised with 20 cm high stands shown in Figure 2.9. Another experiment was conducted by measuring the signal propagation characteristics with the same TX-RX pair twice – once with the 20 cm high stands on the 1.5” wooden base, and another only on the 1.5” wooden base. The resulting curves are plotted in Figure 2.10.

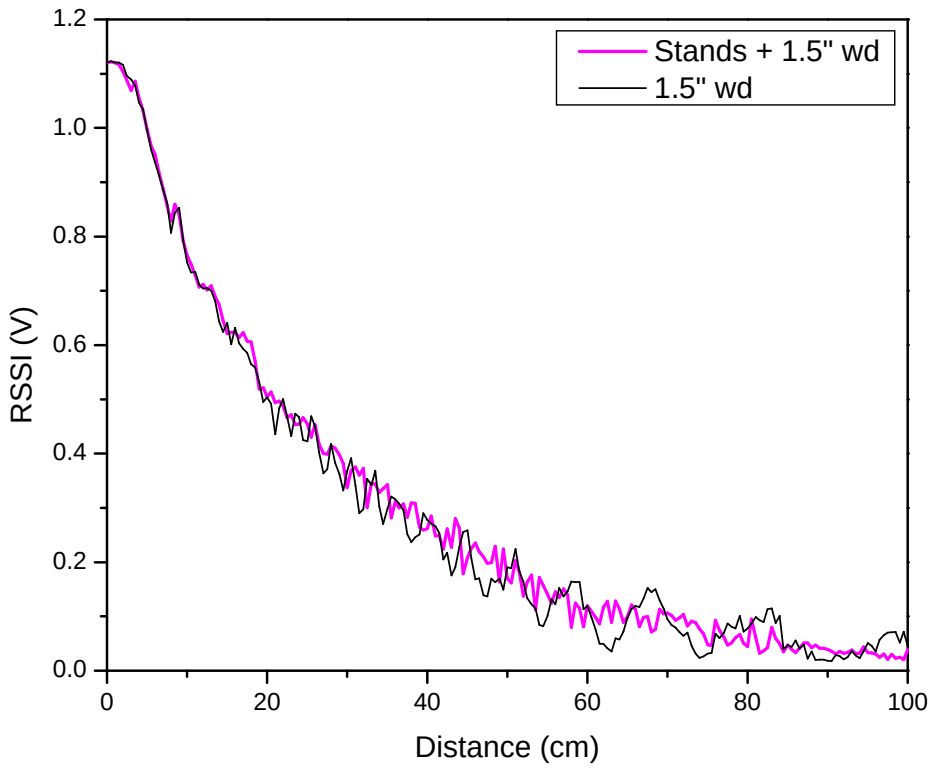

Figure 2.11: RSSI measured with 20 cm high stands on 1.5” wooden base versus only on 1.5” wooden base.

The two curves in Figure 2.10 show a reduction in signal fluctuations when the transmitters and receivers are raised to a height of 20 cm.

2.4.5 Siepel mm-wave absorber

An additional measure for reducing multipath effects from the base is to use mm-wave absorbers. These absorbers, however, are expensive and are mostly made up of soft foam which causes the transmitter and receiver units to tilt, resulting in inaccuracies during measurement.

HYFRAL APM 1.3 is a broadband pyramidal absorber designed and produced by Siepel [24]. Although foam-like, its total height is about 1.3 cm with a base of 0.6 cm. While tilt is unavoidable, it is limited by the short height. The signal propagation characteristics

measured on the Siepel mm-wave absorber are compared in Figure 2.11.

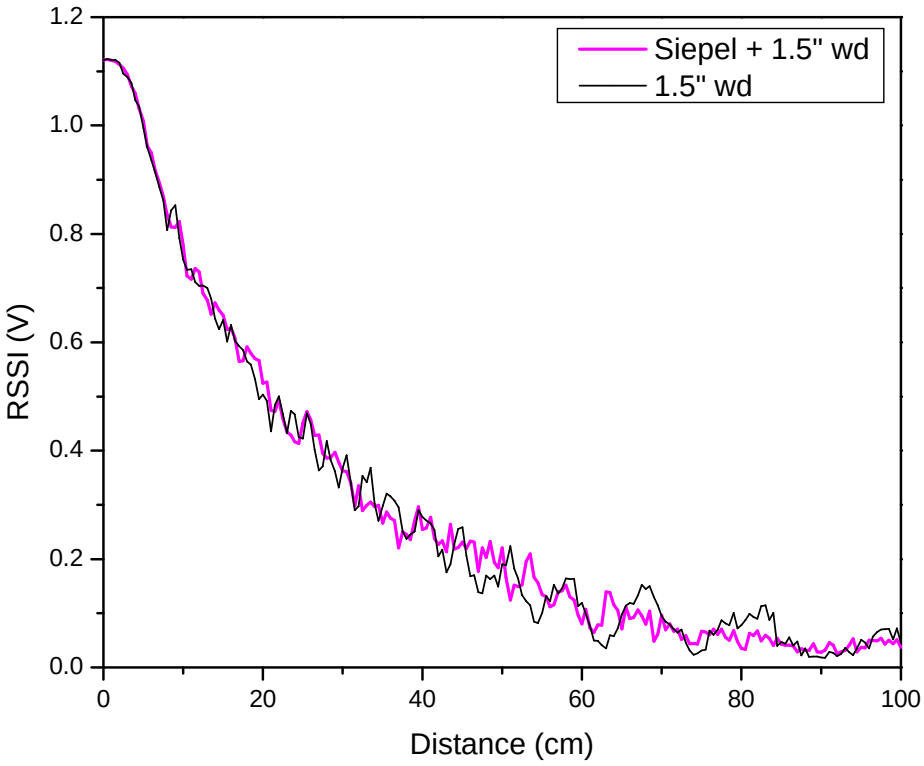

Figure 2.12: RSSI measured with Siepel mm-wave absorber on 1.5” wooden base versus only on 1.5” wooden base.

The results in Figure 2.11 show a reduction in signal fluctuations with Siepel mm-wave absorbers. This is more obvious at larger distances.

Figure 2.12 shows a comparison of the signal propagation characteristics using the 20 cm stands and the Siepel mm-wave absorbers. It is observed that they result in different propagation behavior, particularly beyond a distance of 10 cm. However, it is difficult to judge if one results in more reduction in signal fluctuations as compared to the other.

Hence, the conclusion can only be made by analyzing the accuracy of the localization.

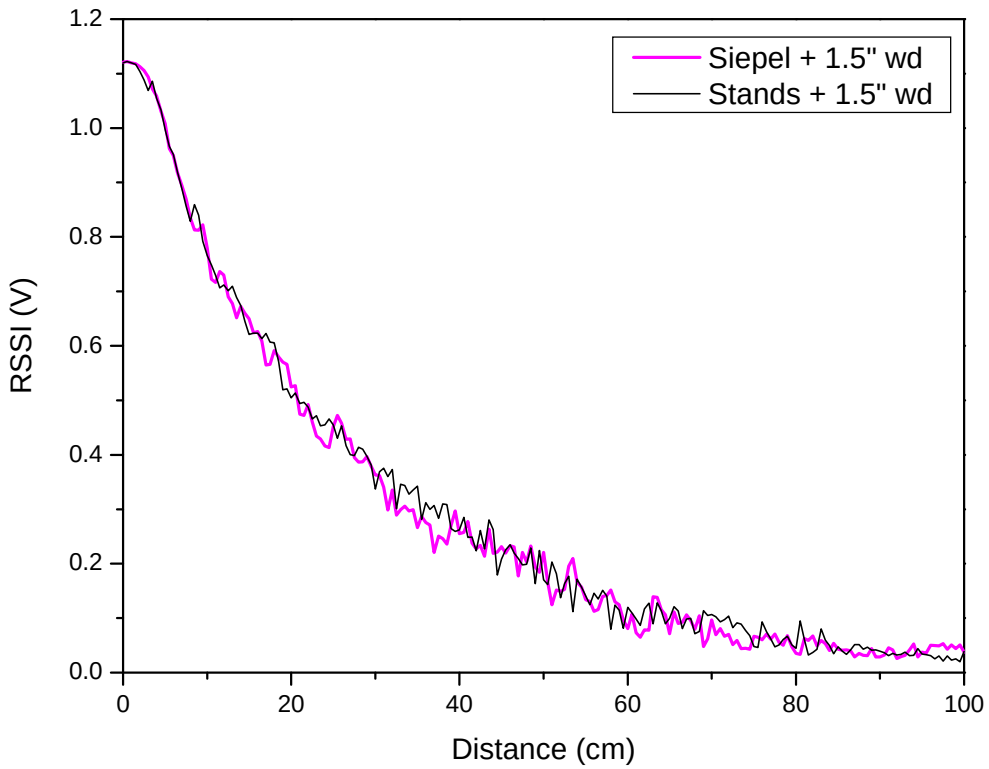

Figure 2.13: Comparison of RSSI measured with Siepel mm-wave absorber and 20 cm stands on 1.5” wooden base.

Finally, the 20 cm stands and Siepel mm-wave absorbers should not be used simultaneously. This is because the 20 cm high structures with the transmitters and receiver are too unstable when placed on the foam-like Siepel mm-wave absorbers.

2.5 Hardware

2.5.1 Transmitters and receivers

The transmitters and receivers from Comotech use the direct conversion architecture to perform upconversion and downconversion. The transmitter, TX60AK1500, is powered by a DC input of 5 V/600 mA and is capable of an output power of 10 dBm. The receiver, RX60AK1500, is powered by a DC input of 5 V/350 mA. The baseband signal can range

from 200 Mbps to 1.5 Gbps and the local oscillator is tuned to output the required 60.5 GHz signal. The voltage range of the RSSI output is between 0 and 1.2 V. The RF (Radio Frequency) and IF (Intermediate Frequency) ports are WR-15 and female SMA (Sub-Miniature type A) ports respectively.

2.5.2 Antenna type

The desired antenna for the system configuration mentioned in Section 2.4.2 is one that provides a consistent RSSI reading despite different antenna directions. Hence, the omni-directional antenna, MD249, from Flann, is selected for this system.

It has an operating frequency range of 59.5 GHz to 65.5 GHz and a gain of 2 dBi. The antenna and the corresponding radiation pattern are shown in Figure 2.13.

Straight waveguide to coaxial adaptors from Quinstar are used to interface the antenna with the RF ports on the transmitters and receiver. This is shown in Figure 2.14. Figure 2.15 shows the Comotech units mounted with the antennas.

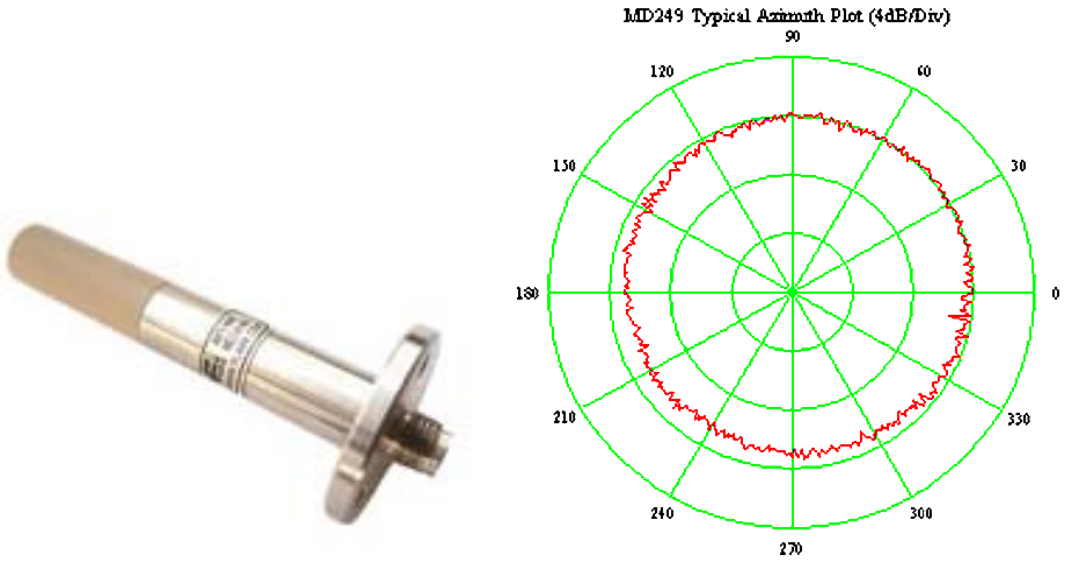

(a) (b)

Figure 2.14: (a) Flann MD249 omni-directional antenna (b) corresponding radiation pattern.

Figure 2.15: Quinstar QWA-15 waveguide to coaxial adaptor.

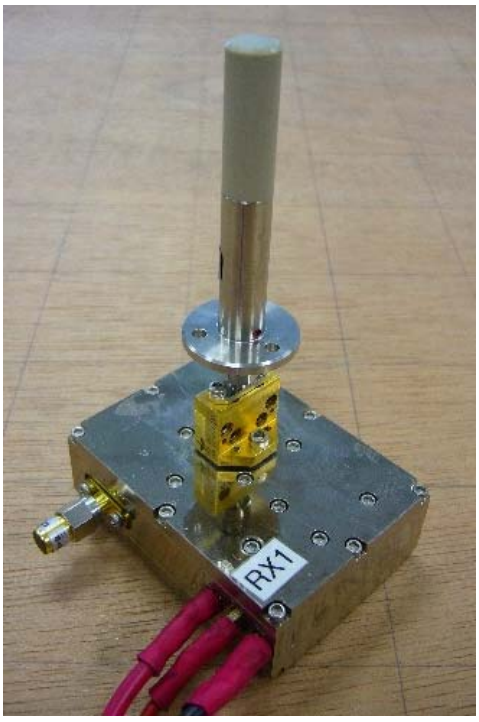

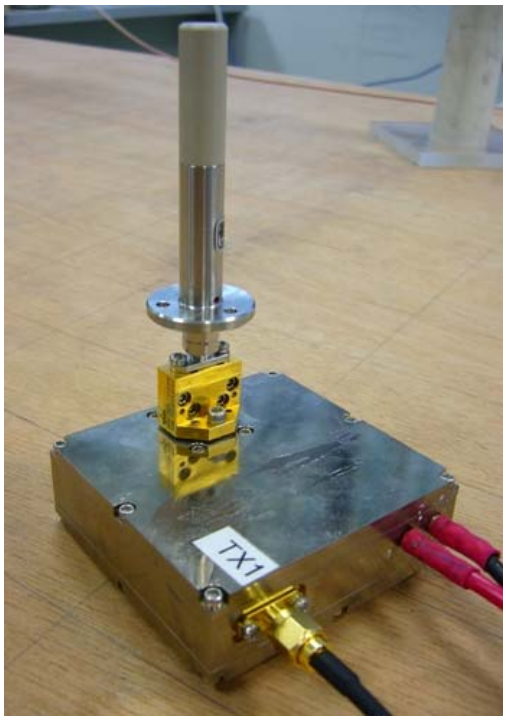

(a) (b)

Figure 2.16: Comotech (a) receiver and (b) transmitter tuned to 60.5 GHz mounted with MD249 omni-directional antennas.

2.5.3 Baseband signal generator - FPGA development board

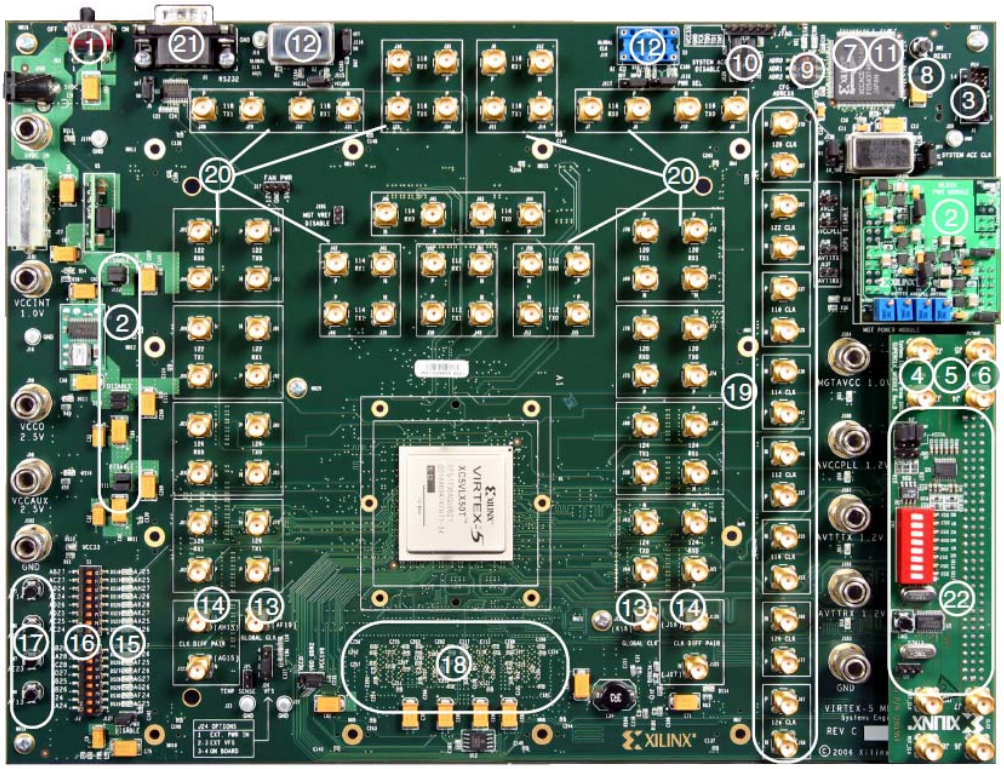

Figure 2.17: Xilinx ML523 FPGA development board.

The four 60 GHz transmitters are driven by a 1.25 Gbps signal which is provided by the ML523 FPGA development board. This board uses a Xilinx Virtex-5 FPGA with 32 pairs of SMA connectors for RocketIO transceivers.

2.5.4 Data acquisition equipment

(a) (b)

Figure 2.18: Data acquisition equipment (a) Agilent U2352A IO board (b) U2902A interface board.

The Agilent U2352A has 16 single ended or 8 differential analog inputs. These inputs have a maximum sampling rate of 250 kSa/s. No analog outputs are available for this model. However, 24 bit programmable digital I/O is available.

2.6 Software

Matlab is the main software used for implementing the localization methods and controlling the I/Os of the data acquisition equipment. It is chosen because of its availability and ease of use in executing complex mathematical algorithms.

Chapter 3 System architecture and localization concept

As mentioned in Chapter 2, the RSS-based localization system is unilateral with four transmitters and one receiver using omni-directional antennas. The system is controlled by a PC with Matlab installed and interfaces with the transmitters and receivers via the Agilent data acquisition devices.

The RSS method of localization uses the intersection of circles, each representing the distance between the receiver and the designated transmitter, to locate the receiver. In this chapter, the RSS localization system architecture and concept are provided.

3.1 Localization system architecture and setup

The block diagram of the localization system with four transmitters and one receiver is shown in Figure 3.1. During real-time localization, the four transmitters turn on sequentially starting from TX1. After each turn, the receiver's RSSI reading is read by the PC and stored. The transmitter is turned off and the next transmitter turns on. This is repeated until the RSSI value of TX4 is obtained and stored. Subsequently, the distance between the transmitter and receiver is extracted and the location is obtained using this information.

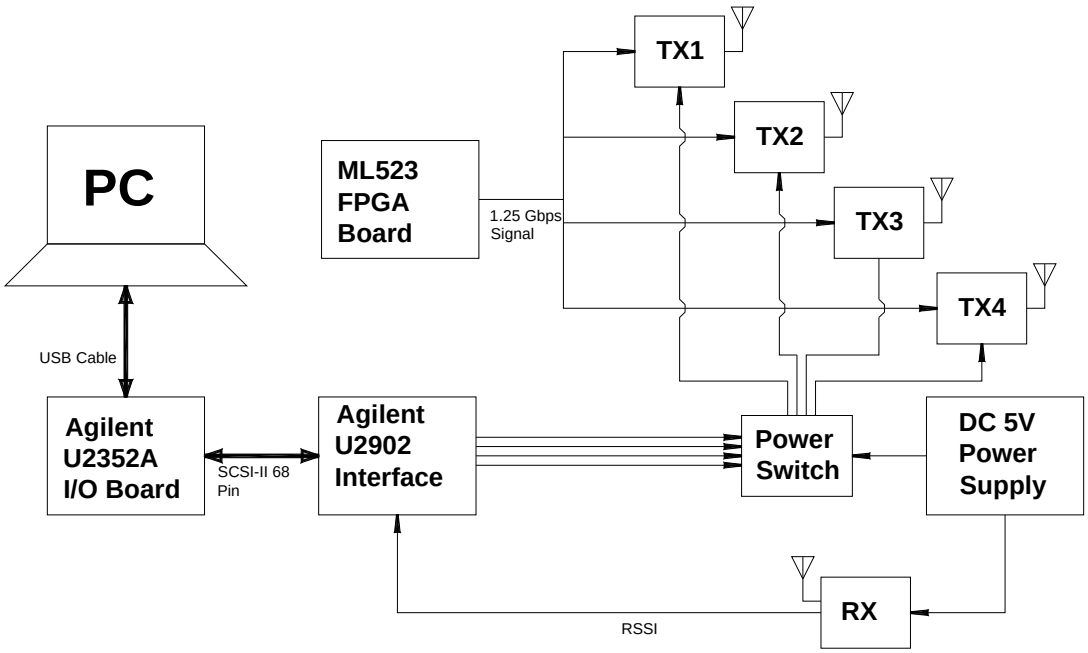

Figure 3.1: System architecture block diagram.

The Agilent U2902 interface has four digital outputs connected to four power switches and a single analog input connected to the RSSI output of the receiver. They are required to enable the four transmitters and retrieve RSS readings during localization.

The DC power supply is connected to the four transmitters via four power switches which are controlled by the PC via the Agilent U2902 interface. The transmitters do not turn on until the PC turns on the individual power switches. The receiver is directly connected and is powered up when the power supply is turned on.

The ML523 FPGA board constantly transmits the 1.25 Gbps signal regardless whether the transmitters are on or off.

All the components, excluding the PC, transmitters and receiver are integrated into a single enclosure shown in Figure 3.2. The setup of the transmitters and receiver are shown in Figures 3.3 and 3.4.

Figure 3.2: Localization system.

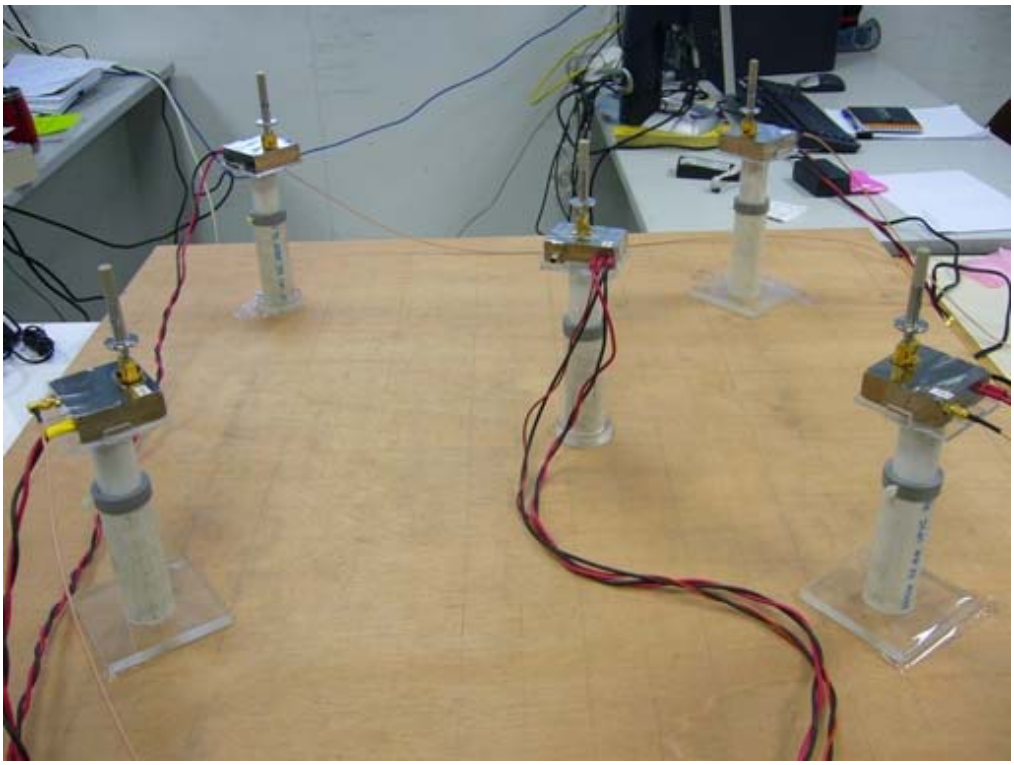

Figure 3.3: Localization setup with 20 cm high stands and 1.5” thick wooden base.

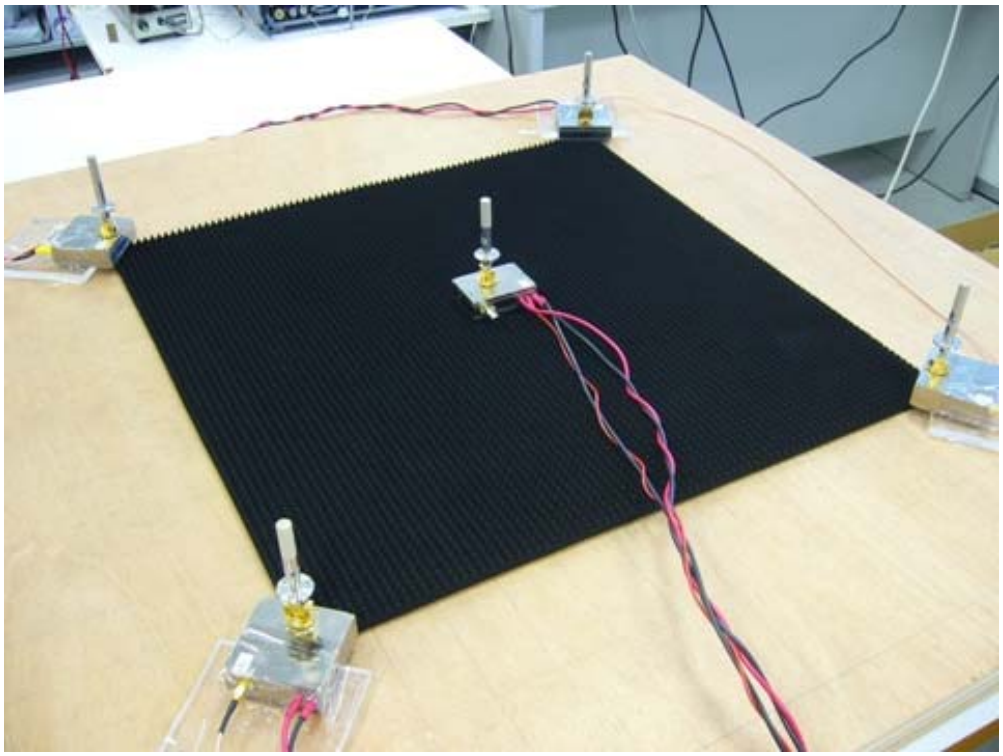

Figure 3.4: Localization setup on Siepel mm-wave absorber and 1.5” thick wooden base.

3.2 Localization concept: Offline and online phase

The localization method has two phases. The first phase is the offline phase where a pre-determined look-up table of RSS values is generated in preparation for real-time localization. Real-time localization is performed in the online phase. Both phases are described in detail in Sections 3.2.1 and 3.2.2.

3.2.1 Offline phase

In the offline phase, a pre-determined look-up table that relates the measured RSSI values to distance for each transmitter is generated through measurements. While a transmitter is transmitting the 60.5 GHz signal, the RSSI values are recorded from the receiver, from 0 mm to 1000 mm, in steps of 5 mm. The measurement setup is similar to Figure 2.4. This is repeated for all four transmitters and generates a total of 804 data

points on the 20 cm high stands and Siepel mm-wave absorber each. Each look-up table is then used to create a propagation model of RSS versus distance using splines in voltage (V) or decibels (dBV). As an example, the measured RSSI and the spline fit for TX1 in V and dBV is shown in Figures 3.5 and 3.6 respectively. The data and splines for the remaining transmitters are shown in Figures A2 to A8 of Appendix A. The inset in each plot shows the expected distance error from each transmitter due to the diifference between the measured value and the value from the spline curve. Similar measurement data on the Siepel mm-wave absorbers and the corresponding splines are presented in Figures A9 to A16 of Appendix A.

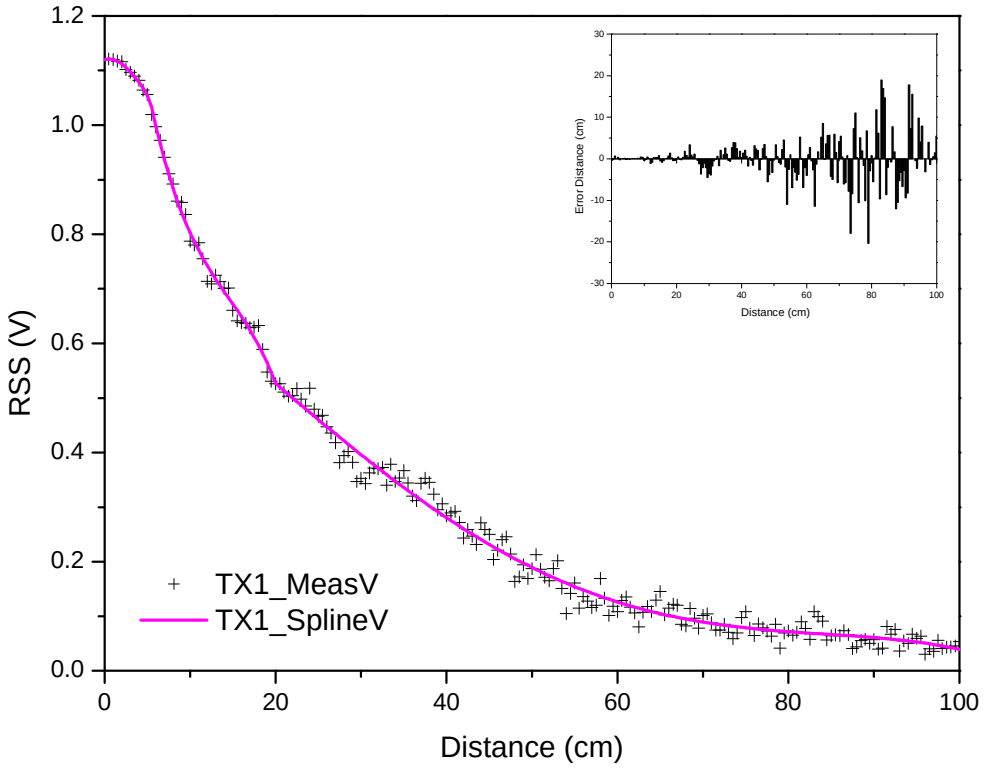

Figure 3.5: Measured RSS and spline-fit of TX1 (in V) on 20 cm stands with inset showing the expected distance error.

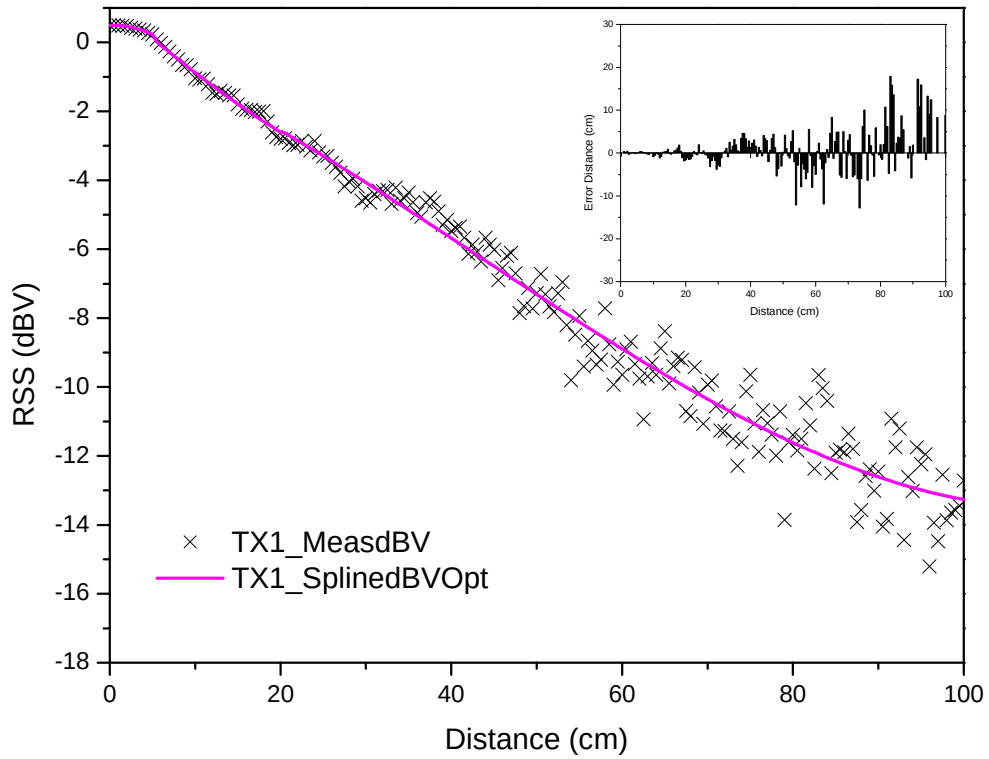

Figure 3.6: Measured RSS and spline-fit of TX1 (in dBV) on 20 cm stands with inset showing the expected distance error.

The most distinct difference between Figure 3.5 and Figure 3.6 is the linearity of the RSS in dBV with respect to distance. While the expected distance error shown in the inset of the two figures show similar trends, the curve-fitting process was less complex when RSS is plotted in dBV.

For both curves, three splines were used to fit three sections; 0 to 5 cm, 5.5 to 20 cm and 20.5 to 100 cm. The equations representing the three sections of the spline-fit in V and dBV are shown in (3) to (5) and (6) to (8) respectively.

$$y = -4.2.10^{-5}x^4 + 0.000645x^3 - 0.00594x^2 + 0.005878x + 1.1198 \quad (3)$$

$$y = -0.0002x^3 + 0.008774x^2 - 0.1498x + 1.624 \quad (4)$$

$$y = -2.28.10^{-8}x^4 + 4.73.10^{-6}x^3 - 0.00023x^2 - 0.0092x + 0.7673 \quad (5)$$

$$y = -0.01196x^2 + 0.00667x - 0.49558 \quad (6)$$

$$y = 0.00181x^2 - 0.22751x - 1.214 \quad (7)$$

$$y = 1.21.10^{-5}x^3 - 0.00156x^2 - 0.0965x - 0.09858 \quad (8)$$

Since the data plotted in dBV is more linear, the three spline equations did not surpass 3 degrees, unlike the spline belonging to the data plotted in V. In addition, the process of spline approximation for the data in V is tedious and required more iterations.

3.2.2 Online phase

During the online phase, the transmitters transmit sequentially and the RSS is measured at the receiver output. For example, as shown in Figure 3.7, while all other transmitters are off, transmitter 1 (TX1) is turned on for more than 150 ms before the program reads the RSSI value from the receiver, RX. This sampling and storing of data lasts for 2 ms, as depicted by B. The 150 ms delay is required because the transmitters require at least 100 ms to power up. For reason of completeness measured results of the power up are shown in Appendix B. After that, TX1 is turned off and TX2 is turned on. The process repeats for all four transmitters.

As depicted by D, after the four RSSI values have been sampled and stored, they are mapped to the look-up table obtained in the offline phase. Four distances corresponding to the four RSSI values are obtained and fed into the localization algorithms to obtain an estimated position of the receiver. This estimated position is then plotted on the screen.

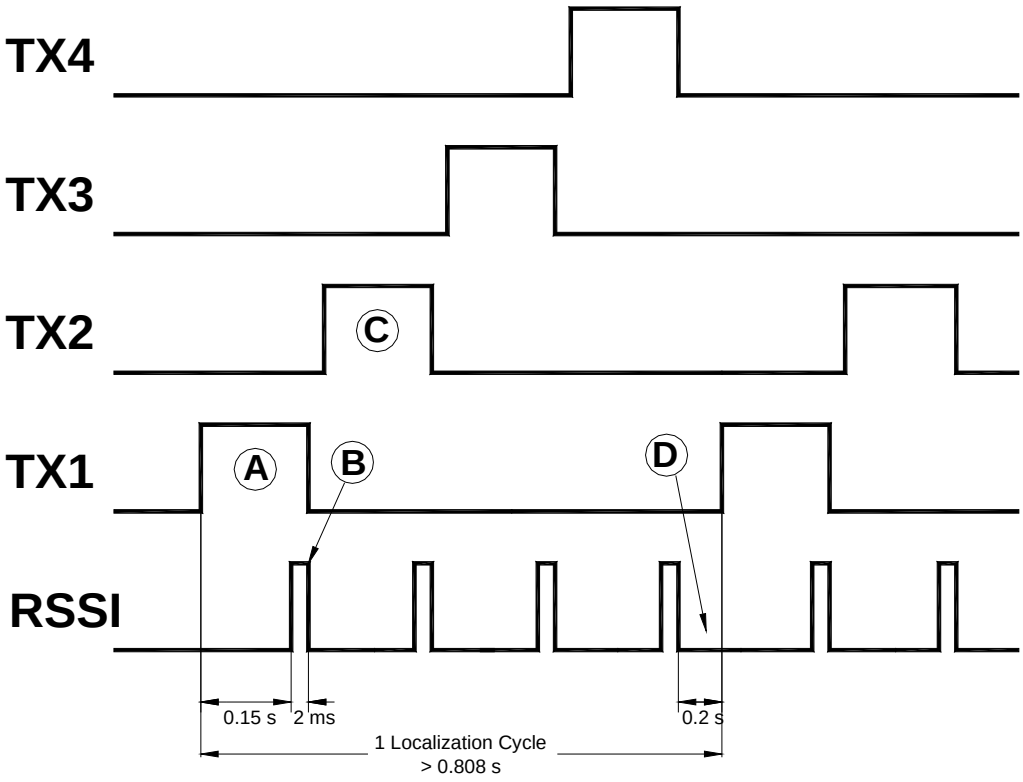

Figure 3.7: Timing diagram of the online phase.

Chapter 4 RSS-based localization methods

4.1 Introduction to RSS-based localization methods

Trilateration and fingerprinting are two general methods commonly used for RSS-based localization systems. Both require a pre-determined look-up table obtained in an offline phase. This section serves as a background for the actual algorithms used in the actual localization program explained in the next section.

4.1.1 Fingerprinting

The method of fingerprinting requires a large look-up table of known RSS measurements at various grid points measured during the offline phase. The look-up table will then be searched to match the RSS values acquired during the online phase. The disadvantage of this look-up table is its site dependence, non-reusable in another environment, and is time consuming to create [20].

4.1.2 Trilateration

Trilateration is a geometrical technique that can locate an object based on its Euclidean distance from three or more objects [25]. This method can be used if the relationship between the RSS and distance is known. For an ideal case as shown in Figure 4.1, the target receiver, RX, is accurate in estimating its distance from all the transmitters. This ideally results in a single intersection point within the desired area.

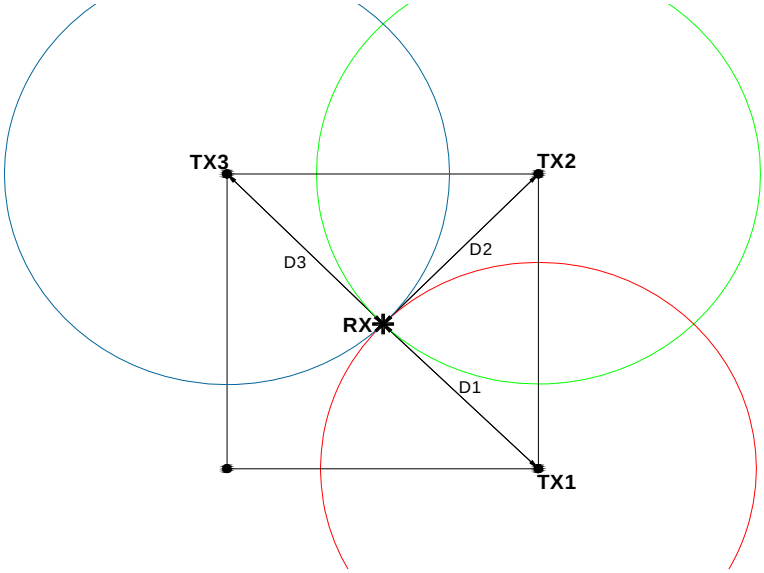

Figure 4.1: Ideal case of trilateration.

Practically, the transmitters and receivers are not ideal. Moreover, signal fluctuations due to interferences and multipath effects can result in inaccuracies. As illustrated in Figure 4.2, these inaccuracies cause an area of ambiguity instead of a single point. Further processing will be needed to estimate the position of the target. Due to the impracticalities of the fingerprinting method, the trilateration method will be used.

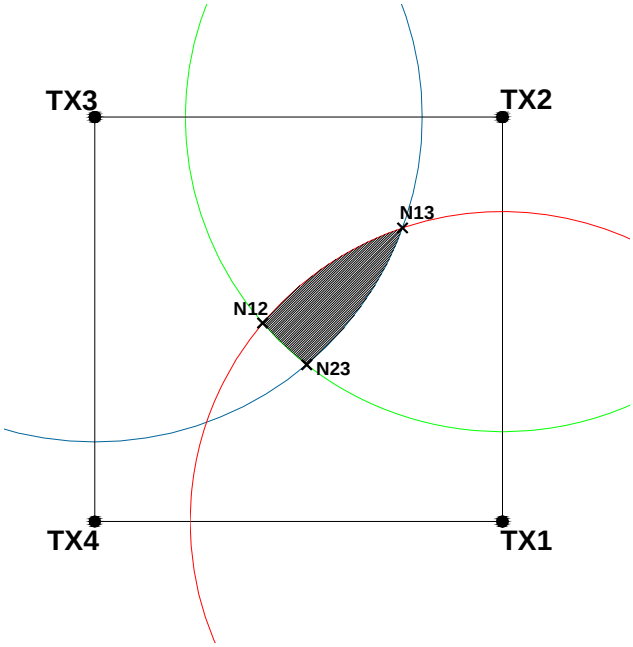

Figure 4.2: Non-ideal case of trilateration.

4.2 RSS-based localization methods used in this project

4.2.1 Method 1: Centre of Gravity (COG)

The COG method of localization is the most straight-forward method of obtaining the average of the four intersecting points. When four circles intersect, there are a total of twelve intersection points. As shown in Figure 4.3, choosing only the intersection points of adjacent circles within field of interest, and averaging the four x-coordinates and four y-coordinates will produce the final results.

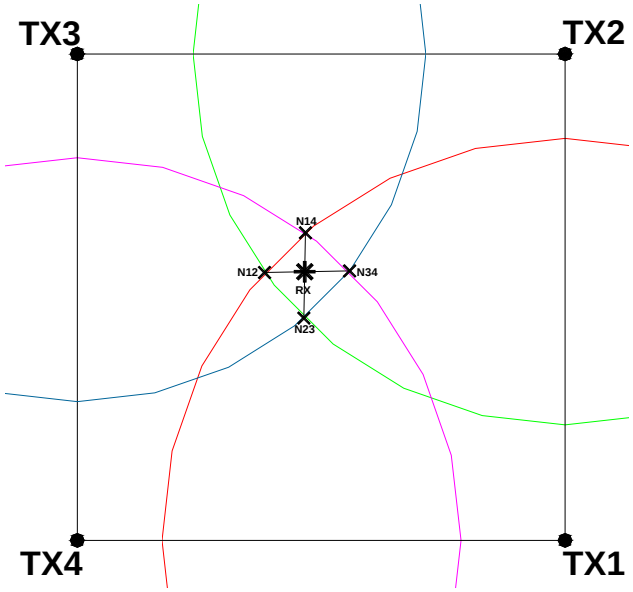

Figure 4.3: Centre of gravity (COG) method of four intersecting circles.

4.2.2 Method 2: Weighted Centre of Gravity (WCOG)

The WCOG method is an extension of the COG method. Instead of solving for the intersection points of all four circles using COG, it solves for the intersection points of three circles at any one time using COG with weights assigned to each intersecting point.

Referring to Figure 4.4, the distances, D23, D12 and D13 will create three weights, W23, W12 and W13 respectively as follows:

$$W12 = \frac{D12}{D12 + D13 + D23}, \quad W13 = \frac{D13}{D12 + D13 + D23}, \quad W23 = \frac{D23}{D12 + D13 + D23} \tag{3}$$

Note that the sum of the three weights is one. These weights, W12, W13 and W23, are then multiplied with the intersection points, N12, N13 and N23 respectively to compose the final estimated position, P1. The point P1', estimated by the COG method is drawn for comparison in Figure 4.4.

Because there can be four combinations of transmitters, WCOG has to be iterated four times to obtain four points, P1 to P4, as shown in Figures 4.4 to 4.7. The four points are then averaged to obtain the final position, P, which is shown in Figure 4.8.

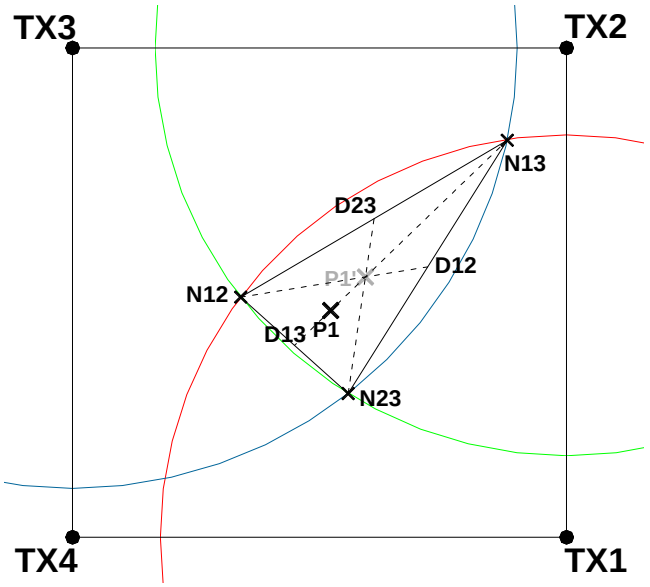

Figure 4.4: Weighted COG method of circles estimated by TX1, TX2 and TX3.

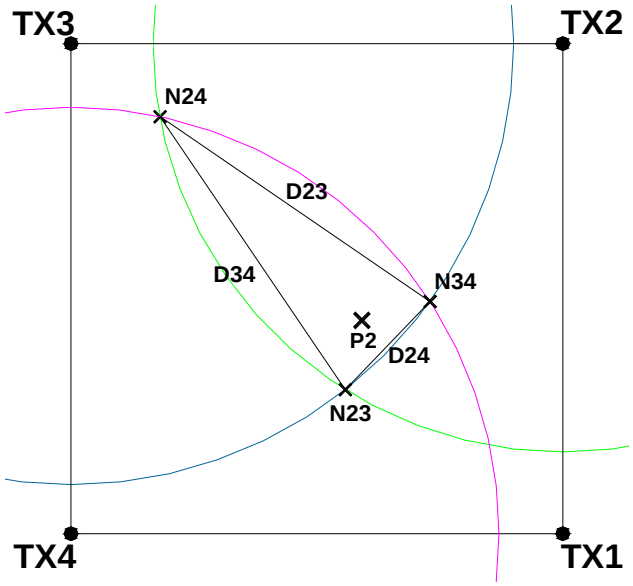

Figure 4.5: Weighted COG method of circles estimated by TX2, TX3 and TX4.

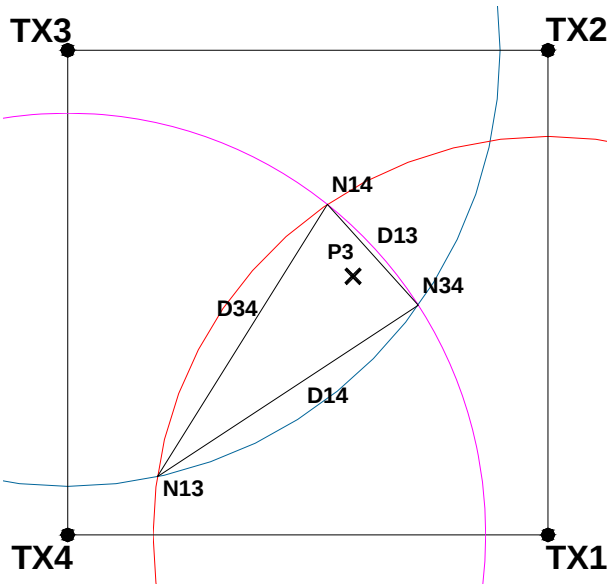

Figure 4.6: Weighted COG method of circles estimated by TX1, TX3 and TX4.

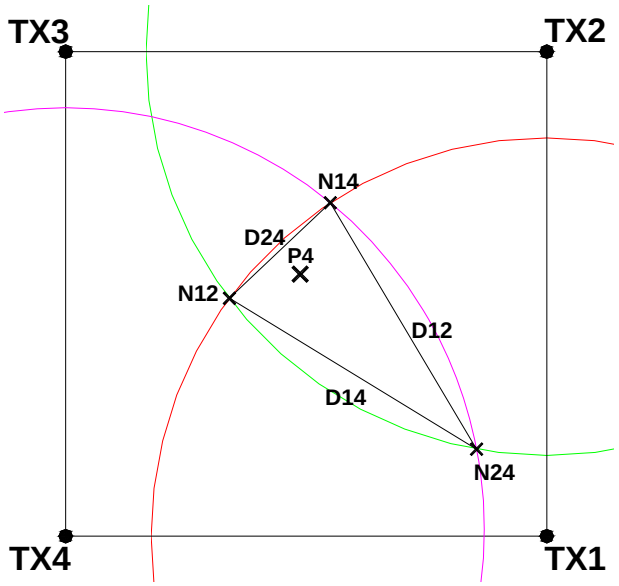

Figure 4.7: Weighted COG method of circles estimated by TX1, TX2 and TX4.

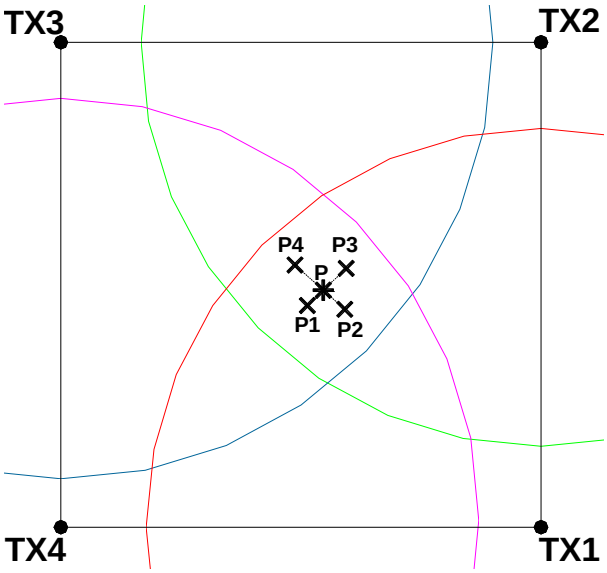

Figure 4.8: Final position, P, composed from the four points acquired by weighted COG.

4.2.3 Method 3: Iterated Weighted Centre of Gravity (IWCOG)

The IWCOG method is a refinement of the WCOG. It takes the four points obtained by the WCOG method and again performs a weighted COG four times. This produces another four points that form a smaller polygon compared to the initial guess. Theoretically, when

this process is iterated infinitely, the four points will converge to a single position. In this system, however, only a second iteration is performed and the average is taken to obtain the final position.

4.2.4 Method 4: Removing the circle from the lowest signal

Based on the assumption that the transmitter closest to the receiver (ie. strongest RSSI) will provide the most accurate signal, and vice versa, this method attempts to determine the furthest transmitter, and discards its RSSI reading. Using the RSSI values from the three closest transmitters, it performs a weighted COG to determine its final position.

Chapter 5 60 GHz RSS localization with omni-directional antennas

In Chapters two to four, various software and hardware considerations are presented. This chapter brings together these considerations, forming an RSS localization system at 60 GHz and presenting the results of the various options.

Section 5.1 explores the use of splines derived from measured results in voltage (V) and decibels (dBV) to determine the optimum option. Sections 5.2 to 5.5 present and compare the performance of the system using the four methods discussed in Section 4.2 on 20 cm stands and Siepel mm-wave absorbers. The chapter ends with conclusions and recommendations from this work.

5.1 Localization with two-dimensional spline in V or dBV

In Section 3.2.1, the relationship between the measured RSS and distance in voltage and dBV together with the corresponding splines were presented. To understand how the two sets of data impact the localization error, localization was performed using the 20 cm stands for the two cases and the first method (COG method) discussed in Section 4.2.

To compare the localization errors for the two cases, the cumulative distribution function of both cases are plotted. For each set of data, a table is first formed with the magnitude of localization errors sorted in ascending order, located in the first column. The second column consists of the cumulative percentage that is obtained by the percentage of each data point plus the sum of the percentage of preceding data points. This column is plotted against the previous column, resulting in the required CDF. The CDFs of the localization

error belonging to the two splines is presented in Figure 5.1.

The figure shows that the localization error is comparable whether the splines are fitted to the measured RSS in V or dBV. The distribution of error is similar and the error at the 90th percentile is approximately 4.6 cm for both cases.

While the expected distance error is similar, spline-fitting is less complex with the plot in dBV due to its more linear nature. This was previously discussed in Section 3.2.1. Thus, for the subsequent cases, the receiver will be localized with splines derived from RSS data in dBV.

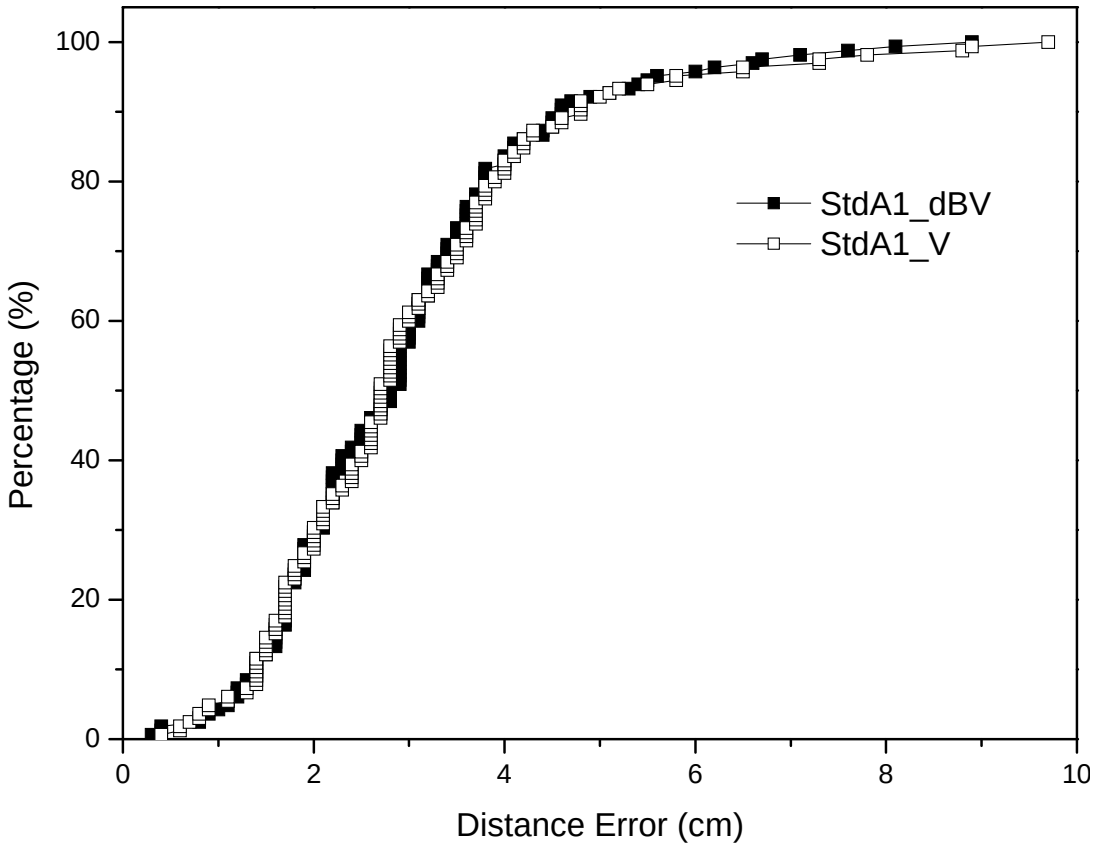

Figure 5.1: Error CDF of method 1 on 20 cm stands using splines derived from measured RSS in V and dBV.

5.2 Localization with 20 cm stands

In Sections 5.2 and 5.3, error vector plots and the CDF of the localization error on 20 cm

stands and Siepel mm-wave absorber are presented respectively. Each section compares the differences in localization error resulting from the four localization methods discussed in Section 4.2. Vector plots of localization errors allow the observation of error trends in two dimensions; the absolute error and the direction of the error in any particular region. This information can be used for comparing the accuracy of different localization methods and spline-approximated propagation models. In addition, this information can be used for detecting problematic transmitters that require recalibration.

The vectors of localization errors are presented on a grid with a 5 cm resolution. Each vector starts at the actual position and the arrow tip ends at the estimated location. Its length represents the absolute error at that particular point.

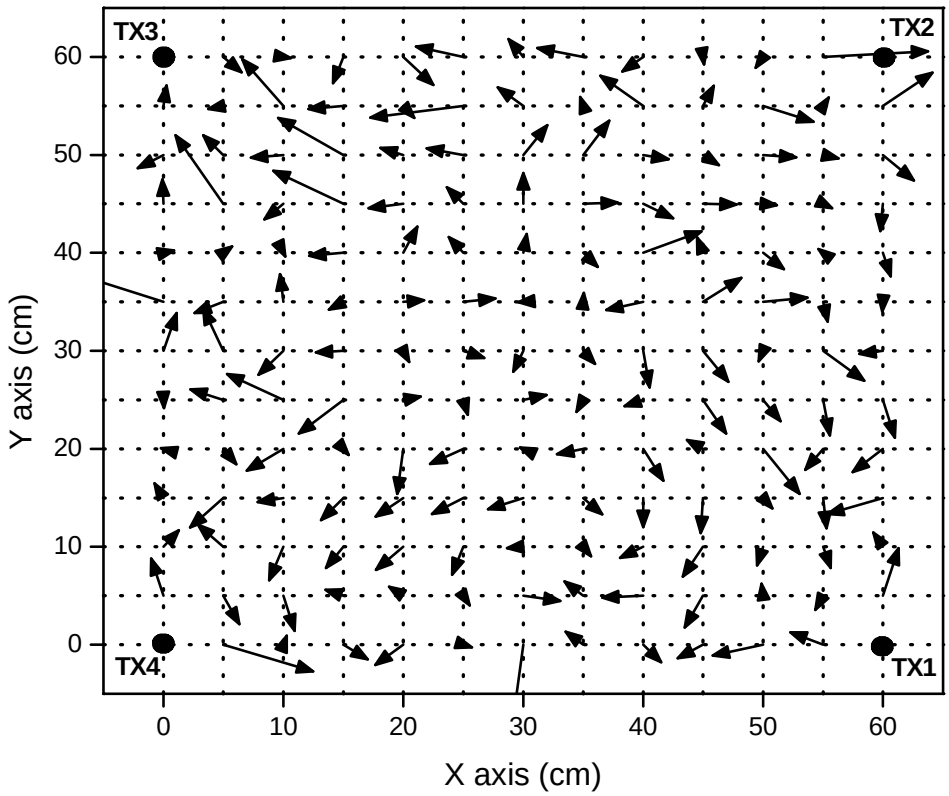

Figure 5.2: Vector plot of localization error on 20 cm stands using method 1.

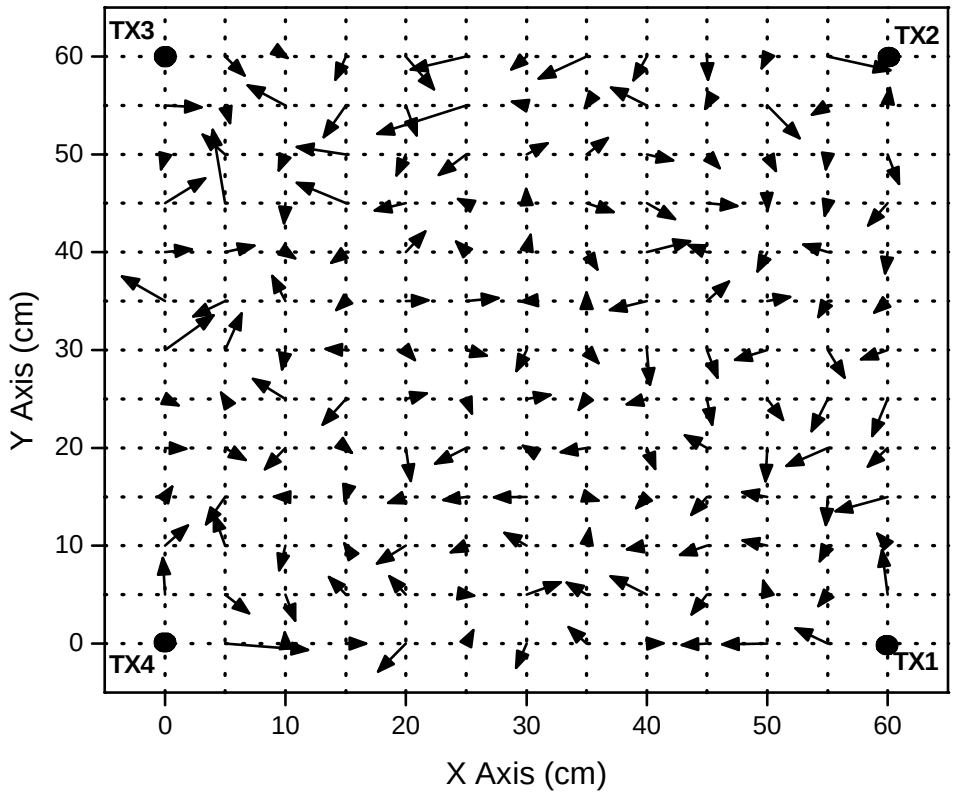

Figure 5.3: Vector plot of localization error on 20 cm stands using method 2.

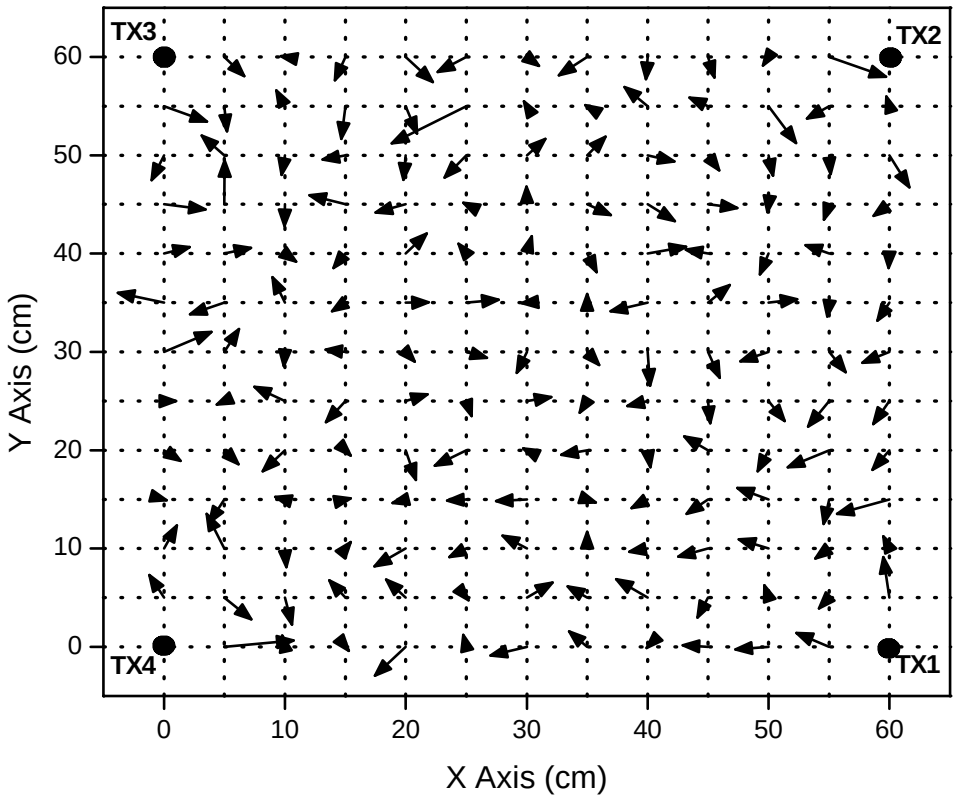

Figure 5.4: Vector plot of localization error on 20 cm stands using method 3.

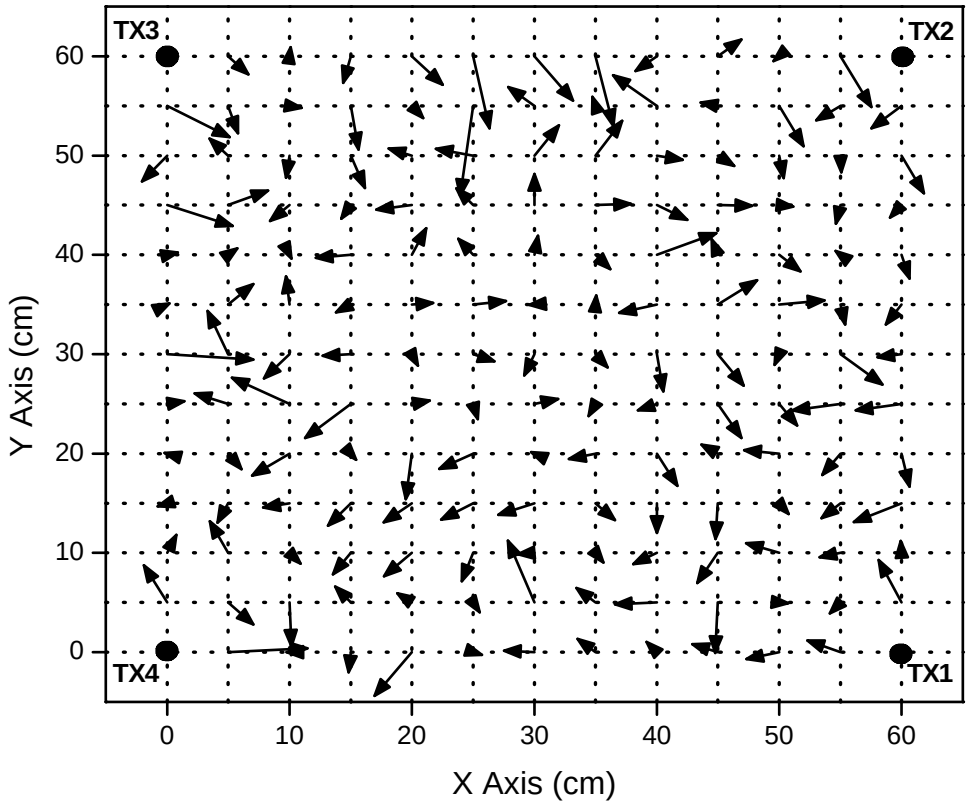

Figure 5.5: Vector plot of localization error on 20 cm stands using method 4.

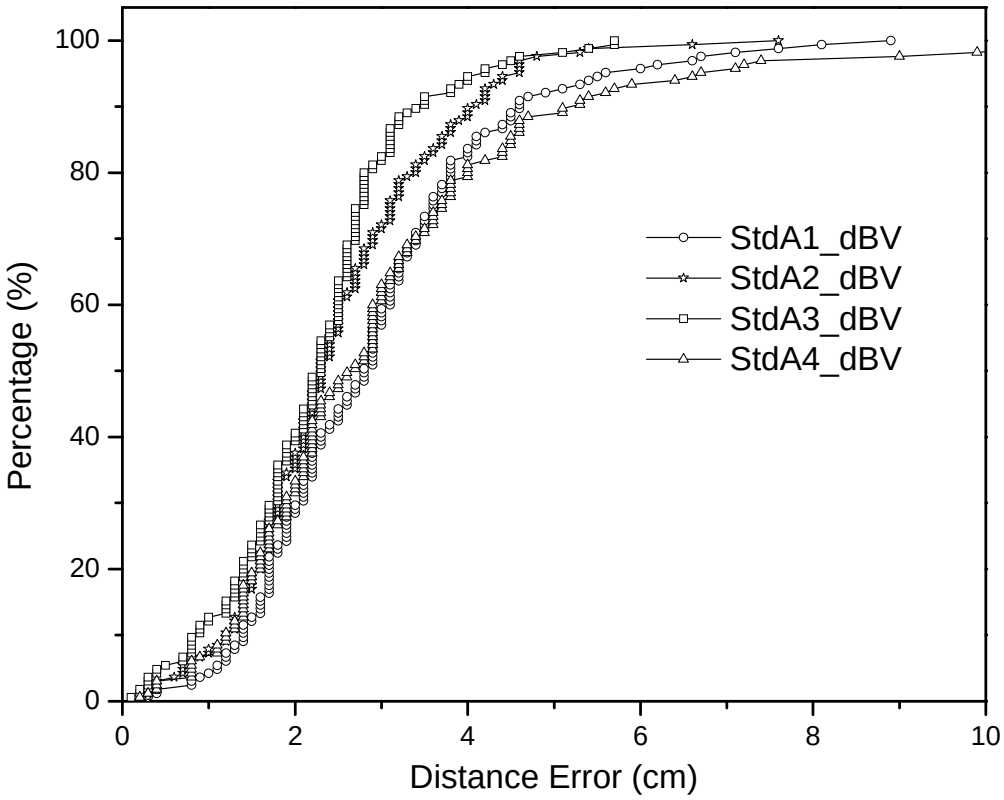

Figure 5.6: Error CDFs of the four methods on 20 cm stands.

From Figures 5.2 to 5.5, a higher accuracy can be observed in the central 20 cm^2 square area. This is obvious with the scatter of short arrows in the center. In general, larger errors are seen in all four figures when the receiver is closer to the borders and corners. No particular trend in direction is especially visible as all the arrows point in random directions.

In Figures 5.3 and 5.4 however, there seems to be a visible reduction in the number of long arrows as compared to Figures 5.2 and 5.5. A comparison of the four error CDFs in Figure 5.6 confirms the observation. The plot shows steeper CDFs belonging to methods 2 and 3, implying overall reduced localization errors. Distance errors exceeding 4 cm make up of only 5 % of the total number of errors for both methods. Of the four methods, method 3 works best, achieving a distance error of 3.5 cm at the 90^{th} percentile. This contrasts with methods 1 and 4 where distance errors exceeding 4 cm make up more than 15 % of the total errors.

It is also interesting to note that the CDF of method 4 is the worst performing despite the removal of the weakest RSS signal supposedly overwhelmed by noise. This shows that useful location information can still be extracted from RSS readings that are comparatively weaker and significantly affected by noise.

5.3 Localization with Siepel mm-wave absorber

The stands are removed and Siepel mm-wave absorber is placed on the wooden base within the 60 cm by 60 cm area. The vector error plots on Siepel mm-wave absorber are presented in Figures 5.7 to 5.10. The corresponding error CDFs are presented in Figure

5.11.

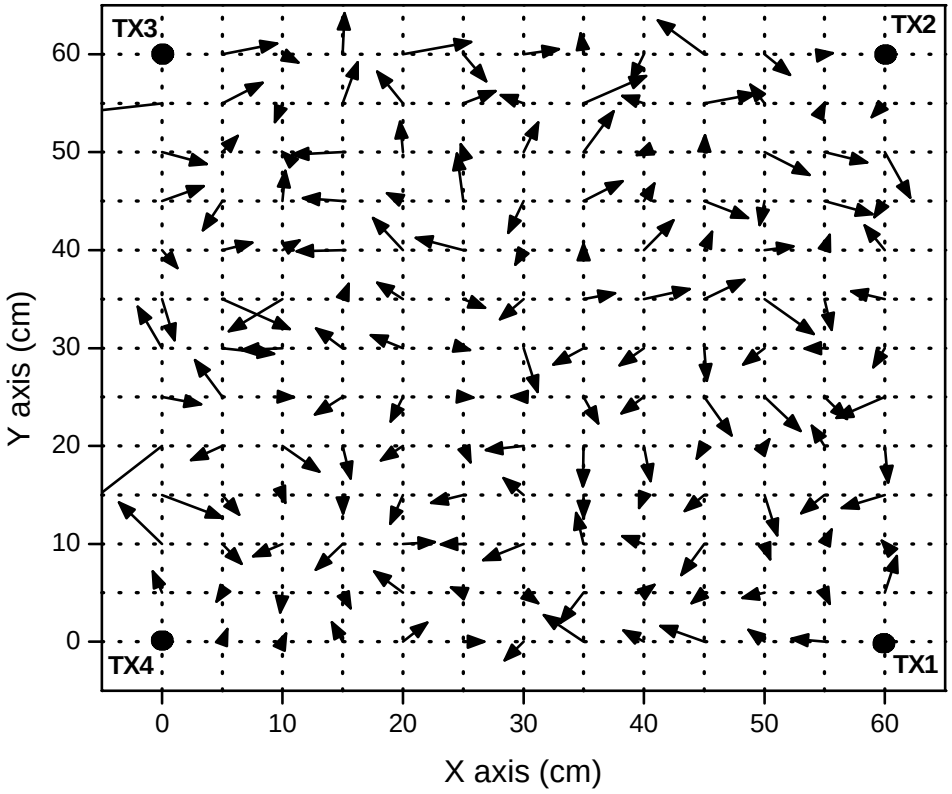

Figure 5.7: Vector plot of localization error on Siepel mm-wave absorbers using method 1.

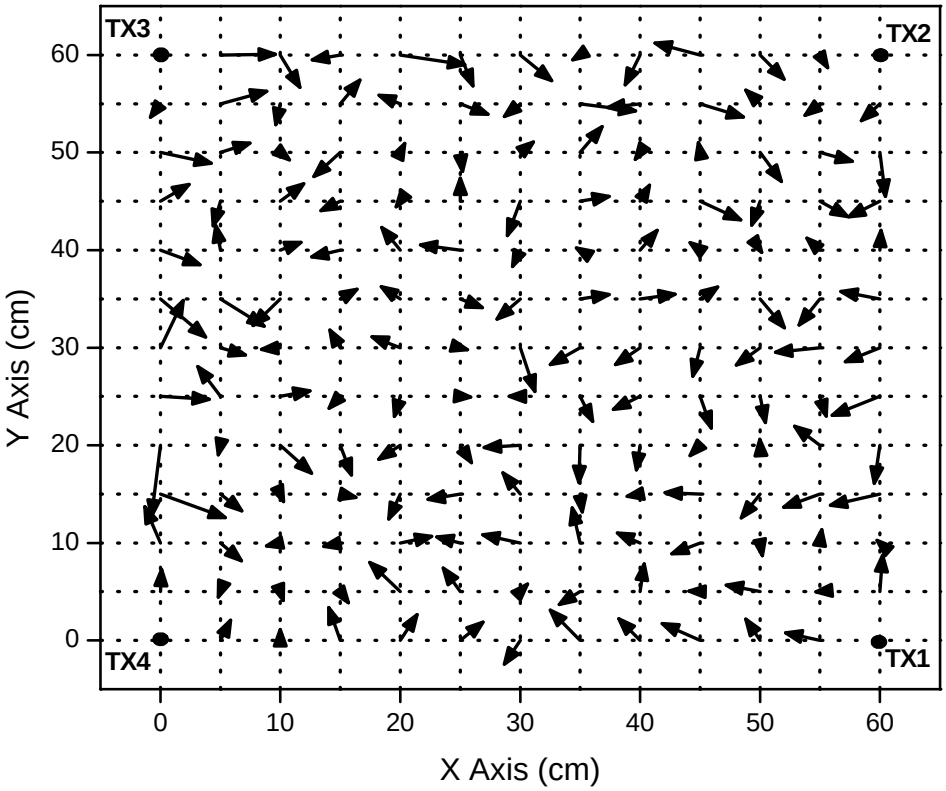

Figure 5.8: Vector plot of localization error on Siepel mm-wave absorbers using method 2.

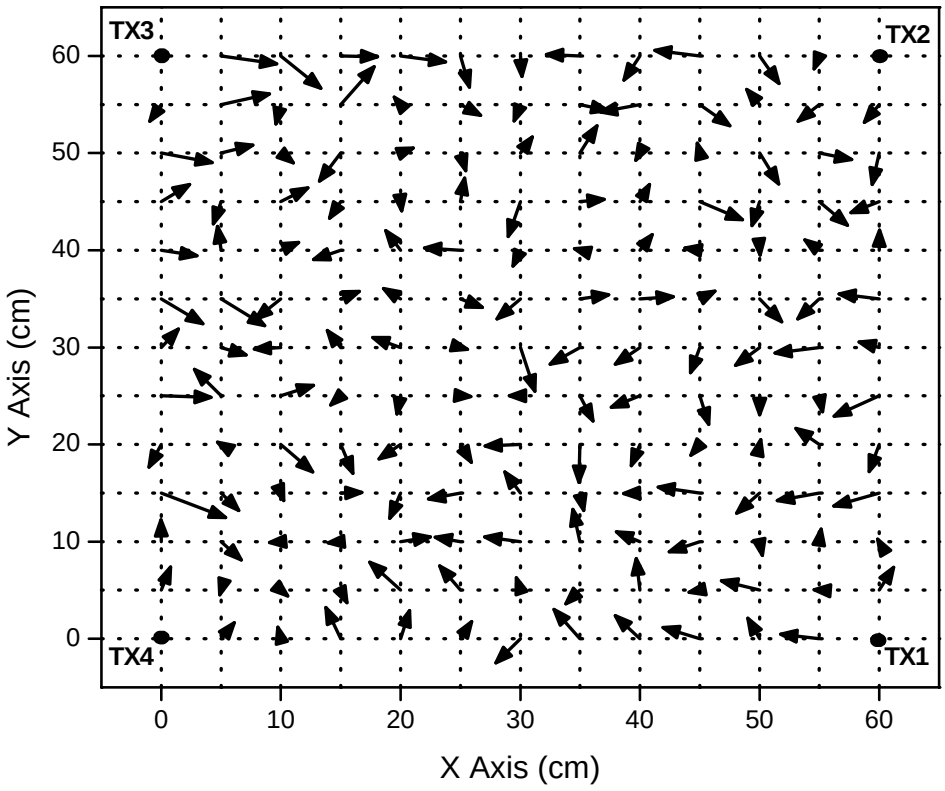

Figure 5.9: Vector plot of localization error on Siepel mm-wave absorbers using method 3.

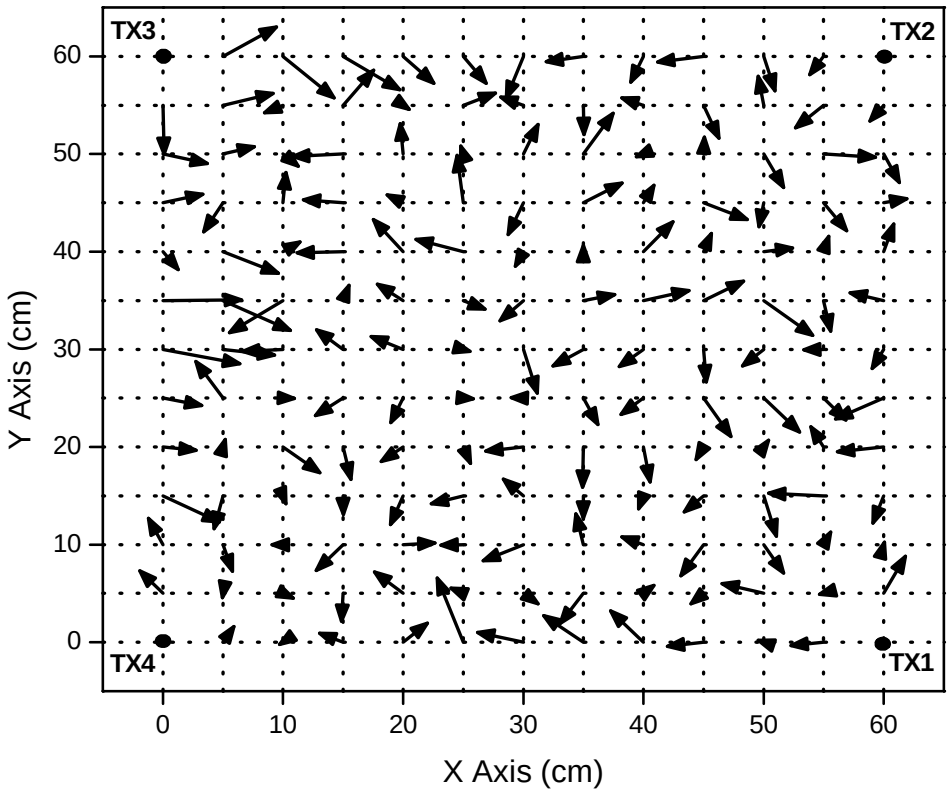

Figure 5.10: Vector plot of localization error on Siepel mm-wave absorbers using method 4.

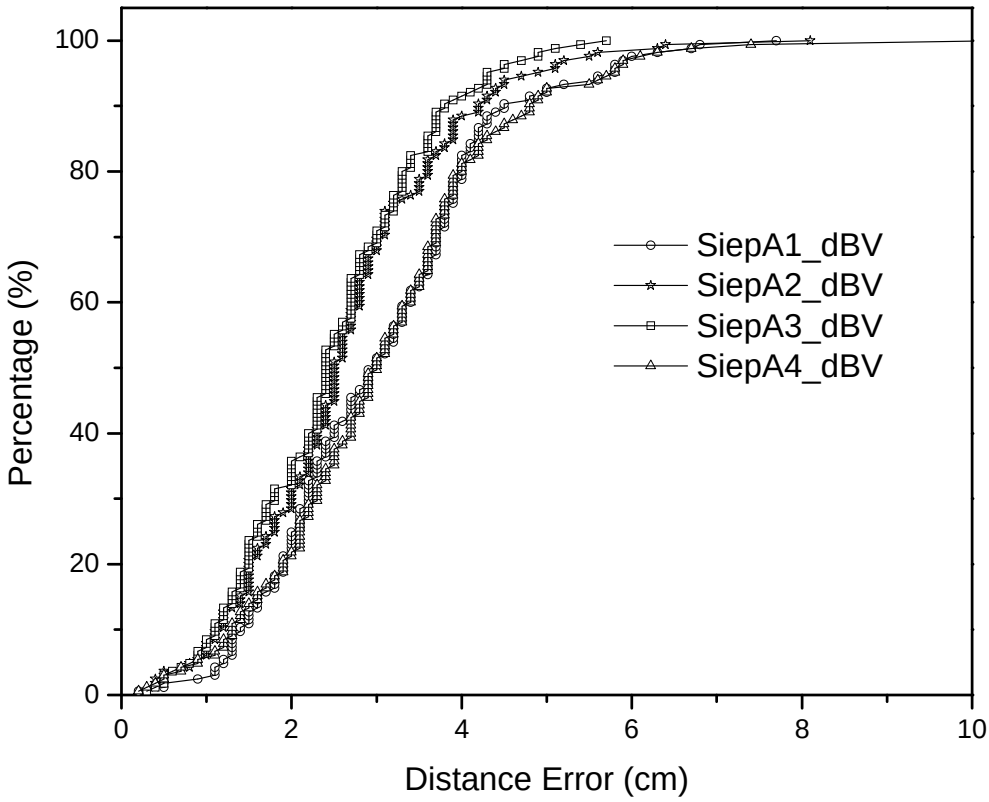

Figure 5.11: Comparing the error CDFs of the four methods on Siepel mm-wave absorber.

Similar to Section 5.2, the vector plots of Figures 5.7 to 5.10 show that methods 2 and 3

result in superior localization accuracy as compared to methods 1 and 4.

This is also observed in Figure 5.11 from the steeper CDF plot. Out of the four methods, method 3 works best, obtaining a distance error of 3.8 cm at the 90th percentile.

5.4 Comparison between 20 cm stands and Siepel mm-wave absorber

From Sections 5.2 and 5.3, it is observed that method 3 has the best performance when localization is performed on 20 cm stands and on Siepel mm-wave absorber. By comparing the CDF of both cases as presented in Figure 5.12, elevating the transmitters with the 20 cm stands result in better localization accuracy.

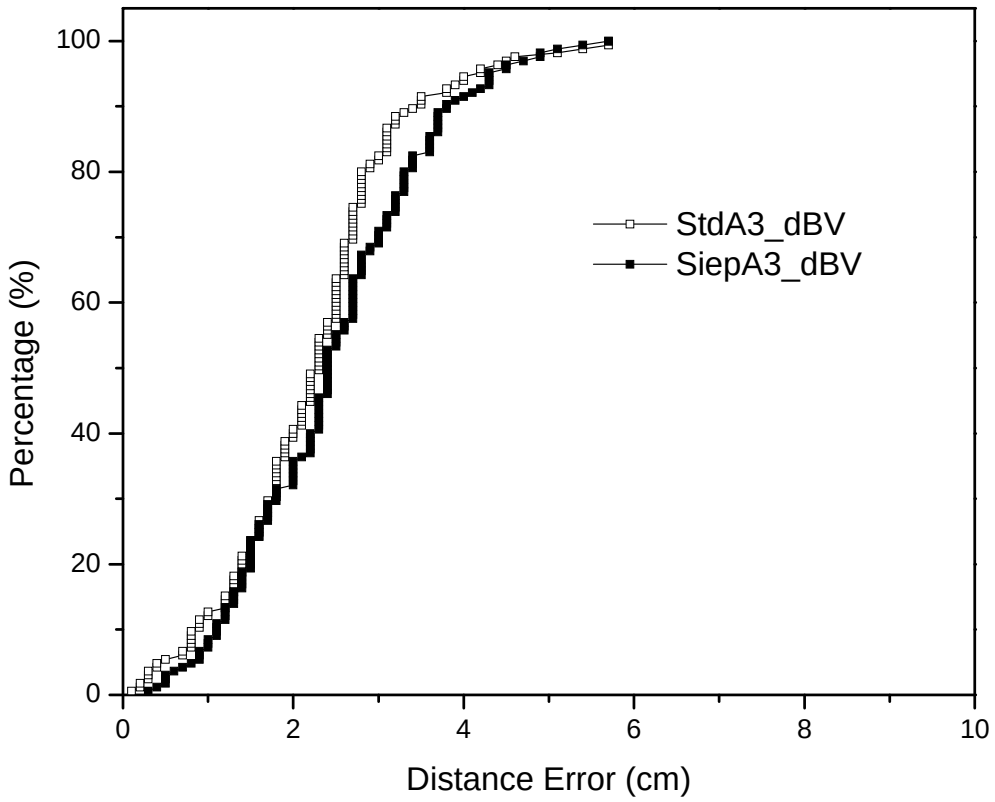

Figure 5.12: Error CDFs of method 3 on 20 cm stands and Siepel mm-wave absorber.

5.5 Mean error and standard error deviation

For further statistical analysis, the mean error and standard deviation is plotted in Figure

5.13 and the values are recorded in Tables 1 and 2.

The two dips in the plot show that using method 3 for RSS localization results in the lowest mean error. The accompanying standard deviation is also the smallest. This implies that method 3 results in the lowest localization errors and closely matches results presented in Sections 5.2 to 5.4.

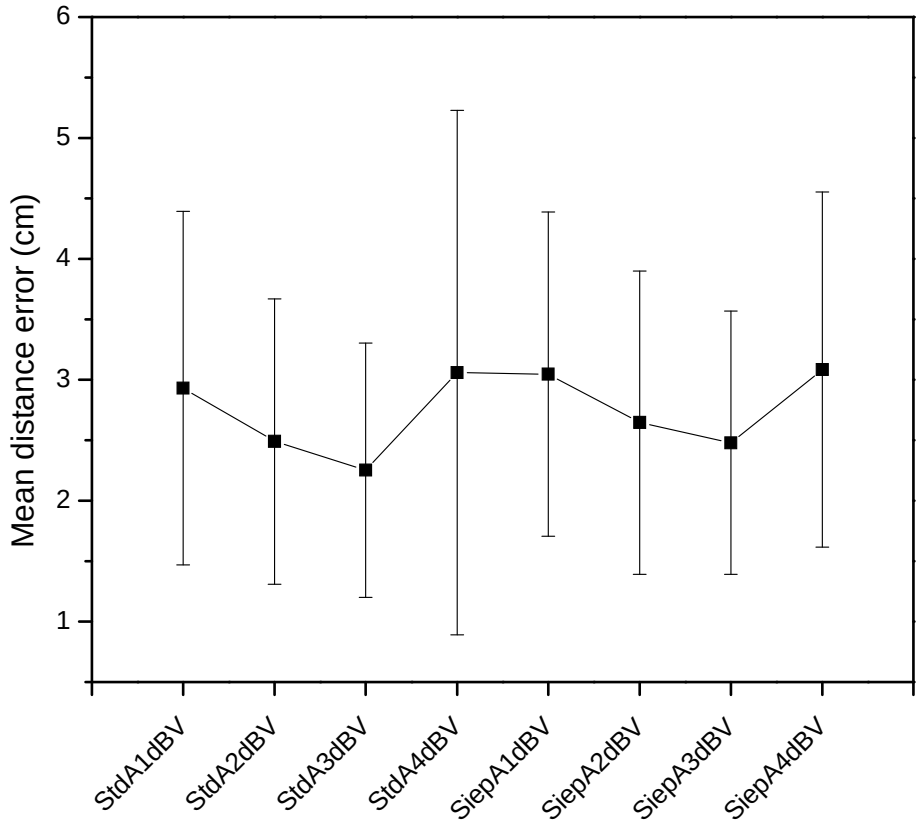

Figure 5.13: Mean and standard deviation error of the four methods on 20 cm stands and Siepel mm-wave absorber.

	Method 1	Method 2	Method 3	Method 4
Mean Error (20 cm stands)	2.9303 cm	2.4891 cm	2.2521 cm	3.0594 cm
Mean Error (Siepel absorber)	3.0472 cm	2.6454 cm	2.4794 cm	3.0842 cm

Table 1: Mean errors of methods 1 to 4, measured on 20 cm stands and Siepel mm-wave absorber.

	Method 1	Method 2	Method 3	Method 4
Std Deviation (20 cm stands)	1.4622 cm	1.1796 cm	1.0512 cm	2.1674 cm
Std Deviation (Siepel absorber)	1.3405 cm	1.2543 cm	1.09 cm	1.4685 cm

Table 2: Standard deviation error of methods 1 to 4, measured on 20 cm stands and Siepel mm-wave absorber.

5.6 Limitations

5.6.1 Localization speed

Referring to the timing diagram in Figure 3.7, the time taken to complete a localization cycle is more than 808 ms. While attempts can be made to optimize the localization algorithms, the main bottleneck lies with the time taken for the transmitters to power up. Since turning on a single component is much faster than turning on an entire transmitter chain, the time taken can be greatly reduced if the enable pin to the input or output amplifier in the transmitter can be made accessible. Currently this enable pin is not externally available.

5.6.2 Localization accuracy due to multipath effects

Fluctuation in signal levels is the main cause for errors in RSS-based distance estimations. From Appendix A, it is observed that localization errors result from the difference between these fluctuations and the generated RSS model. The problem of residues is a matter of calibration only when the fluctuations are reduced to zero.

Since most short range localization systems are meant to operate indoors, multipath is unavoidable. Nevertheless, it can be mitigated by the strategic positioning of transmitters

and receivers, the use of highly directional antennas, lining potentially reflective regions with microwave absorbers and utilizing a denser network of transmitters.

Despite all the above mentioned solutions, it is challenging to fully eradicate multipath effects and its related errors for the implementation of an RSS-based localization system.

5.6.3 Accuracy of measured RSS data

In the offline phase, the measured relationship between RSS and distance is measured manually. This can result in measurement inaccuracies due to positioning errors. Rather, a flat base mounted with a precise sliding fixture capable of micrometer adjustments for both the vertical axis and the horizontal axis will ensure positioning accuracies. Ideally, the construction of this measurement table should consist of parts that are non-metallic in nature to ensure accurate RSS readings.

5.7 Conclusion and discussion

60 GHz RSS-based localization using omni-directional antennas has been developed and tested within a 60 cm by 60 cm area. Several system considerations and positioning methods are also tested and compared in performance. From there, it is apparent that refining the estimation methods is essential in optimizing the localization accuracy.

From Figure 2.1, 60.5 GHz wave absorption due to oxygen at sea level peaks at 15.2 dB/km and decreases to 4.8 dB/km at an altitude of 20 km. This apparent large decrease might appear to have significant impact on localization performance subjected to the altitude of localization. However, translating it to the meter-range, the resulting difference is from 0.0152 dB/m at sea level to 0.0048 dB/m at a 20 km altitude. Taking reference to

the typical RSS measurement in Figure 3.6, it is observed that resulting distance errors become more pronounced with distance, with the largest distance errors of >10 cm occurring beyond 80 cm. This magnitude of distance error occurs with RSS fluctuations of approximately 1 dBV. Thus, RSS fluctuations between 0.0152 dB/m and 0.0048 dB/m are unlikely to alter localization accuracy significantly.

Section 5.1 shows that the choice of a spline look-up table derived from measured RSS in V or dBV does not impact the localization error significantly. However, because of the complexity and rigor required to spline-fit the two-dimensional measured data in V, the spline is fitted to the same data in dBV instead.

The vector plots in Sections 5.2 and 5.3 do not show any particular trend in the direction of the error. This implies that the RSS models used for the four transmitters are well matched with the propagation characteristics of the transmitters and receiver at the time of localization. No malfunctioning of transmitters can be seen. Instead, an observable trend is the increased magnitude of the vectors at the edges of the square as compared to the centre. This indicates that the accuracy of the system declines as the RSS signal of one or more transmitters diminishes below 0.3 V.

Localization on 20 cm stands and on Siepel mm-wave absorber using the four methods is discussed in Section 4.2. The trends in magnitude and direction of the localization error are compared. Of the four localization methods, method 3 (IWCOG) performs the best providing localization errors of the smallest magnitudes, cross-compared using the CDF, mean and standard deviation of the localization errors. With method 3, 90 % of the localization errors fall below 4 cm and the remaining 10 % fall between 4 to 5.7 cm on both

20 cm stands and Siepel mm-wave absorber.

Since method 1 results in a reduced localization error as compared to method 4, it is also evident that the weakest RSS contribution does not cloud location information as expected. Rather, location information can still be extracted despite the significant amount of reflections experienced at that range, leading to increased localization accuracy.

Lastly, although localization accuracy on the Siepel mm-wave absorber is slightly lower as compared to the 20 cm stands, they are comparable. For any practical localization system, it is usually convenient and aesthetically pleasing to use such low-profile mm-wave absorbers as an alternative to elevation.

Chapter 6 60 GHz RSS localization with horn antennas – Range extension

6.1 Motivation

From the empirical results in Chapter five, localization at 60 GHz using RSS can achieve mean errors of less than 3 cm. Such reduced errors are achieved by mitigating multipath effects by using Siepel mm-wave absorbers or elevating the transmitters and receivers to a height of 20 cm. However, a combination of factors, such as the high frequency and low gain of omni-directional antennas limits the localization range to a distance of 80 cm. This translates to a 60 cm by 60 cm square area, covered by four transmitters at the four corners. This can be inferred from the Pythagoras theorem as mentioned in Section 2.4.1. While applications such as ultra-fast downloading will be unaffected, this short range is a limiting factor for many other applications such as wireless high definition (Wi-HD) and ultra-fast wireless LAN where longer ranges are desired. Thus, it is imperative to increase the range of localization.

For range extension with RSS, the RSS received requires a boost when the receiver is further from the transmitters. This can be achieved with the following alternatives: increased number of transmitters, transmitters with higher output power, receivers with a larger dynamic range, or directive antennas. Out of these options, replacing the omni-directional antennas with directive antennas, while maintaining the original setup, is selected here.

6.2 System architecture and localization concept

6.2.1 System considerations with directive antennas

Following from the previous localization system, it is logical to retain the omni-directional antenna at the receiver because it is receiving from the four corners of a localization area. Thus, only the omni-directional antennas at the transmitters are replaced with directive antennas.

Achieving localization range extension with directive antennas requires a different set of considerations and concerns not addressed previously.

Firstly, while the RSSI output can be assumed to be a direct function of distance for the case of the omni-directional antenna, it no longer is the same for directive antennas. In addition to distance, the RSSI output will be dependent on the radiation pattern of the directive antenna. Although this is advantageous in AOA systems where the additional angle information is used, it adds extra challenges for RSS-based localization systems.

Secondly, it is not clear at this point how the beam-width of the directive antenna will affect localization accuracy. From the results in Chapter five, it can be gathered that the localization accuracy deteriorates when the RSS is low. Hence, for a directive antenna with a finite beam-width, localization accuracy can deteriorate if the target receiver does not reside in the major lobe of the directive antennas.

Lastly, to ensure that the entire localization area is sufficiently covered by the main beams of the four antennas, the azimuth angle of the horn antennas has to be decided.

6.2.2 Additional hardware

6.2.2.1 Directive horn antennas

From the discussion in Section 6.2.1, there are two main requirements for the directive antenna: additional gain for range extension and a wide azimuth beam-width.

While high gain antennas are commercially available, the beam-width is usually limited. The most common directive antennas at 60 GHz provides an extremely high directive gain of 24 dBi, but a narrow beam-width in the range of 10°-15°. Instead, the 60 GHz horn antenna, AT6010H, with a beam-width of 57.5° and a gain of 10 dBi was eventually obtained from Comotech. The horn antenna and the radiation pattern are shown in Figures 6.1 and 6.2 respectively.

(a) (b) (c)

Figure 6.1: AT6010H horn antenna from Comotech. (a) top-view (b) WR-15 mount (c) front view.

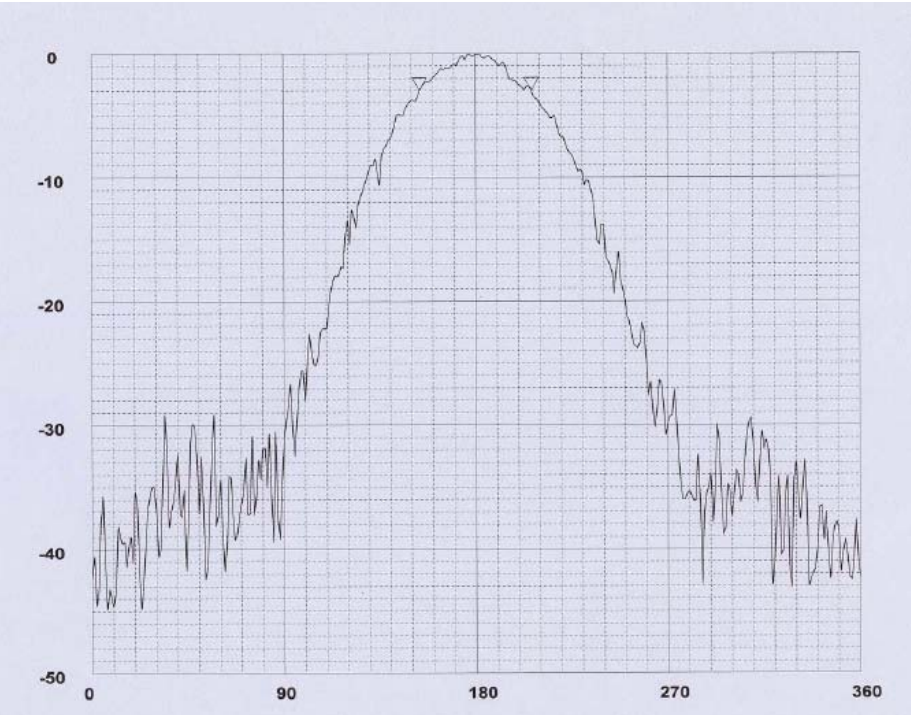

Figure 6.2: Radiation pattern of AT6010H Horn antenna supplied by Comotech.

6.2.2.2 Wooden stands

As mentioned in Section 6.2.1, the receiver retains the omni-directional antenna and the transmitters will be mounted with horn antennas. This causes a vertical mis-alignment between the receiving and transmitting antennas depicted in Figure 6.3(a). Therefore, an additional height is required at the transmitters for alignment of the receiver's omni-directional antenna with the transmitters' horn antennas. The mis-alignment is rectified with wooden stands as illustrated in Figure 6.3(b). The final setup is shown in Figure 6.4.

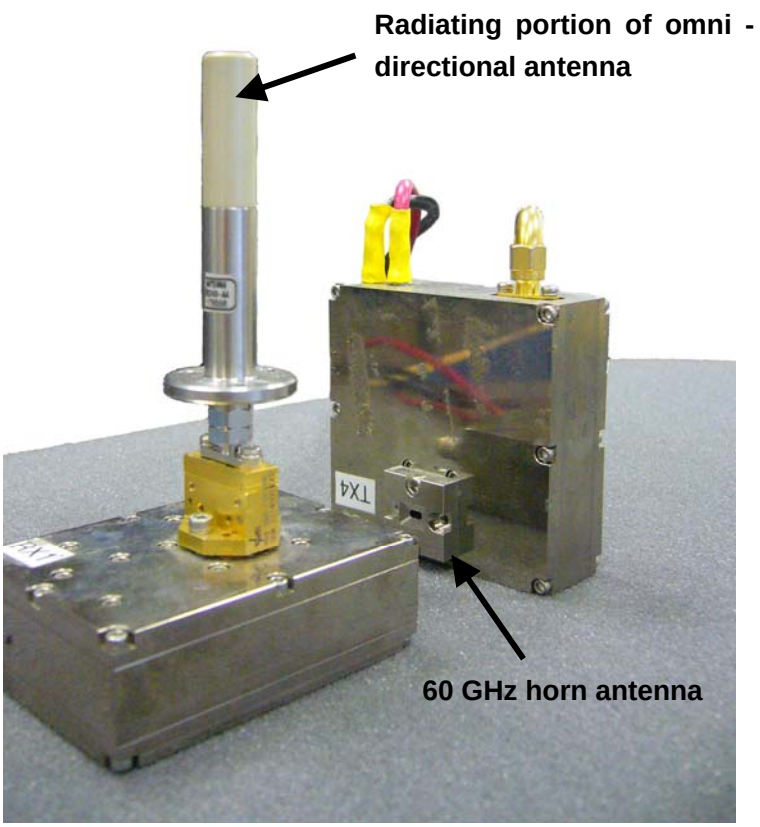

(a)

(b)

Figure 6.3:(a) Mis-alignment of receiver and transmitter antennas (b) After rectification.

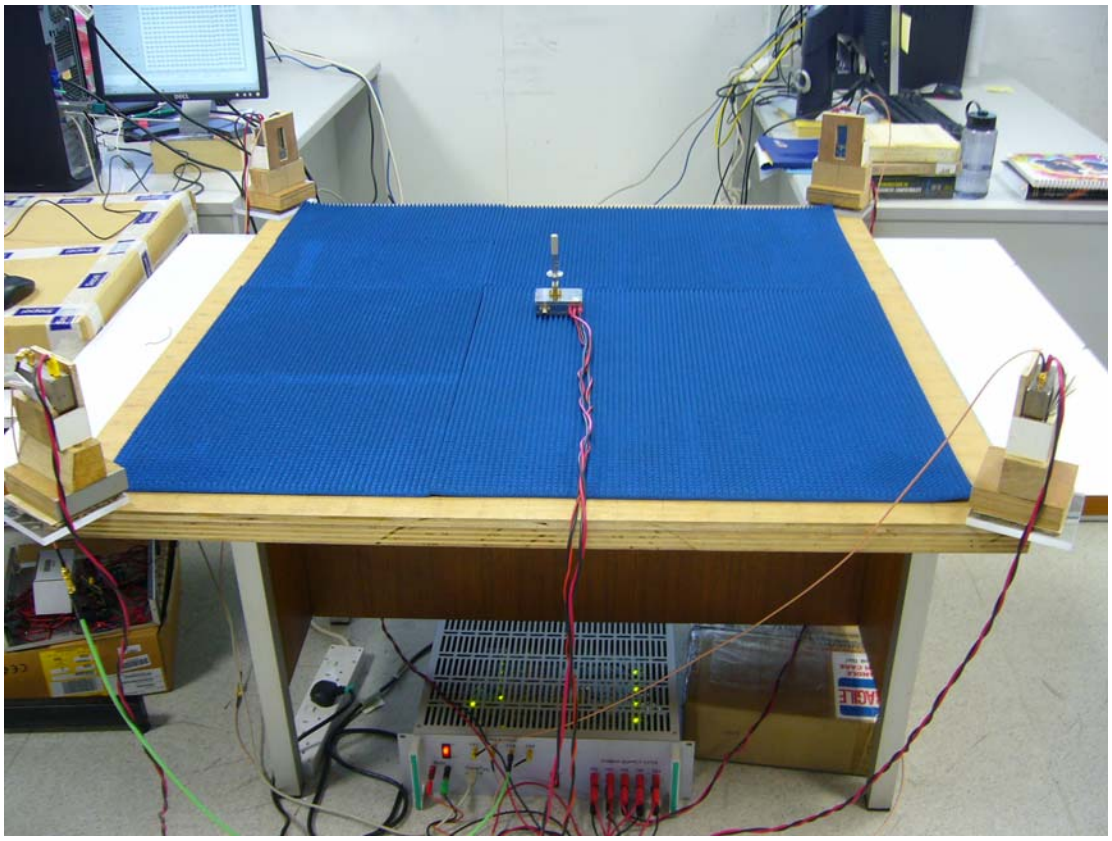

Figure 6.4: Final setup with Siepel mm-wave absorbers.

6.2.3 Range of localization

In the localization system using omni-directional antennas described in Chapter 5, the range of localization can be determined by identifying the tail portion of the RSS-distance relationship that has a low gradient where distance information is diminished. This is obvious when the relationship of the RSS is two-dimensional and is directly related to the distance.

With a horn antenna at the transmitter, the RSS is dependent on the distance of the receiver and the radiation pattern of the transmitting antenna. This implies that the RSS-distance relationship for a directive antenna system is three-dimensional. Thus the range is determined by a three-dimensional plot.

With one of the transmitters at one corner of the setup, the RSS is measured with the

receiver positioned within a 100 cm by 100 cm square wooden base in steps of 5 cm. This measurement results in a total of 437 values excluding the positions that the four transmitters are residing on. The 437 measured values are further interpolated at a resolution of 0.5 cm, as shown in Figure 6.5. The plots for the remaining transmitters are shown in Appendix C.

In Figure 6.5, it can be observed that the range of the horn antenna exceeds 1 m if the receiving antenna is in the path where the horn antenna is the most directive. However, because the 3-dB beam-width of the horn antenna is limited to 57.5° as shown in Figure 6.2, the RSS is very low, and the gradient is diminished, 100 cm away from the transmitter on the x-axis and y-axis. Thus, for an angle of ±45° from the centre of the beam-width, the range of localization is estimated to be approximately 100 cm. Noting that the gain of the antenna at the centre of the beam-width is 9 dBi more than the gain at ±45°, it is reasonable to estimate the range of each transmitter to be effective within a 100 cm by 100 cm area.

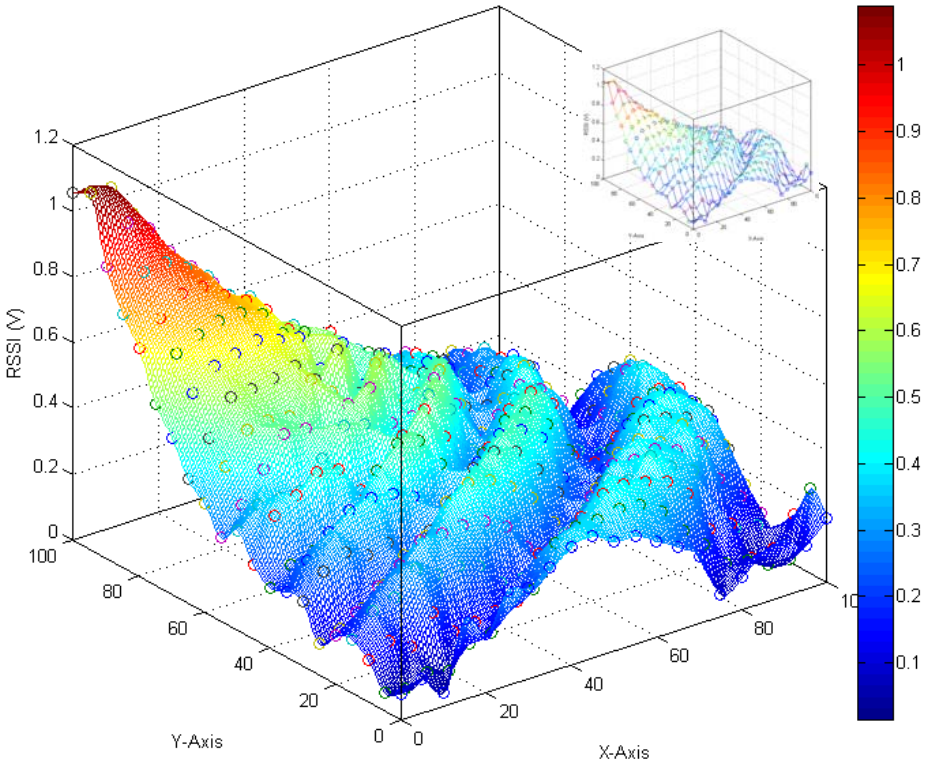

(a)

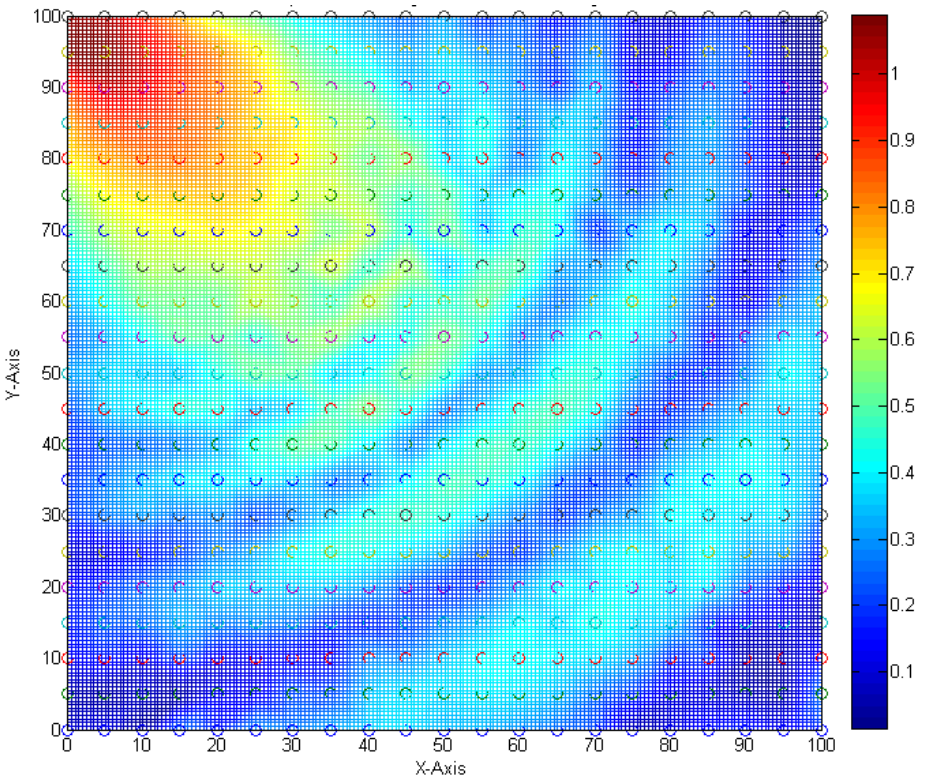

(b)

Figure 6.5: RSS plot interpolated from 437 measurements with a resolution of 0.5 cm. (a) Surface plot of TX3 at an angle of 45° in V interpolated from measured RSS values (inset) (b) top-view.

6.2.4 Fingerprinting method for RSS based localization with horn antennas

Previously mentioned in Chapter 4, there are two main RSS localization methods: Trilateration and fingerprinting.

Since the trilateration method requires the extraction of the Euclidean distance from the two-dimensional relationship between the RSS and distance, it requires the antennas on both the transmitters and the receiver to radiate isotropically in the azimuth plane.

Thus, for a localization system using directive antennas, trilateration is not suitable and the fingerprinting method will be used instead.

In the fingerprinting method, a look-up table of RSS values corresponding to predetermined positions and location is obtained during the offline phase. The size of this look-up table is dependent on the size of the localization area and resolution of the positions.

During the online phase, the system follows the timing diagram illustrated in Figure 3.7. The only difference is in the type of look-up table and the methodology of obtaining the position.

In the case of using omni-directional antennas and trilateration, the look-up table required only contains the RSS as a function of distance for each transmitter. Most of the computing power during the online phase is spent on the trilateration calculations after the Euclidean distance from each transmitter is obtained.

For fingerprinting, the system matches the real-time RSSI values in the look-up table and outputs the corresponding position. No additional computation is required. The drawback

is the large size of the required look-up table. Since a three-dimensional relationship of RSS against distance is needed for each transmitter, a much larger look-up table is needed. For a look-up table corresponding to a 5 cm square grid within a 100 cm by 100 cm area, a total of 437 x 3 data points is needed for each transmitter after discounting the four corners where the transmitters are located. If the resolution further increases to a 0.5 cm square grid, the look-up table balloons to 40397 x 3 data points for each transmitter. This contrasts greatly with 201 x 2 data points required for a system of equivalent range using the combination of omni-directional antennas and trilateration. Therefore, most of the computation for this system is spent on sifting the large look-up table to search for the matching position.

6.2.4.1 RSS matching methodologies

Two methods are considered here: (i) Pruning and (ii) Minimum RSS error.

The pruning method involves using a pre-determined range surrounding the online RSS as a condition to sift through the look-up table of RSS values. This method starts by identifying the transmitter with the largest real-time RSS. The RSS data that corresponds with this transmitter will be sifted through first. Values that fall out of the pre-determined range will be discarded together with the RSS data of the other transmitters that tags along with those values. This is repeated for the remaining three transmitters and the look-up table is pruned, up to the transmitter with the weakest RSSI value. This method, however, fails to maximize the RSS information because of the loss of information through the process of pruning.

An alternative method is to identify the correct position by considering the squared RSS error for all the points in the look-up table. The RSS error is calculated as follows:

$$Error = \sqrt{\sum_{n=1}^{4} W_n (RSS_n - RSSLU_n)^2} \quad (9)$$

Where, n = transmitter number

RSS_n = real-time RSS values for the four transmitters

$RSSLU_n$ = RSS values from the look-up table for the four transmitters

$W_n = (RSS_n/\text{Total RSS})^m$

W_n = weighting function for providing a higher weight to the transmitters that are closer to the receiver. It is optimized by varying *m* from 0 to 3.

The position that corresponds to the minimum RSS error is the final estimated position. This method assumes that a minimum RSS error corresponds to an estimated position that will result in the minimum distance error. Since this method considers every point in the look-up table, the RSS information of the look-up table is fully utilized. Hence, this method is used for this localization system.

6.2.4.2 Resolution of look-up table

RSS data is measured for the four transmitters on a 5 cm grid, within a 100 cm by 100 cm area. This gives a total of 437 x 4 sets of data, each consisting of 3 data elements; x-position, y-position and the corresponding RSS value. The isometric plots of measured RSS data belonging to the four transmitters are shown in Appendix D.

With the intention of refining the positioning error into smaller step sizes, the measured data is further spline-fitted to create a look-up table with a 0.5 cm grid resolution. The

spline is fitted using the CSAPS function found in the spline toolbox within Matlab [26]. The function returns a piecewise polynomial cubic smoothing spline based on the given data set. This results in a total of 40439 x 4 sets of data, each consisting of 3 data elements. A typical spline-approximated plot is shown in Figure 6.6.

An equivalent resolution can also be obtained with normal interpolation of all the measured data over the localization area. This will be further discussed in Section 6.5.

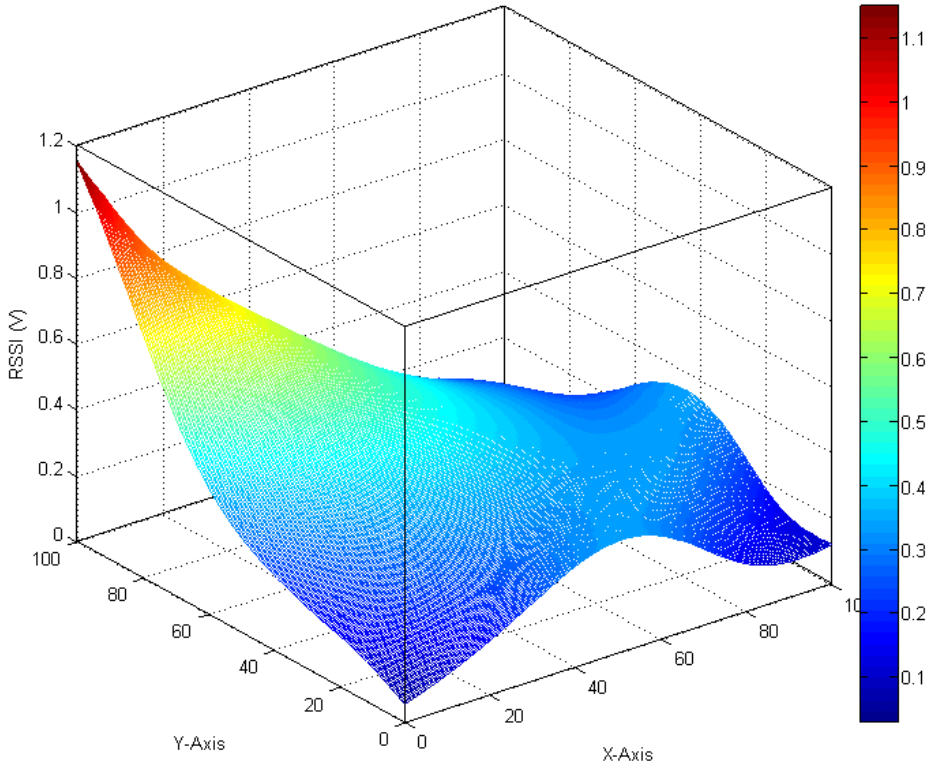

(a)

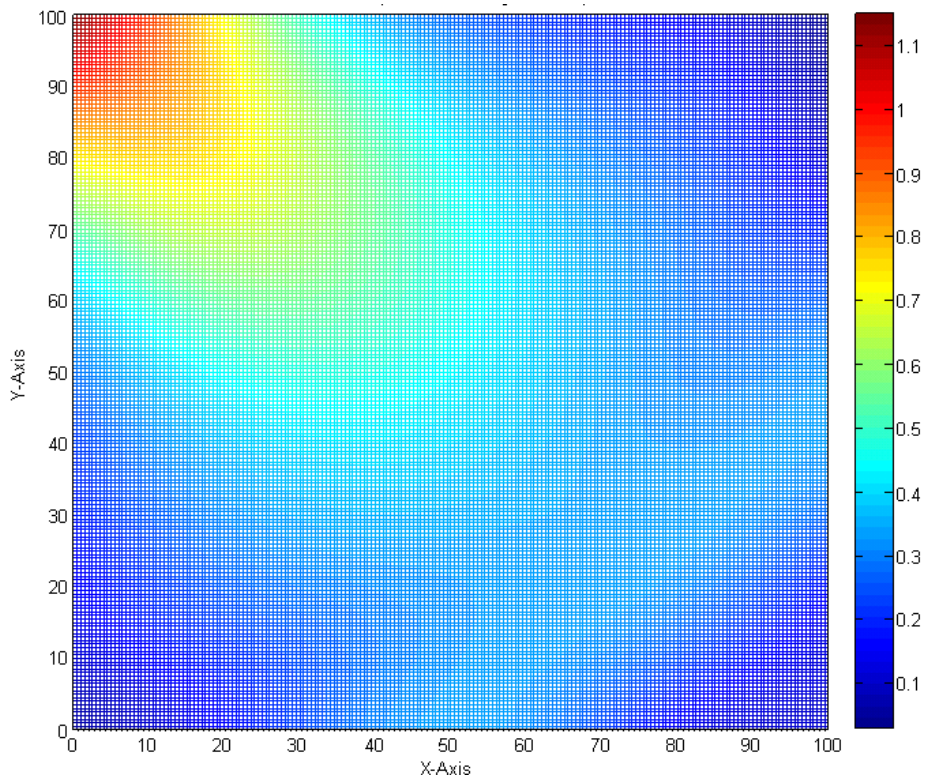

(b)

Figure 6.6: (a) 3D spline-fitted surface plot of TX3 at an angle of 45° (b) Top view.

6.2.5 Baseline setup

A setup with the following characteristics will be used in this analysis as the baseline for performance comparison:

i. Wooden platform with thickness of 1.5”

ii. Horn antennas at an angle of 27° with reference to the axis on the left of each transmitter

iii. Look-up table with a size of 40,397 data points (0.5 mm grid) created using spline-approximation of 437 measured data points (5 cm grid)

iv. Localization using fingerprinting method

v. Position estimation using minimum RSS error as mentioned in Section 6.2.4.1.

With the baseline setup as the reference, there are a few research questions that need to

be answered.

Firstly, is there a difference in localization accuracy if the look-up table of RSS values is in voltage or dBV? From the conclusion in Chapter 5, the spline-approximated look-up table required for the baseline setup can be expected to be much more tedious because the measured RSS data is three-dimensional with many large undulating gradients present in the measured RSS data.

From Figure 6.5, it seems that directing the four transmitting antennas at an angle of 45° to the center will lead to an uneven distribution of the RSS, with higher intensity at the center and lower intensity at the edges. This will result in blind spots that will affect localization performance. By changing the direction to 27° with reference to the axis on the left, can these blind spots and localization errors be reduced?

As the size of the localization area increases, effort to obtain measured RSS data for the look-up table exponentially increases. Can an interpolation or spline-approximation of a coarser grid provide similar localization accuracy?

The use of omni-directional antennas in Chapter 5 resulted in large reflections that were mitigated using mm-wave absorbers and improved localization accuracy significantly. With the use of horn antennas, the elevation beam-width is reduced, and reflections from the wooden platform are expected to be reduced. In this case, will the use of mm-wave absorbers have a significant impact in reducing reflections and thus provide improved localization accuracy?

6.3 Localization with three-dimensional spline in V and dBV

In this section, a comparison of localization accuracy between using a look-up table derived from measured RSS values in voltage or dBV is discussed. Referring to Sections 3.2 and Section 5.1, the additional complexities in spline-fitting of a two-dimensional RSS curve plotted in V is shown.

For a three-dimensional RSS plot in V, the challenge of spline-fitting is increased. Since it was also observed in Section 5.1 that spline-fitting measured RSS data in dBV can be simplified without any compromise to localization accuracy, the same is done here. By plotting in decibels, the surface plot of measured RSSI values is more linear and easier to fit with a spline.

A measured set of data plotted in V and dBV is plotted in Figure 6.7 (a)-(b) and Figure 6.8 (a)-(b) respectively. Figure 6.7 (c)-(d) and Figure 6.8 (c)-(d) show the approximated spline from the two curves. The plots belonging to the remaining transmitters in V and dBV are presented in Appendix E and F respectively.

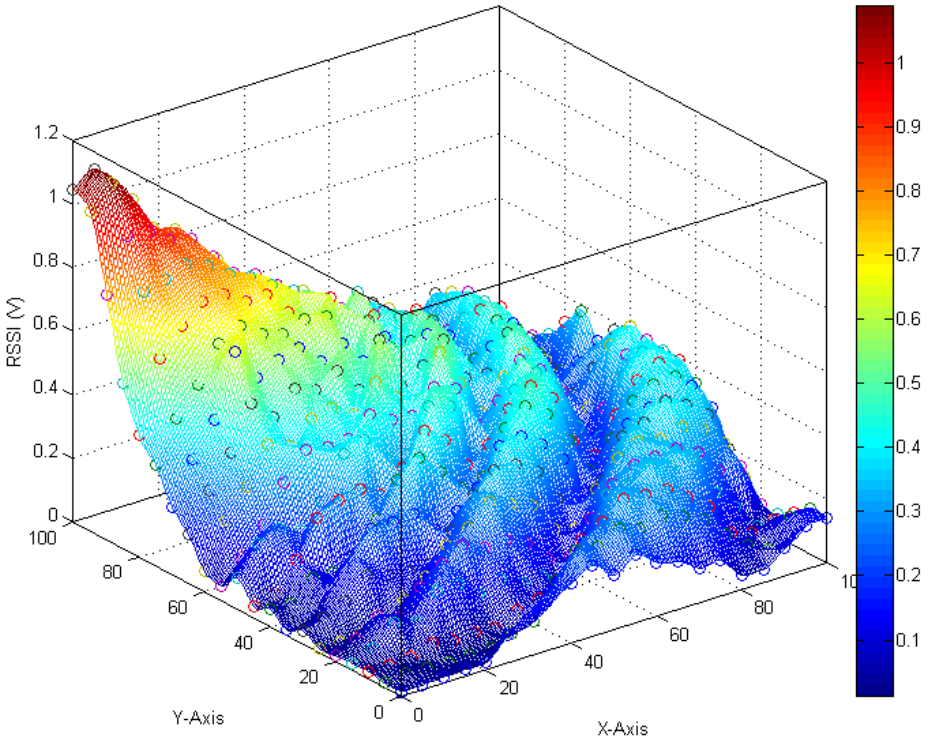
RSSI (V)
1.2
1
0.8
0.6
0.4
0.2
0
Y-Axis
100
80
60
40
20
0
X-Axis
0
20
40
60
80
1
0.9
0.8
0.7
0.6
0.5
0.4
0.3
0.2
0.1

(a)

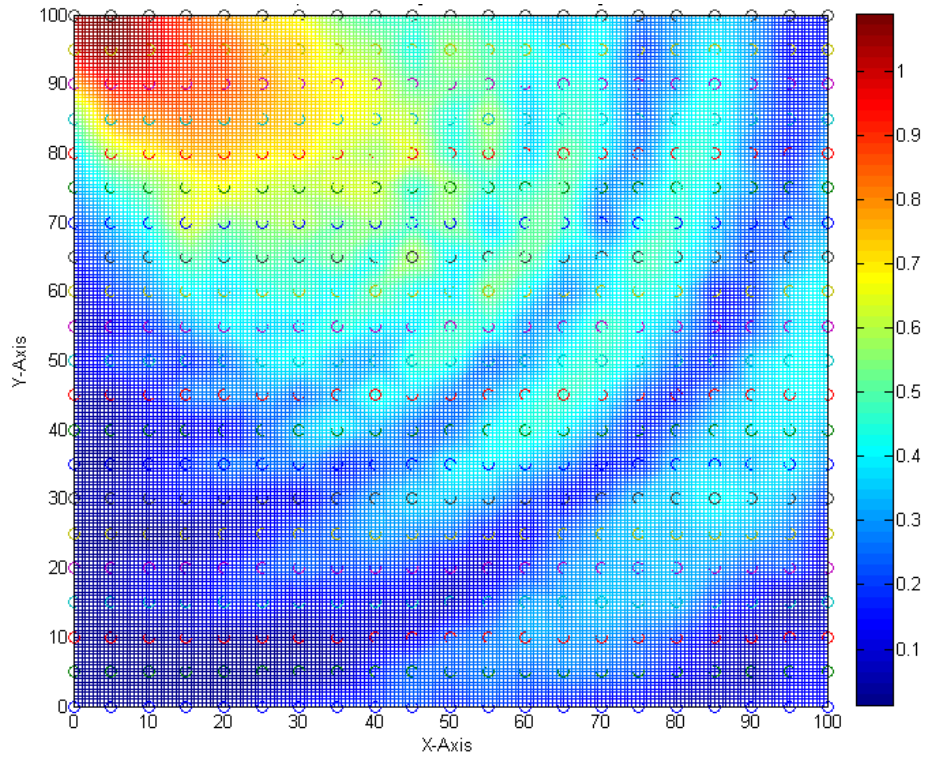
Y-Axis
100
90
80
70
60
50
40
30
20
10
0
X-Axis
0
10
20
30
40
50
60
70
80
90
100
1
0.9
0.8
0.7
0.6
0.5
0.4
0.3
0.2
0.1

(b)

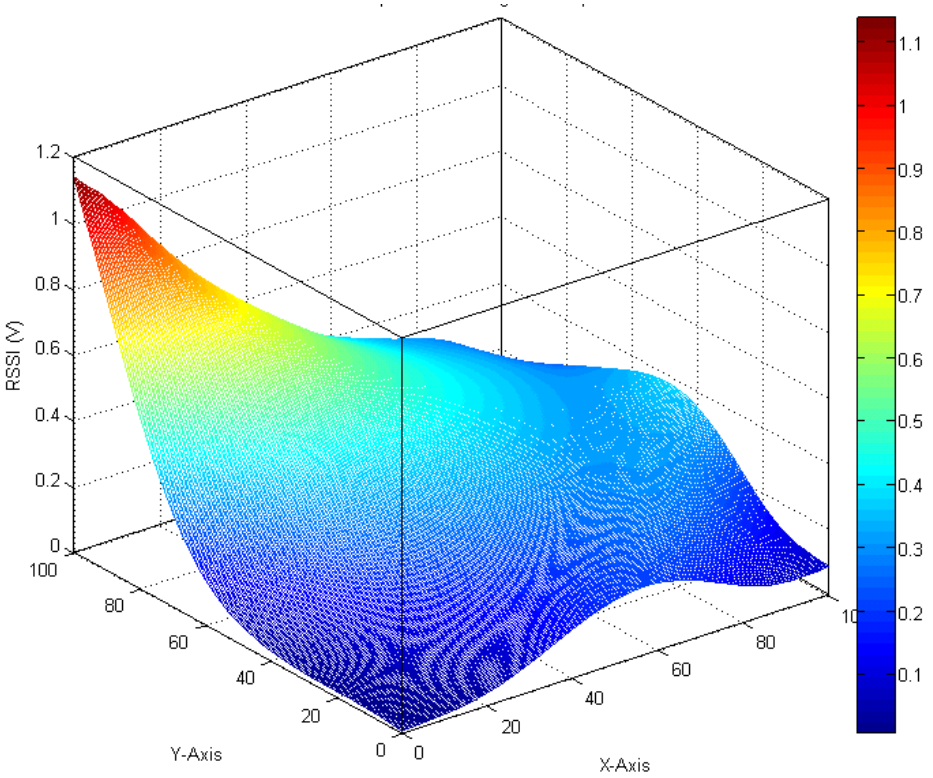

(c)

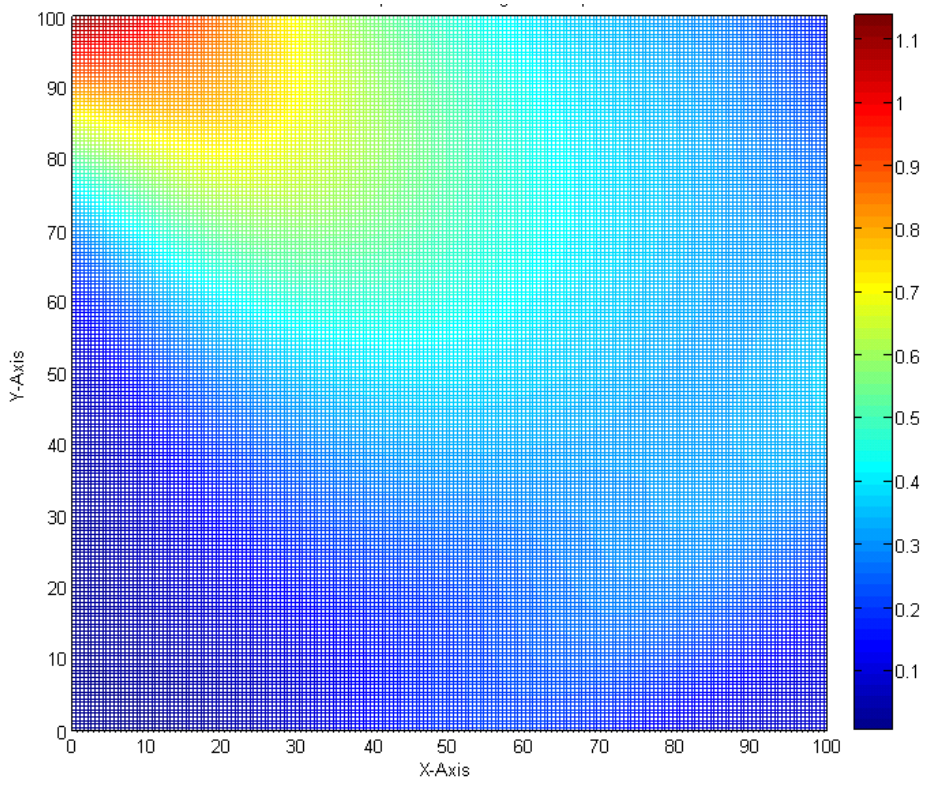

(d)

Figure 6.7: (a) 3D surface plot of TX3's measured RSSI at an angle of 27° in V (b) Top view (c) Spline-fitted curve (d) Top view of spline.

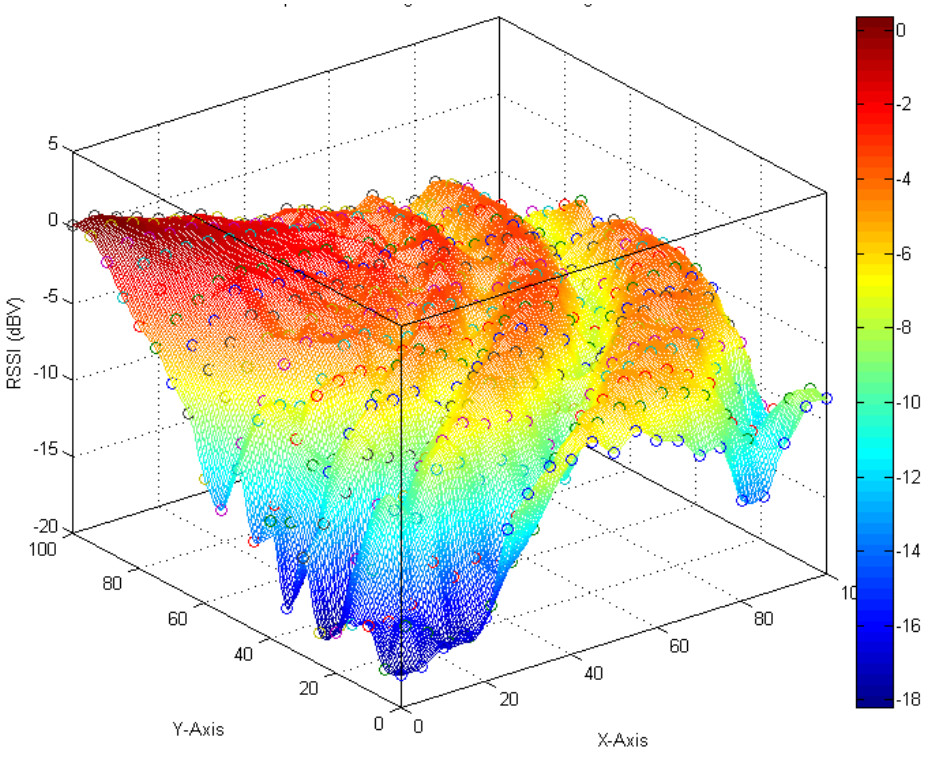
RSSI (dBV)
5
0
-5
-10
-15
-20
100
80
60
40
20
0
Y-Axis
0
20
40
60
80
X-Axis
0
-2
-4
-6
-8
-10
-12
-14
-16
-18

(a)

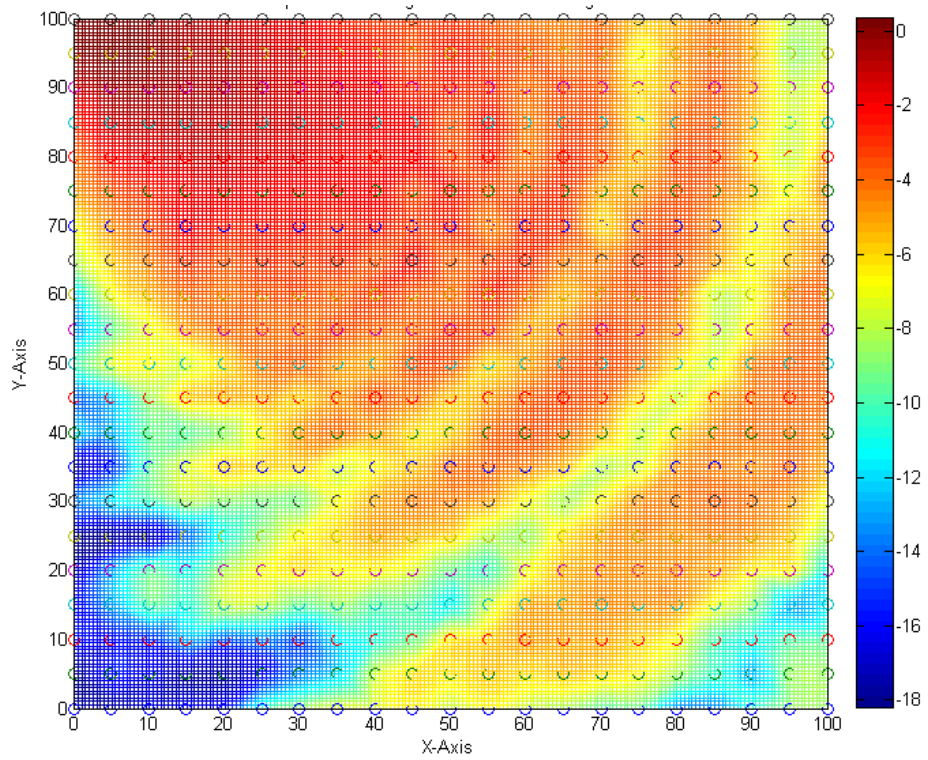
Y-Axis
100
90
80
70
60
50
40
30
20
10
0
0
10
20
30
40
50
60
70
80
90
100
X-Axis
0
-2
-4
-6
-8
-10
-12
-14
-16
-18

(b)

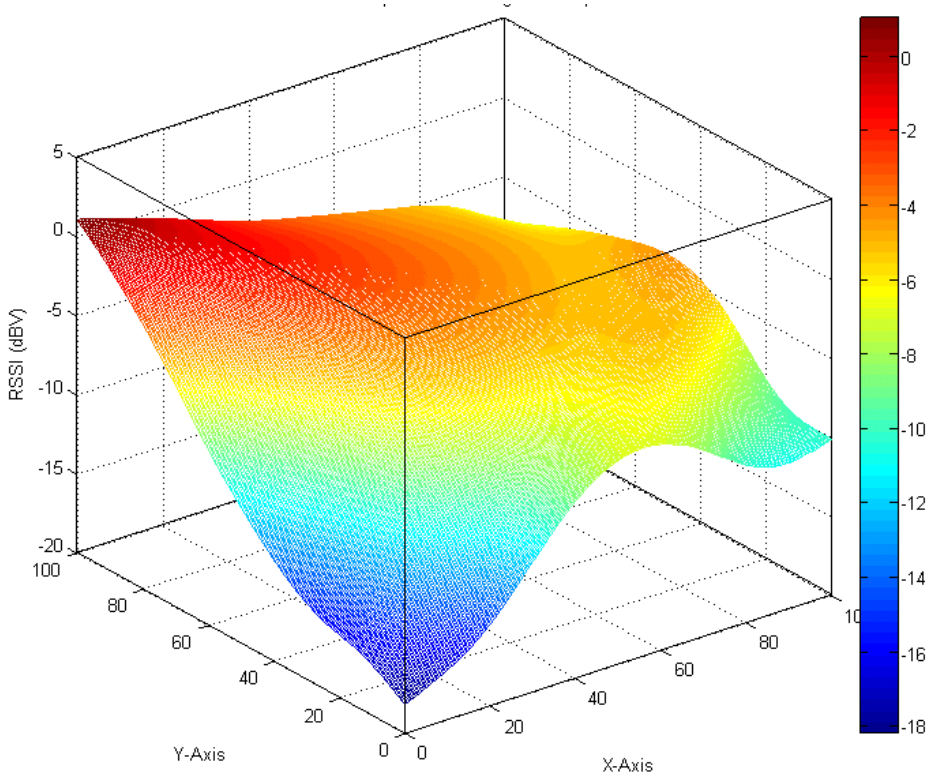

(c)

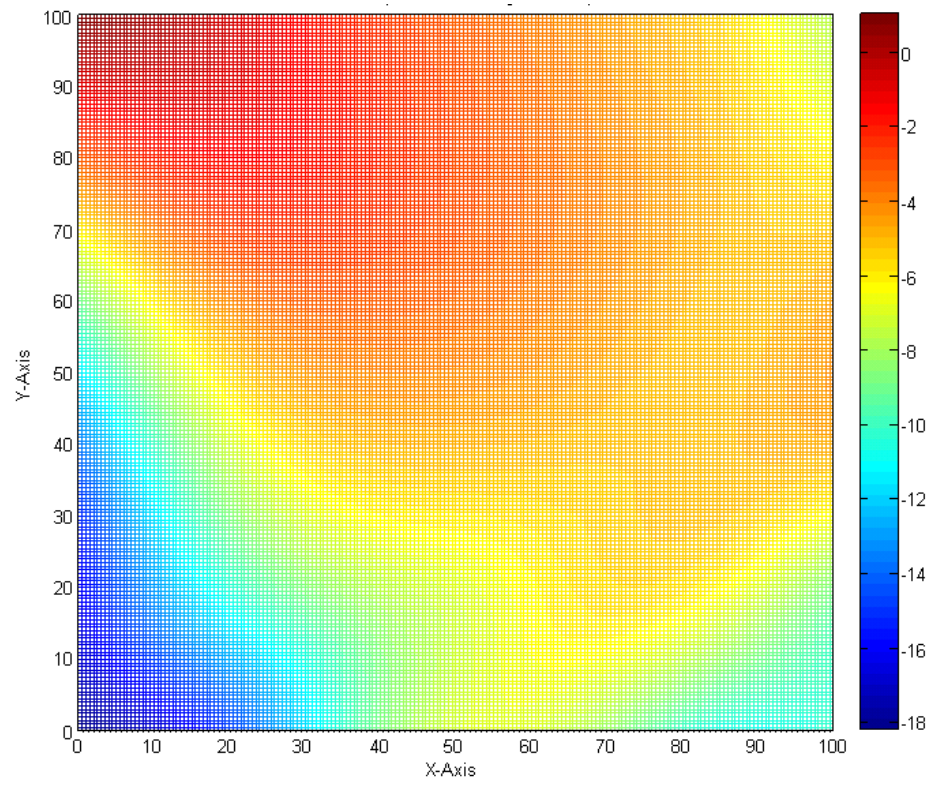

(d)

Figure 6.8: (a) 3D surface plot of TX3's measured RSSI at an angle of 27° in dBV (b) Top view of spline (c) Spline-fitted curve (d) Top view of spline.

Localization was performed using the baseline setup mentioned in Section 6.2.5 to compare the two cases. In both cases, equation (9) was used to obtain the minimum RSS error between the measured RSS and the RSS from the look-up table. The variable ‘n’ is varied from 0 to 3 in search of the optimum weighting where the mean error and the standard deviation is the lowest. The results are shown in Figure 6.9. The optimum value of n observed for the case of V and the case of dBV is 0 and 1.3 respectively. It can also be observed from the figure that the maximum distance error corresponding to the optimum n value is also the lowest for the entire range of n.

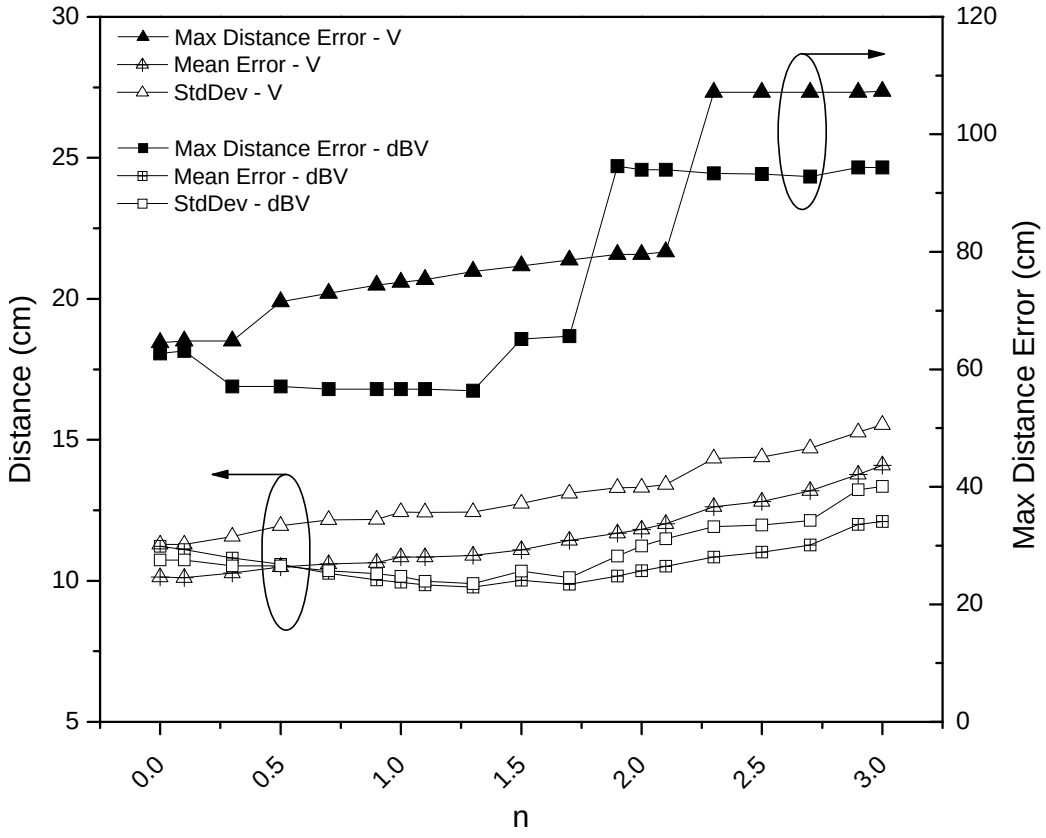

Figure 6.9: Plot of mean distance error, standard deviation and maximum distance error of localization using a look-up table derived from measured RSS values in dBV and V.

While the values in Figure 6.9 are unable to fully conclude the merits of using dBV to facilitate easier spline-approximation of the RSS values in the look-up table, the CDF

presented in Figure 6.10 shows that using either has similar performance below the 80th percentile. Beyond that, the surface spline derived from measured RSS in dBV results in reduced overall distance error and maximum distance error.

This result is expected, as the CSAPS function in Matlab is able to provide a better spline-fit for the measured RSS values in dBV, leading to better localization accuracy. This outcome is in line with the conclusion that was reached in Chapter 5. Thus, the look-up table used for localization in the subsequent sections will be derived from the measured RSS values in dBV.

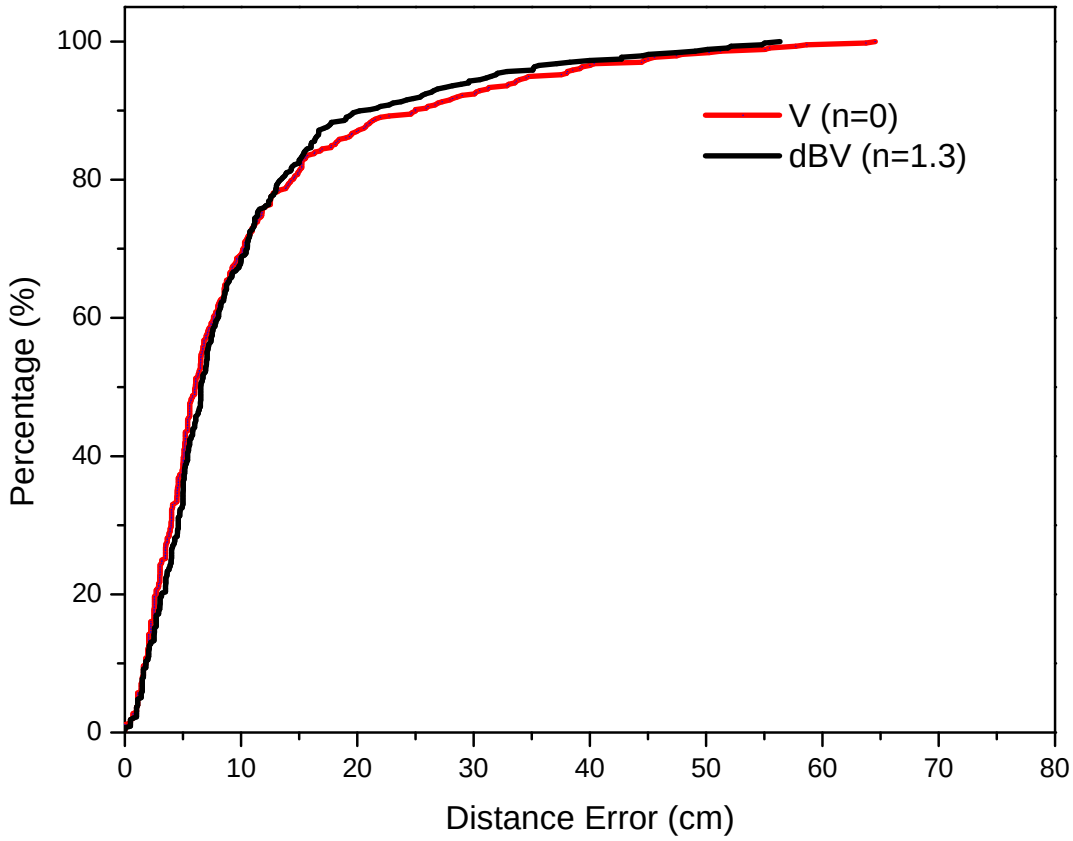

Figure 6.10: Error CDF of localization from using a look-up table derived from measured RSS in dBV and V.

6.4 Angle of horn antennas

From Chapter 5, it was observed that regions with a lower RSS resulted in poorer localization accuracy. In this system, the radiation pattern of the horn antennas results in lower RSSI values at the ±45° edge of the radiation pattern when the antennas are directed towards the centre of the 100 cm by 100 cm area. This will result in weak spots at the boundaries of the square, which will lead to larger than expected localization errors in those regions. Thus, by localizing with the horn antennas directed 27° referenced from the axis on the left of each transmitter, coverage can be maximized to the edges of the localization area.

Thus, this section presents the comparison on localization performance between the baseline system with horn antennas at a 27° and at a 45° angle.

Similar to the Section 6.3, the minimum RSS error of the two cases is calculated using equation (9) with the n value optimized for minimum mean error and standard deviation. The results are plotted in Figure 6.11. It shows that when the horn antennas are at a 27° angle, the overall mean error and standard deviation are reduced by almost 5 cm and 12 cm respectively across the n-values. Moreover, the maximum distance error registers a 30 cm reduction for n-values from 0 to 1.7. For the two cases, the minimum mean error and standard deviation corresponds to the n-value of 1.3. The CDF of both cases are presented in Figure 6.12. As expected, the CDF plot shows that errors larger than 10 cm exist in larger proportions when the horn antennas are at an angle of 45°.

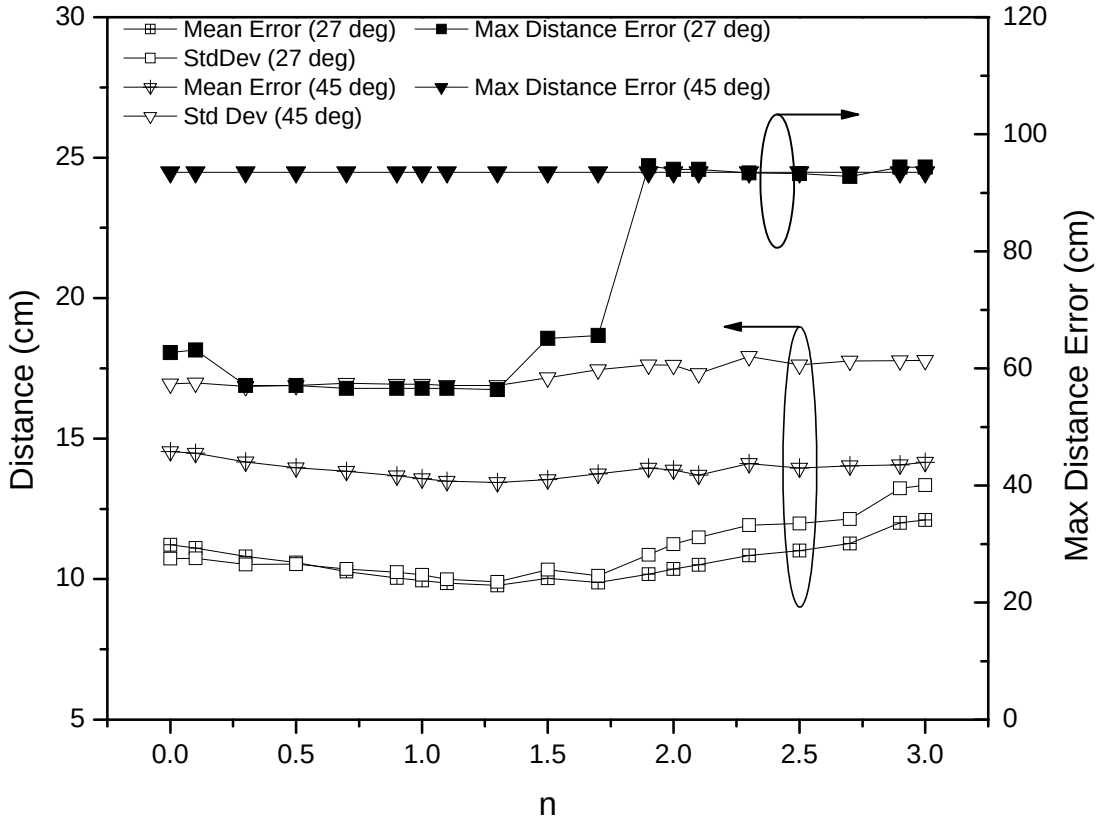

Figure 6.11: Plot of mean distance error, standard deviation and maximum distance error of localization with direction of horn antennas at 27° and 45°.

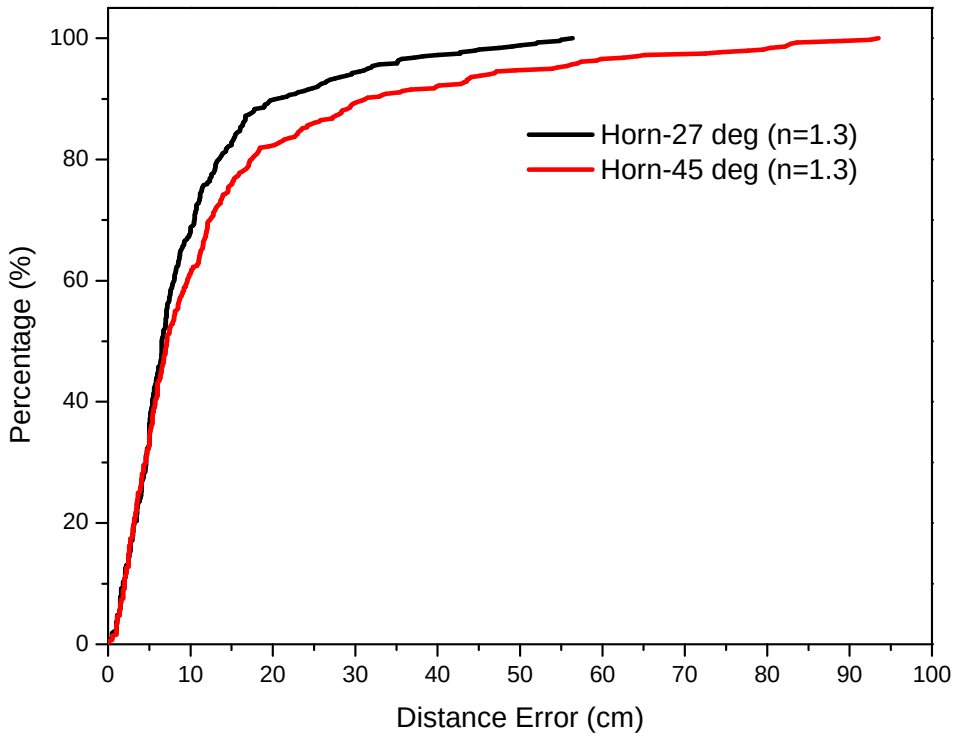

Figure 6.12: Error CDF of localization with horn antennas directed 27° and 45° from the axis on the left of each transmitter.

6.5 Spline versus interpolated data for look-up table

One main concern for RSS localization using fingerprinting is the amount of effort needed to characterize the RSS of the system in the desired localization environment. For a localization system with four transmitters within a 100 cm by 100 cm localization area and a measurement resolution of 5 cm, a total of 1,748 (437 x 4) measured RSS values are needed. To reduce the number of measurements, the localization area can be reduced. But this is usually impractical as a decent range is usually needed for more meaningful applications.

Alternatively, the measurements can be made on a coarser grid resolution, and the look-up table can be generated via interpolation or a spline-fit, thus reducing the accuracy of the look-up tables. The question then is how this inaccuracy impacts the localization error.

Localization with look-up tables derived from RSS values measured on 10 cm and 20 cm grids are explored and the resulting error CDFs are plotted in Figure 6.13. With the error CDF resulting from look-up tables derived from a 5 cm grid as a baseline, it is observed that reducing the resolution to a 10 cm grid and 20 cm grid does reduce localization accuracy, however, marginal. At the 80^{th} percentile, localization error due to the spline-fitted look-up table at 5 cm, 10 cm and 20 cm grid resolution is 13.5, 15.0 and 17.3 cm respectively. For the look-up table that is interpolated from a 10 cm and 20 cm grid resolution, localization error is 16.1 and 17.1 cm at the 80^{th} percentile respectively.

This shows that localization error is comparable to the baseline case when the look-up table is derived from RSS values measured on a coarser grid.

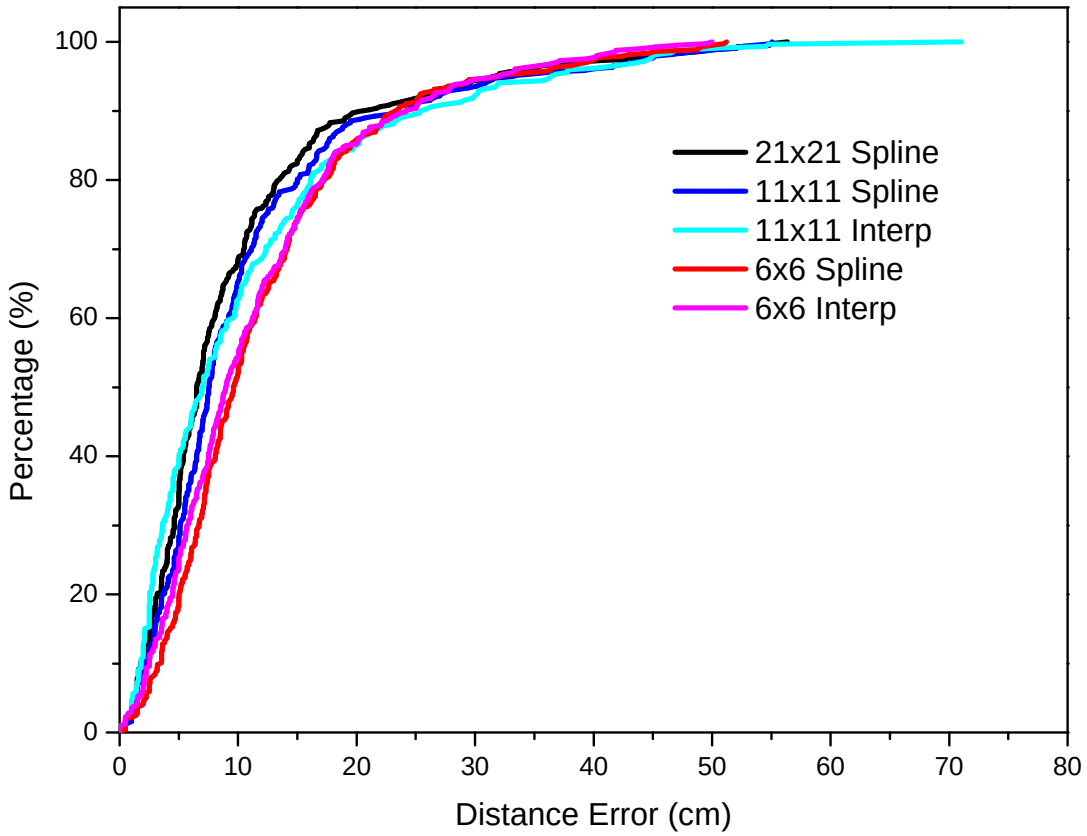

Figure 6.13: Error CDF of localization from using look-up tables derived from RSS values measured on 5 cm grid (21 x 21 values), 10 cm grid (11 x 11 values) and 20 cm grid (6 x 6 values).

6.6 Localization with and without Siepel mm-wave absorber

To further improve the localization performance, Siepel mm-wave absorbers are placed on the wooden base. The RSS of the four transmitters are measured on a grid of 5 cm resolution and fitted with splines. The surface plots of the measured RSS and splines are presented in Appendix G. With the addition of the Siepel mm-wave absorber, it can be observed from those plots that some irregularities in the RSS are reduced.

Localization is performed and the analysis in Figure 6.14 shows that the optimum n value is 1.7. A comparison between the error CDFs belonging to the localization setup with and without (i.e. Baseline setup) the Siepel mm-wave absorbers is presented in Figure 6.15.

From Figure 6.14, the optimum n value for localizing on Siepel mm-wave absorbers is 1.7. It can be seen that both the mean error and the standard deviation achieve a reduction of approximately 3 cm as compared to the baseline setup. By using Siepel mm-wave absorbers, the CDF in Figure 6.15 also shows improved performance. At the 90th percentile, the distance error is only 14 cm as compared to the baseline setup (21 cm).

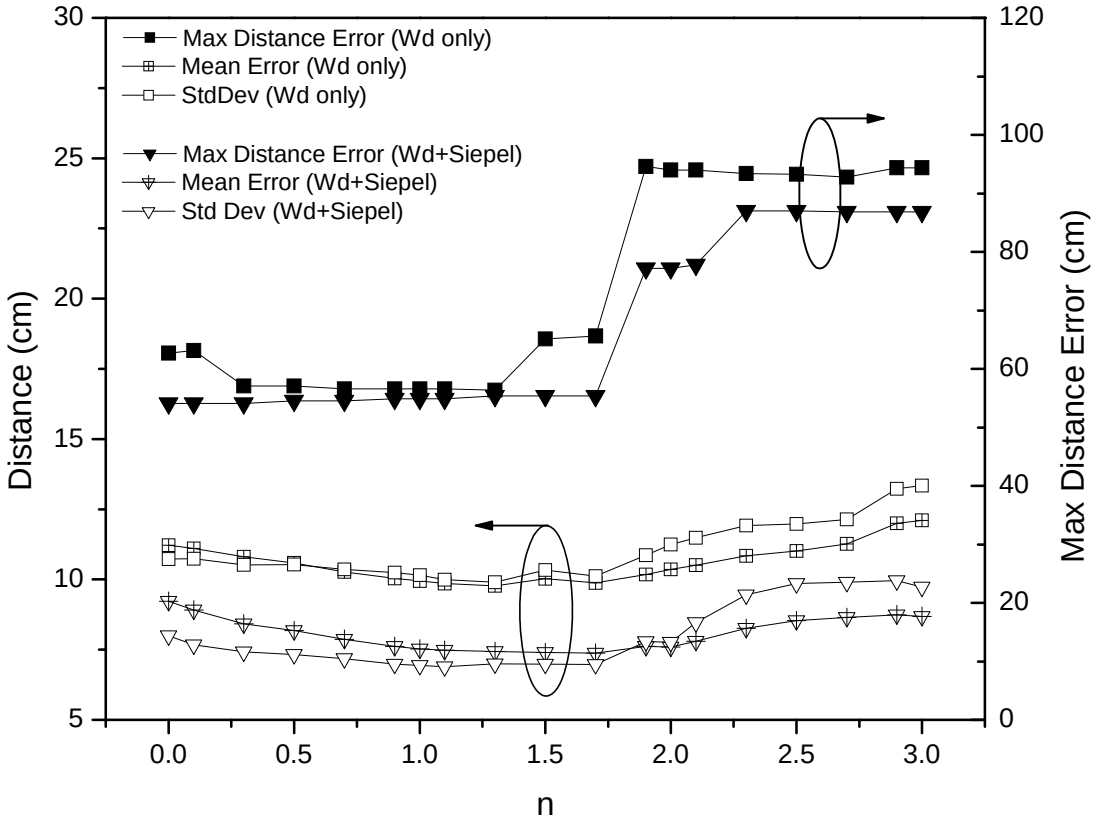

Figure 6.14: Plot of mean distance error, standard deviation and maximum distance error of localization with and without Siepel mm-wave absorbers.

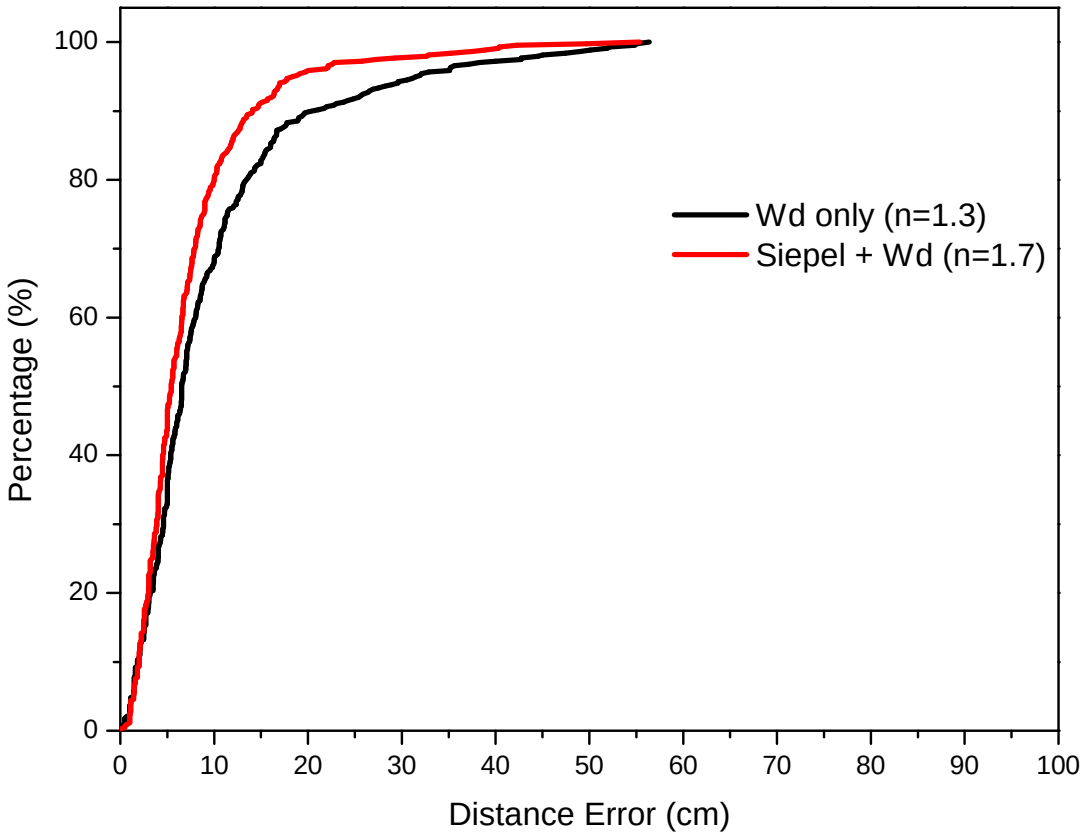

Figure 6.15: Error CDF of localization with and without Siepel mm-wave absorbers.

6.7 Conclusion and discussion

In a bid to extend the area of localization from a 60 cm by 60 cm area to 100 cm by 100 cm area, the omni-directional antennas at the transmitters are replaced by horn antennas with a gain of 10 dBi and a 3 dB beam-width of 57.5°. As discussed in Section 6.2.4, fingerprinting with a look-up table is used for real-time localization because the trilateration method is unable to be implemented with the use of horn antennas.

On the assumption that the minimum difference between the RSS in the look-up table and RSS of real-time measurement corresponds to the estimated position with minimum localization error, several experiments were carried out and compared.

In line with the results from Section 5.1, Section 6.3 discusses about attaining a better

spline-fit of measured RSS values in dBV, which leads to better localization accuracy.

Due to the limited beam-width of the horn antenna, the azimuth angle of the main beam belonging to the horn antennas becomes an essential consideration. Section 6.4 presents an improvement in localization accuracy at an angle of 27° as compared to 45°. This is due to the increased 'blind spots' introduced at the edges within the 1 m^2 area when the horn antennas are at a 45° angle.

Measurement effort can also be greatly reduced without significantly compromising the localization accuracy. As discussed in Section 6.5, using 50 % less measurement points only results in a 1.5 cm increase in localization errors at the 80^{th} percentile. This will be useful if localization in a larger space is required.

Thus far, optimum localization accuracy is obtained by the system using directional antennas with the following parameters:

- Spline look-up table fitted to the RSS plot in dBV, measured on a 5 cm grid.
- Horn antennas at 27° from the left hand axis of the transmitter.
- Siepel mm-wave absorber on top of the 1.5" wooden base.

For this system, the mean error and standard deviation are 7.4 cm and 6.9 cm respectively. At the 80^{th} and 90^{th} percentile, the localization error is 10 cm and 14 cm respectively.

In comparison with the localization system using omni-directional antennas, the localization errors have increased. This is expected, as the range has increased and the resolution of the measured RSS has decreased. In the localization system using omni-directional antennas, RSS measurements were obtained in steps of 0.5 cm. When

directional antennas are used, RSS measurements are obtained on a 5 cm (10x reduction in resolution) grid instead. Moreover, increased errors in spline-fitting a three-dimensional set of data are expected, resulting in poorer localization accuracy.

Chapter 7 Conclusions and recommendations

RSS-based localization at 60 GHz is one of the simple alternatives to indoor positioning with high data-rate transfer for future intelligent home systems. In this dissertation, the system architecture, hardware, software and localization methods are first discussed and presented. Several decisions, such as the use of omni-directional antennas set up the stage for the study of RSS-based localization using mm-waves.

Based on the initial measurement results of wave propagation at 60 GHz, reflections from the formica-laminated table cause significant fluctuations in the RSS that introduces ambiguity in distance estimates for any particular RSSI value. While this ambiguity can be resolved with a spline-fit, the fluctuations in RSS can cause the localization system to be grossly inaccurate. Additionally, the behavior of the wave changes with the surface of the table. Since wood provides attenuation of 20-40 dB at 60 GHz, RSS measurements were performed on 0.5” 1”, 1.5” and 2” thick wooden bases. In each set of measurements, each wooden base was placed on top of the formica-laminated table with and without a metal plate in-between, and the difference in the two sets of data is compared. The measurement results show that the 1.5” and 2” thick wooden base result in the lowest difference between the two sets of data. This implies that wave propagation behavior is consistent on these two wooden bases even when placed on a different surface. Moreover, these wooden bases also reduce the magnitude of RSS fluctuations. Thus, the 1.5” thick wooden base is used throughout the project to ensure consistency.

Despite the introduction of the 1.5” thick wooden base, significant fluctuations in RSS remain. This is especially pronounced at distances beyond 60 cm. Further reduction in

reflections was successfully achieved by elevating the transmitters to a height of 20 cm and using Siepel mm-wave absorbers on the wooden base.

With the hardware in place, localization experiments are carried out across various RSS positioning methods such as the COG (with four RSS readings and three largest RSS readings), WCOG and IWCOG methods. Results show that the weighted methods have superior localization accuracy as compared to the non-weighted methods. Between the WCOG and IWCOG methods, the IWCOG method extracts positioning information most accurately for both cases of the 20 cm stands and mm-wave absorber, resulting in localization error of only 3.5 cm and 3.8 cm respectively at the 90^{th} percentile within a 60 cm by 60 cm area. The mean error and standard deviation for both cases are also the lowest among the four methods at 2.4 cm and 1.1 cm respectively. The worst performing method is the COG method using only the three largest RSS values. The localization error at the 90^{th} percentile is approximately 5 cm within a 60 cm by 60 cm area. The mean error and standard deviation are also the highest of the four methods. The mean error for both the 20 cm stands and mm-wave absorber is approximately 3.1 cm. The standard deviation for the 20 cm stands and mm-wave absorber is 2.2 and 1.5 cm respectively.

In all the cases, the vector plots of distance errors do not show any particular directional trend. It does, however, show that the error magnitude is diminished towards the centre and is increased towards the borders of the 60 cm by 60 cm area. This is because the transmitters that are further away output lower RSSI values, resulting in less accurate distance estimation.

The CDFs of localization errors also show that the Siepel mm-wave absorber is able to

reduce multipath effects to a degree that is similar to raising the transmitters and receiver by 20 cm. This implies that these two methods of reducing reflections can be implemented interchangeably.

For further development, the following recommendations can be carried out:

- Reduce the time for localization. This can be achieved either by using transmitters with faster power-up or with an accessible transmit enable pin.
- Increase the accuracy of measurements. RSSI measurements and localization experiments should be performed on a precision positioning table with precise sliding fixtures capable of micrometer adjustments. The base should be made of wood and the sliding fixtures made of non-reflective materials.
- Supplement measurement results with statistical studies such as Monte Carlo simulations. This analyzes the system performance more thoroughly and can lead to the development of a more robust system. This will be especially helpful for a more complex system using directive antennas or for localization in a three-dimensional space.
- Localize multiple receivers. With multiple receivers within the localization area, they can interfere with one another's RSS signals. This has to be mitigated in many practical scenarios where multiple targets exist.
- Characterize and localize in a three-dimensional space. Although 3-D localization is complex, it opens up more applications. An investigation involving methods for measurement and localization in a 3-D space is recommended.

Due to the limited sensitivity of the receiver, RSS plateaus beyond 80 cm, and localization

is limited to a 60 cm by 60 cm area. This limits the number of useful applications. Thus, in an attempt to enlarge the localization area to a 100 cm by 100 cm area, the 2 dBi omni-directional antennas at the transmitters are replaced with 10 dBi horn antennas. The range extension, however, comes at the price of complexity and accuracy. Since trilateration can no longer be used because of the radiation pattern of the antenna, fingerprinting was implemented. Instead of a two-dimensional dataset used in trilateration, a three-dimensional dataset is required for fingerprinting. This increases the amount of effort significantly in both the offline and online phases. In the offline phase, RSS measurements for each transmitter are increased by 20 times for a 100 cm by 100 cm area with a resolution of 5 cm. For a 100 cm by 100 cm area with a resolution of 0.5 cm, the size of the RSS dataset increases by 200 times. Processing data of this size in the online phase is challenging and computationally intensive. While little can be done to reduce the size of the RSS dataset used in the online phase, measurement effort can be significantly reduced in the offline phase by reducing the resolution to a 10 cm and 20 cm grid during measurement. Measurement results show that localization performance does not degrade significantly from doing so.

A comparison is made with the azimuth angles of the horn antennas at 27° and 45°, and a significant improvement in localization accuracy is observed for the angle of 27°. Since directive or horn antennas have a limited beam-width, a poor choice in angle can result in increased blind spots at the edges of the localization area that will lead to large errors.

Localization with the baseline setup on mm-wave absorbers further reduces RSS fluctuations. This combination further reduces localization error to 14 cm at the 90th

percentile for a 1 m^2 area. Although this magnitude of error is significantly more than the previous setup using omni-directional antennas, the localization area is almost three times larger. Moreover, the magnitude of error is not extreme and can still be tolerated in a practical indoor localization system.

In addition to the recommendations for the case of using omni-directional antennas, the following is recommended:

- Further optimize the azimuth angle of the horn antennas. The transmitters can be rotated from 0° to 90° in steps of 10° and the localization errors compared in search of the optimum angle. Further analysis can be carried out with this analysis to determine the relationship between the antenna's beam-width and this optimum angle.
- Use fan-beam horn antennas instead. Since fan-beam horn antennas have a wider azimuth beam-width and a much narrower elevation beam-width, blind-spots can possibly be reduced at the edges of the localization area. Moreover, the narrow elevation beam-width will also reduce reflections from the wooden base. The contribution from both factors will lead to increased localization accuracy. This improvement can be further explored.
- Exploit angle information. While having a radiation pattern increases the difficulty in implementing trilateration, it provides additional direction information. A possible way is to install PC-controlled rotating stands under the four transmitters and they can be rotated while localizing the receiver to obtain angle information. This additional information will further refine the localization accuracy.

The main advantage of RSS-based localization at 60 GHz is the simplicity of development and implementation. Through this research, it can be seen that the use of RSS is under-appreciated, resulting in increased research attention moving towards the rest of the localization methods such as TOA, TDOA and AOA. With RSS-based localization using simple trilateration and fingerprinting methods, localization error at the 90^{th} percentile is 3.5 cm for a 60 cm by 60 cm area and 14 cm for a 100 cm by 100 cm area respectively.

Bibliography

[1] The Robinson Rojas Archive, States and Markets Report 2009. Retrieved October 10th, 2009 from http://www.rrojasdatabank.info/wdi2009/statesmarkets.pdf.

[2] IEEE 802.11n-2009. In Wikipedia, The Free Encyclopedia. Retrieved October 10th, 2009, from http://en.wikipedia.org/w/index.php?titl…http://en.wikipedia.org/wiki/IEEE_802.11n-2009.

[3] IEEE 802.15 WPAN Task Group 3c (TG3c), Millimeter Alternative Phy. Retrieved October 10th 2009, from http://ieee802.org/15/pub/TG3c.html.

[4] R. C. Daniels and R. W. Heath Jr., "60GHz Wireless Communications: Emerging Requirements and Design Recommendations", *IEEE Vehicular Technology Magazine*, September 2007

[5] L. M. Correia and P. O. Frances, "A Propagation Model for the Estimation of the Average Received Power in an Outdoor Environment in the Millimetre Waveband", *IEEE 44th Vehicular Technology Conference,* p 1785-8 vol.3, 1994.

[6] S.W. Wales, D.C. Rickard, M.A. Beach and R. Davies, "Measurement and Modelling of Short Range Broadband Millimetric Mobile Communication Channels", *IEE Colloquium on Radiocommunications in the Range 30-60 GHz,* p 12/1-6, 1991.

[7] R. Janaswamy, "An Indoor Pathloss Model at 60 GHz Based on Transport Theory", *IEEE Antennas and Wireless Propagation Letters,* v 5, n 3, p58-60, 2006.

[8] T. H. Ngoc et al., “Indoor Multipath Propagation Characteristic at 60GHz”, *TENCON 2006,* p 4, 2006.

[9] G. Y. Delisle, “ Implementation of wideband indoor wireless systems at millimeter wave frequencies”, *1996 IEEE International Conference on Personal Wireless Communications Proceedings and Exhibition,* p 48-51, 1996.

[10] Atushi Yamamoto et al., ”Path-Loss Prediction Models for Intervehicle Communication at 60 GHz”, *IEEE Transactions on Vehicular Technology,* v 57, n 1, p 65-78, Jan. 2008.

[11] M. Stella, M.Russo, D. Begusic, “Location Determination in Indoor Environment based on RSS Fingerprinting and Artificial Neural Network”, *9th International Conference on Telecommunications - ConTEL 2007*, p 301-6, 2007.

[12] X. Huang, “Antenna Polarization as Complementarities on RSSI Based Location Identification”, *4th International Symposium on Wireless Pervasive Computing (ISWPC 2009)*, p 5 pp., 2009.

[13] A. Awad, “Adaptive Distance Estimation and Localization in WSN using RSSI measures”, 2007 10th Euromicro Conference on Digital System Design: Architectures, Methods and Tools, pp. 452-9, 2007.

[14] A. Hatami, K. Pahlavan, “Performance Comparison of RSS and TOA indoor geolocation based on UWB measurement of channel characteristics” 17th International Symposium on Personal, Indoor and Mobile Radio Communications, pp. 6, 2006.

[15] F. Winkler et al., “A 60 GHz OFDM Indoor Localization System Based on DTDOA”,

4th Information Society Technologies Mobile and Wireless Communications Summit, 2005.

[16] D. Dardari and V. Tralli, “High-Speed Indoor Wireless Communications at 60 GHz with Coded OFDM”, *IEEE Transactions on Communications*, v 47, n 11, pp. 1709-1721, Nov 1999.

[17] H. J. Liebe, G. A. Hufford and R. O. Debolt, “Atmospheric 60 GHz Oxygen Spectrum: Modeling and Laboratory measurements and line parameters”, *National Telecommunications and Information Administration, NTIA-91-272,* p 171, Mar. 1991.

[18] W. G. Read et al., “The Measurement of Absolute Absorption of Millimeter Radiation in Gases: The Absorption of CO and O_2”, *IEEE Transactions on Antennas and Propagation,* v. 36, no.8, p 1136-1143, Aug. 1988.

[19] Tutorial on Airborne Microwave Temperature Profilers. Retrieved 10th October, 2009 from http://brucegary.net/MTP_tutorial/OxyAbsSpec.png.

[20] A. Bensky, *“Wireless Positioning Technologies and Applications”, Artech House 2008.*

[21] L. M. Correie and P. O. Frances, “Transmission and Isolation of Signals in Buildings at 60 GHz”, *Sixth IEEE International Symposium, PIMRC'95*, p 1031-4 vol.3, 1995.

[22] G. Riva, V. D. Esposti, E. D. Ponti, L. Ferrucci, E. Papa, “Characterization of mm-wave Indoor Propagation with Directive Antennas”, *European Microwave Conference*, v 1, p 130-134, 1997.

[23] L. M. Correia and P. O. Frances, “Estimation of Materials Characteristics from Power Measurements at 60 GHz”, *5th IEEE International Symposium, PIMRC'94*, p 510-13 vol.2, 1994.

[24] Siepel home page, retrieved on 10th October, 2009 from http://www.siepel.com/PDFS/83_BROADBAND_PYRAMIDAL_ABSORBER_HYFRAL_APM_-_12.02.08.pdf.

[25] G. Mao, B. Fidan, *“Localization Algorithms and Strategies for Sensor Networks”, Information Science Reference.*

[26] The Mathworks helpdesk, retrieved June 4th, 2010 from http://www.mathworks.de/access/helpdesk/help/toolbox/splines/csaps.html.

Publications

Hongzhao Ray Fang, G. Cao, E. Gharavol, K. Tom, K. Mouthaan, “60 GHz short range planar RSS localization”, *Asia-Pacific Microwave Conference 2010*.

Glossary

AOA	Angle-of-Arrival
CDF	Cumulative Distribution Function
COG	Centre-of-Gravity
FPGA	Field-programmable-gate-array
Gbps	Giga-bits-per-second
GHz	Giga-hertz
HDTV	High-Definition Television
IF	Intermediate Frequency
IWCOG	Iterated Weighted Centre-of-Gravity
kSa/s	Kilosamples-per-second
LAN	Local Area Network
Mbps	Mega-bits-per-second
NLOS	Non-Line-of-Sight
RSS	Received-Signal-Strength
RSSI	Received-Signal-Strength-Indicator
RX	Receiver
SMA	Sub-Miniature version A
SNR	Signal-Noise-Ratio
TDOA	Time-Difference-of-Arrival
TOA	Time-of-Arrival
TX	Transmitter
UWB	Ultra-Wideband
WCOG	Weighted Centre-of-Gravity
Wi-Fi	Wireless Infidelity
Wi-HD	Wireless-High-Definition
WiMax	Worldwide Interoperability for Microwave Access

APPENDIX A RSS of measured and spline versus distance on 20 cm stands (V and dBV)

The RSS spline models used for mapping the distance from the RSS of transmitters 1, 2, 3 and 4 are generated using the measured RSSI values. The generated spline models of transmitters 1, 2, 3 and 4 using the RSSI values (in voltage) measured with 20 cm stands are shown in Figures A.1 to A.4 respectively. The same measurements in dBV are presented in Figures A.5 to A.8. The models generated with the RSSI values measured on Siepel mm-wave absorbers in V and dBV are shown in Figures A.9-12 and A.13-16 respectively. Their corresponding distance errors are also illustrated in the inset of the same figures.

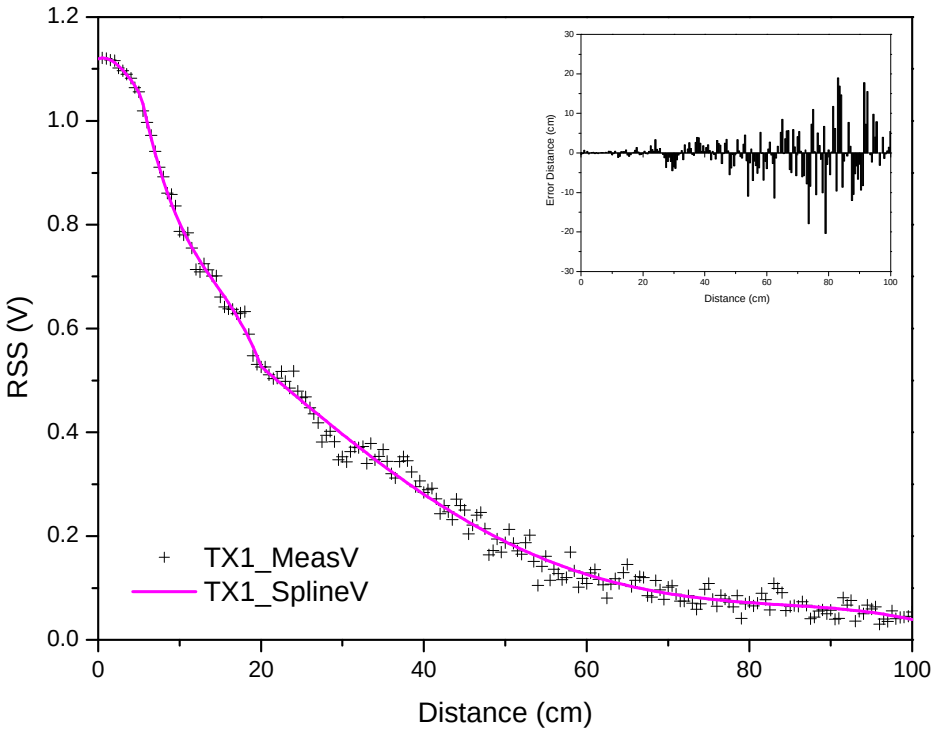

Figure A.1: Measured RSS and spline-fit of TX1 in V on 20 cm stands with inset showing the expected distance error.

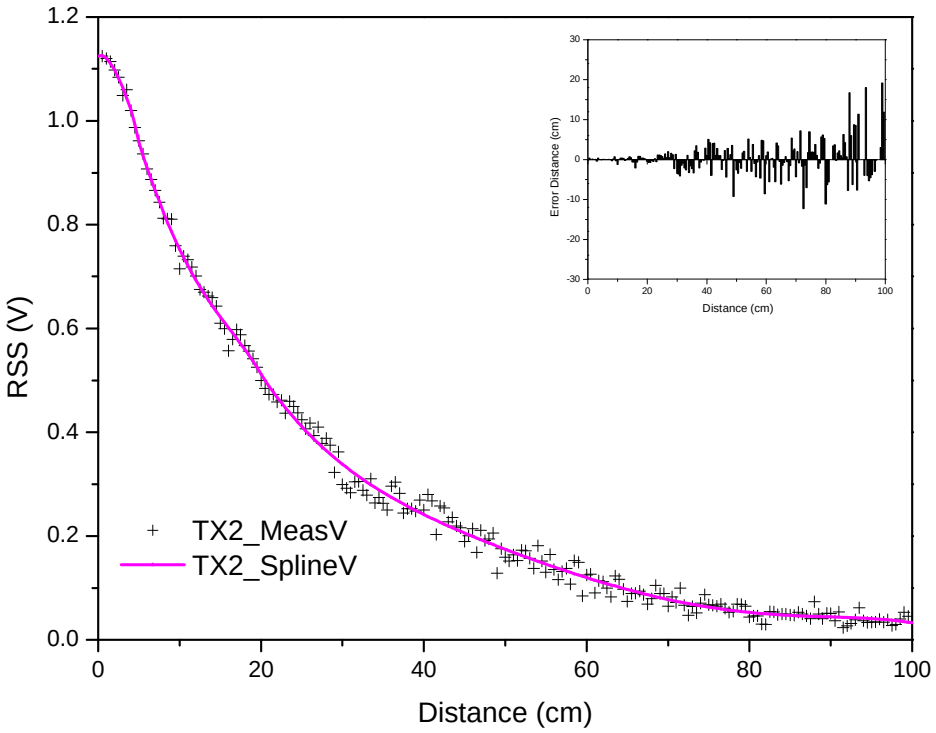

Figure A.2: Measured RSS and spline-fit of TX2 in V on 20 cm stands with inset showing the expected distance error.

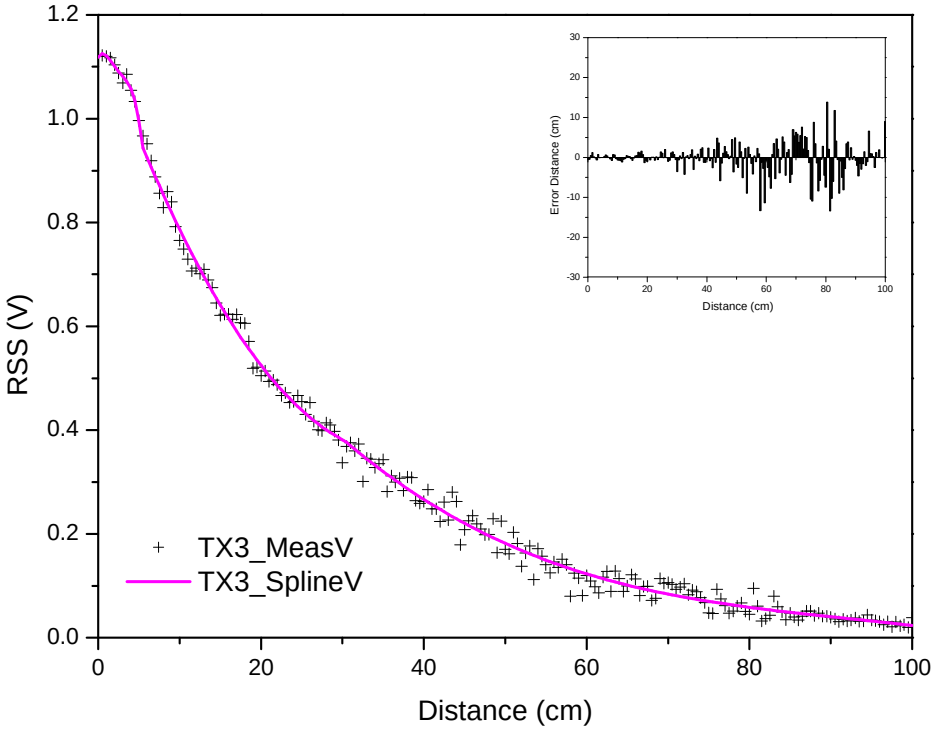

Figure A.3: Measured RSS and spline-fit of TX3 in V on 20 cm stands with inset showing the expected distance error.

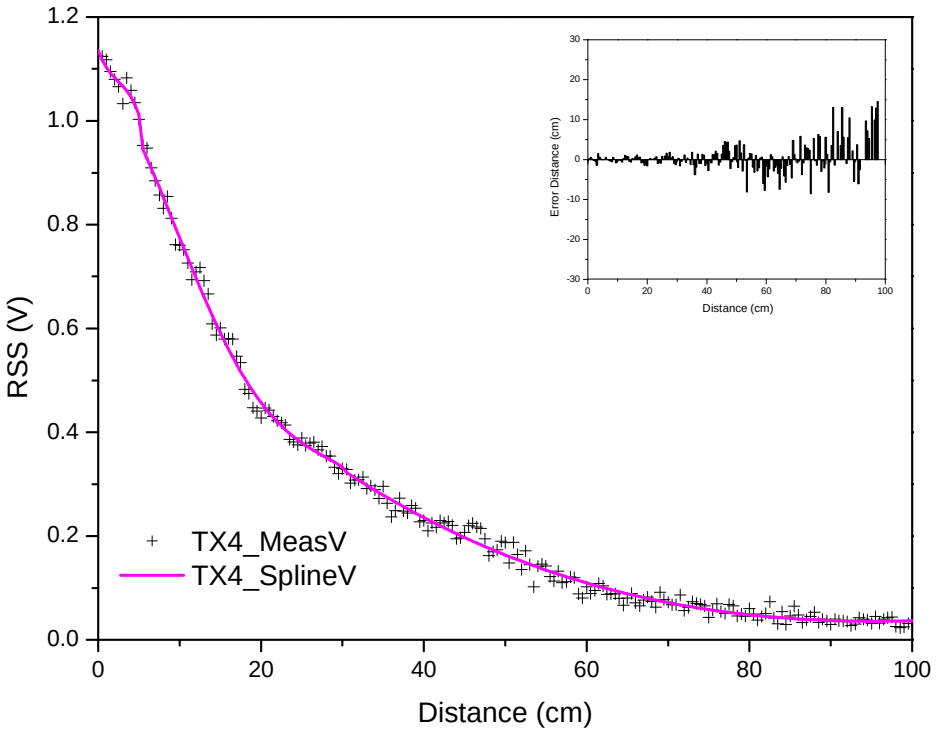

Figure A.4: Measured RSS and spline-fit of TX1 in V on 20 cm stands with inset showing the expected distance error.

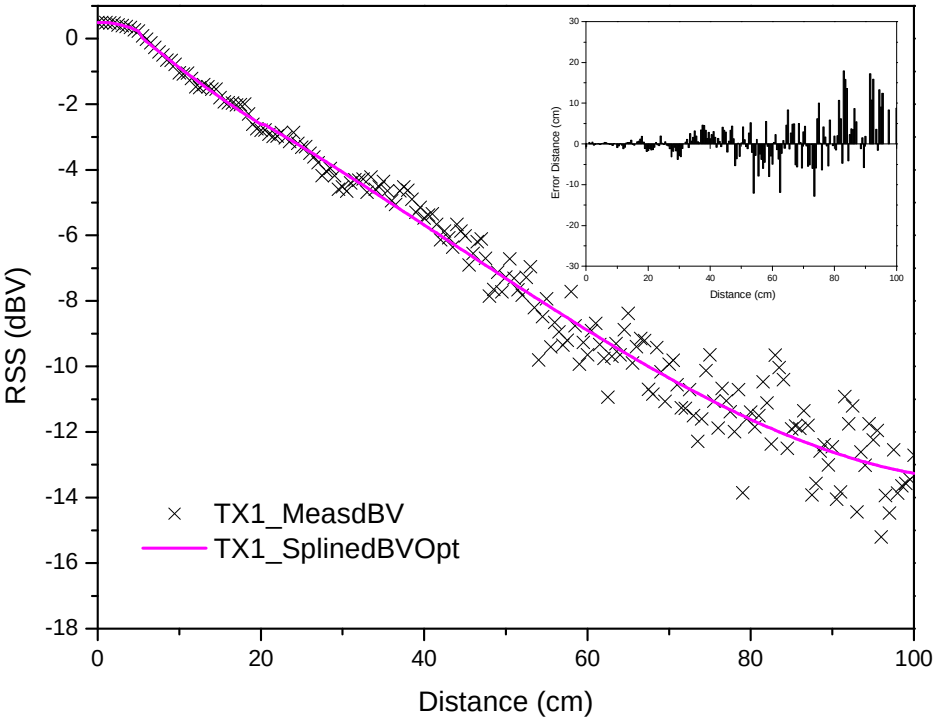

Figure A.5: Measured RSS and spline-fit of TX1 in dBV on 20 cm stands with inset showing the expected distance error.

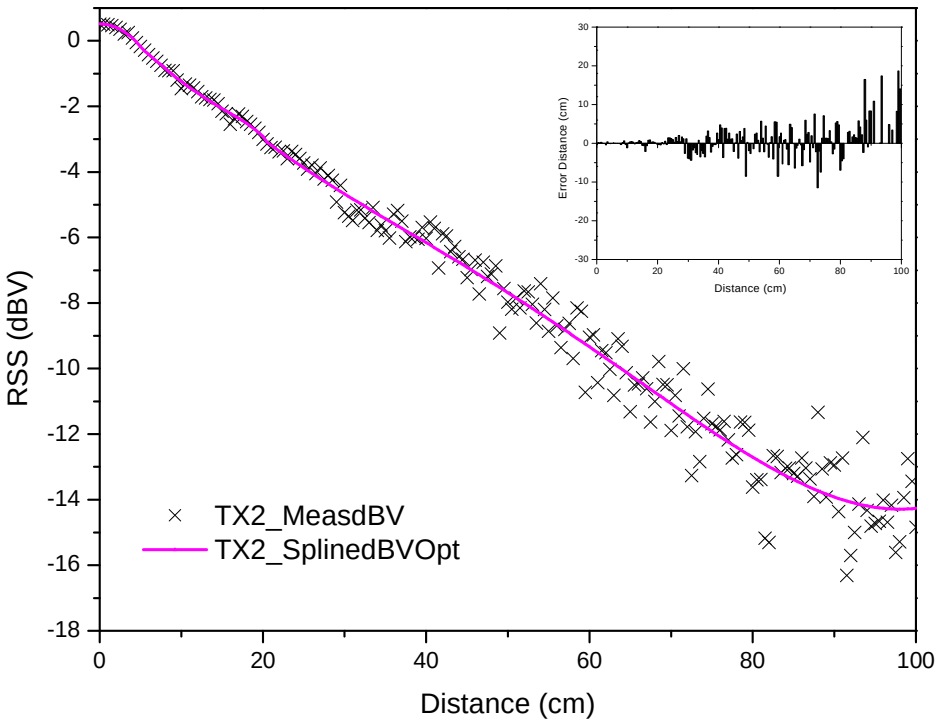

Figure A.6: Measured RSS and spline-fit of TX2 in dBV on 20 cm stands with inset showing the expected distance error.

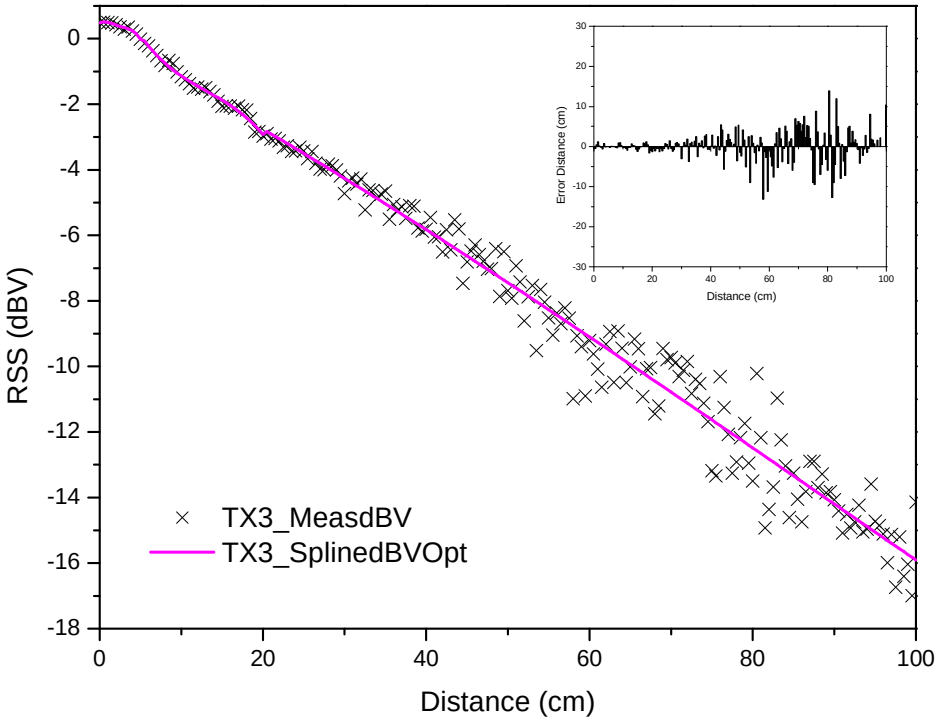

Figure A.7: Measured RSS and spline-fit of TX3 in dBV on 20 cm stands with inset showing the expected distance error.

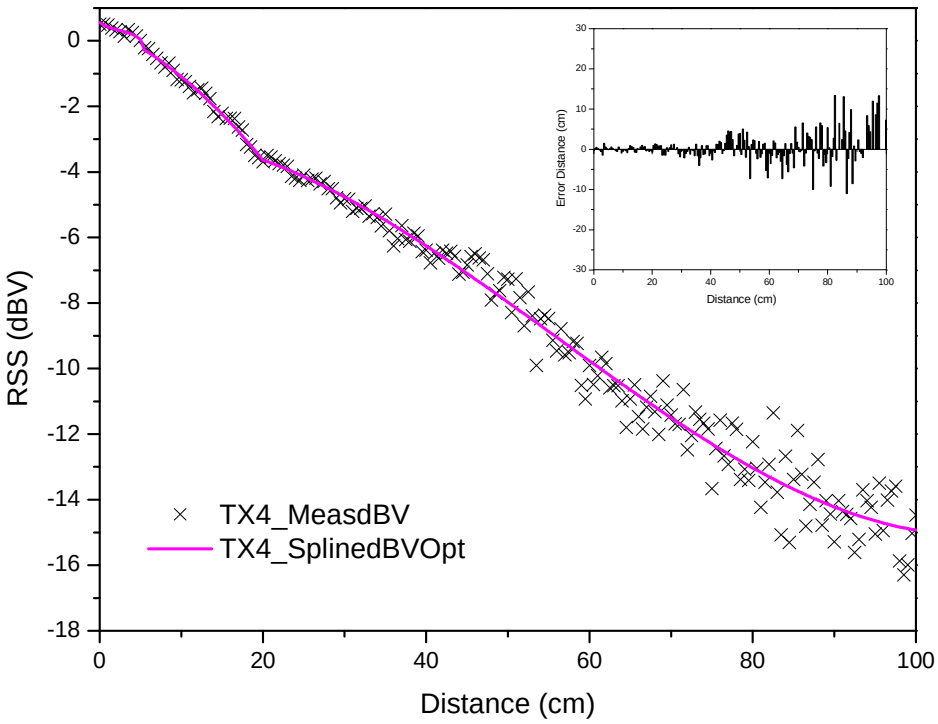

Figure A.8: Measured RSS and spline-fit of TX4 in dBV on 20 cm stands with inset showing the expected distance error.

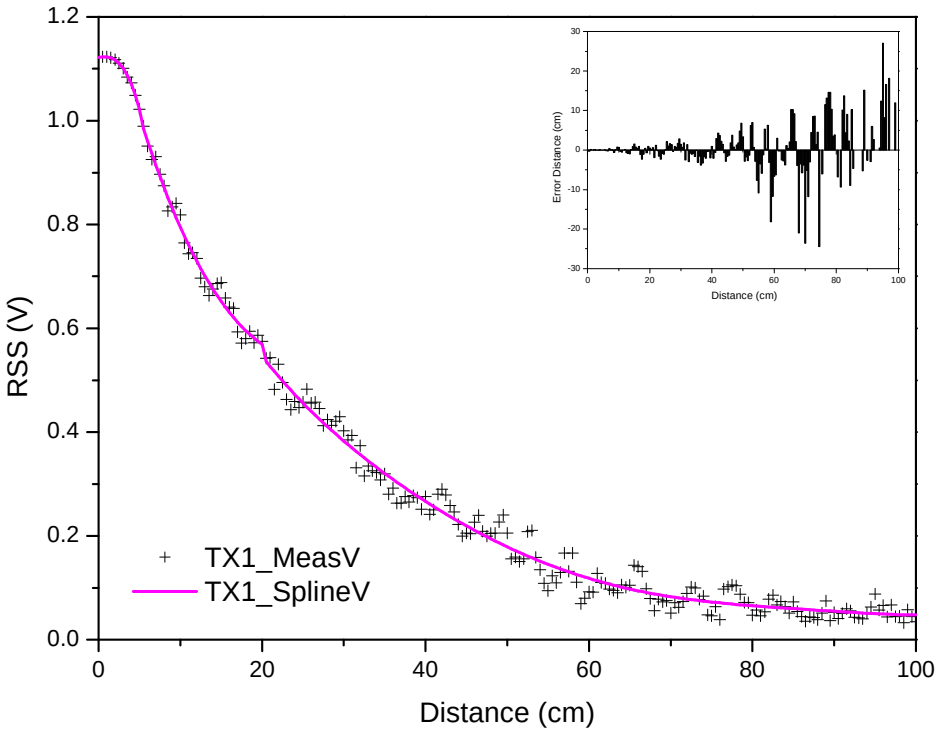

Figure A.9: Measured RSS and spline-fit of TX1 in V on Siepel mm-wave absorbers with inset showing the expected distance error.

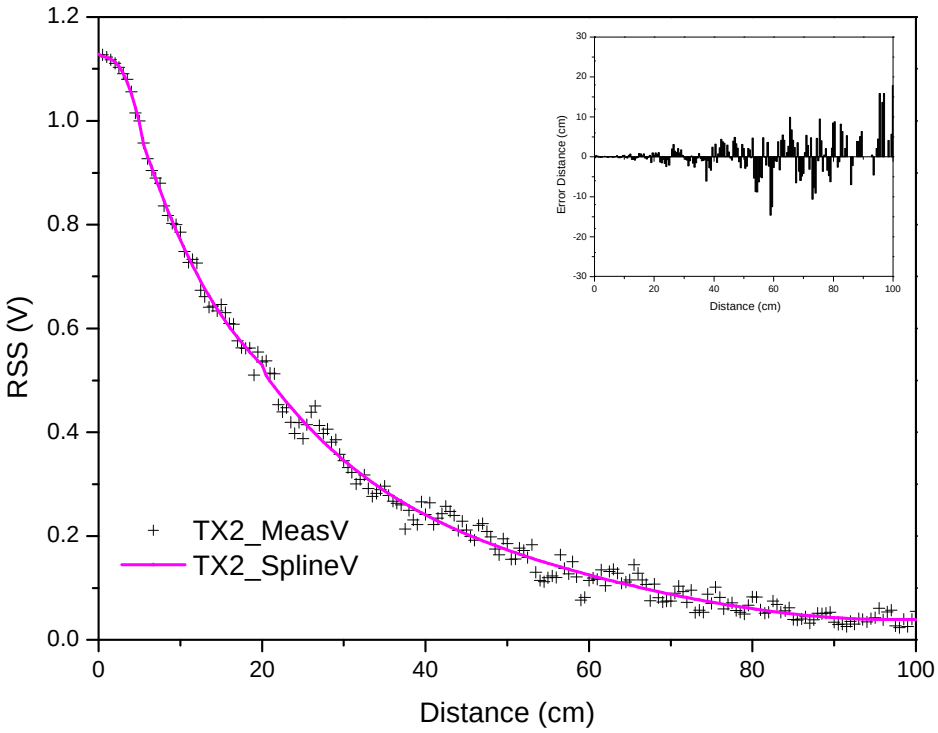

Figure A.10: Measured RSS and spline-fit of TX2 in V on Siepel mm-wave absorbers with inset showing the expected distance error.

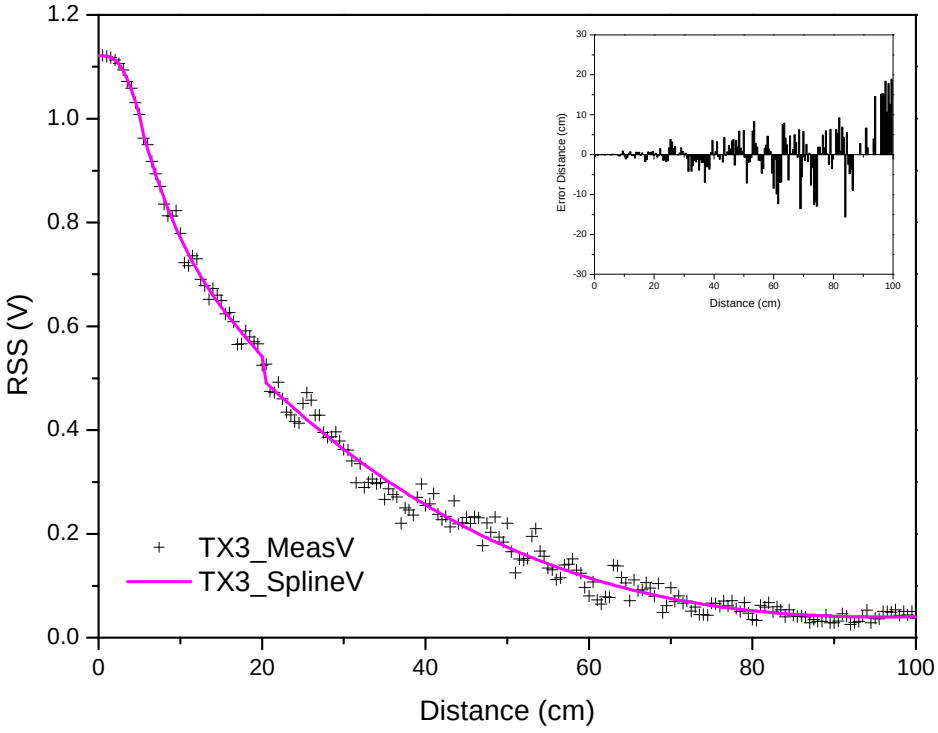

Figure A.11: Measured RSS and spline-fit of TX3 in V on Siepel mm-wave absorbers with inset showing the expected distance error.

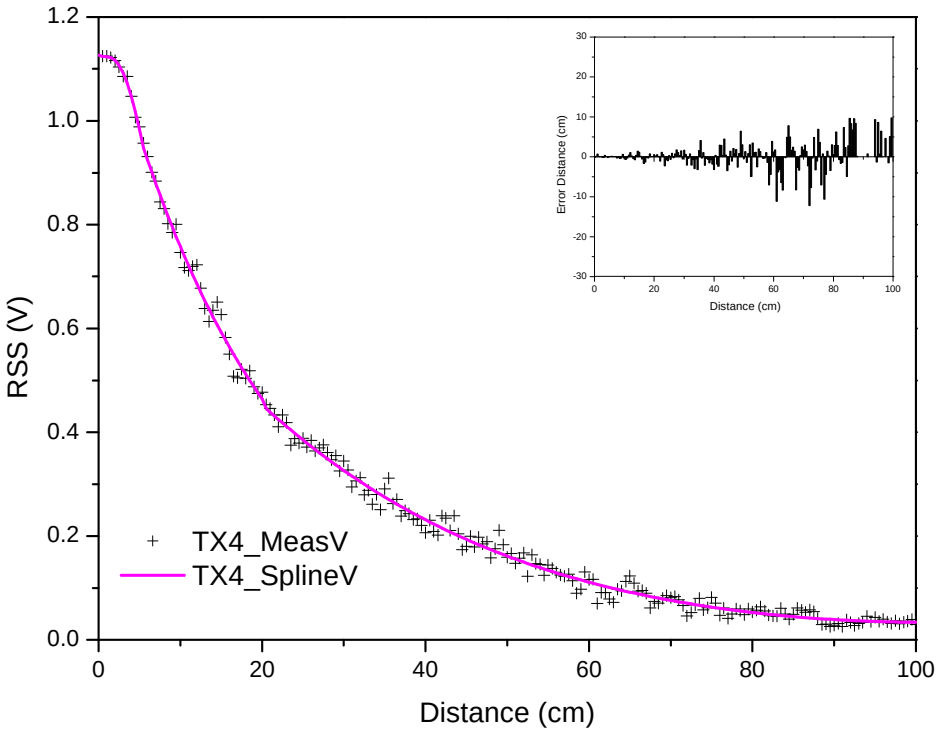

Figure A.12: Measured RSS and spline-fit of TX4 in V on Siepel mm-wave absorbers with inset showing the expected distance error.

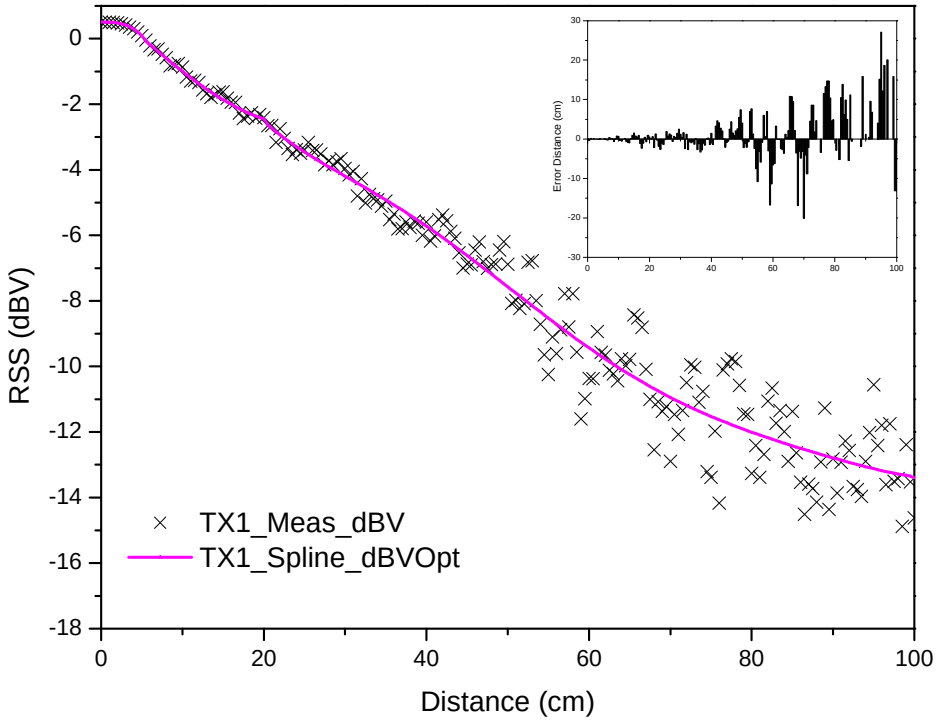

Figure A.13: Measured RSS and spline-fit of TX1 in dBV on Siepel mm-wave absorbers with inset showing the expected distance error.

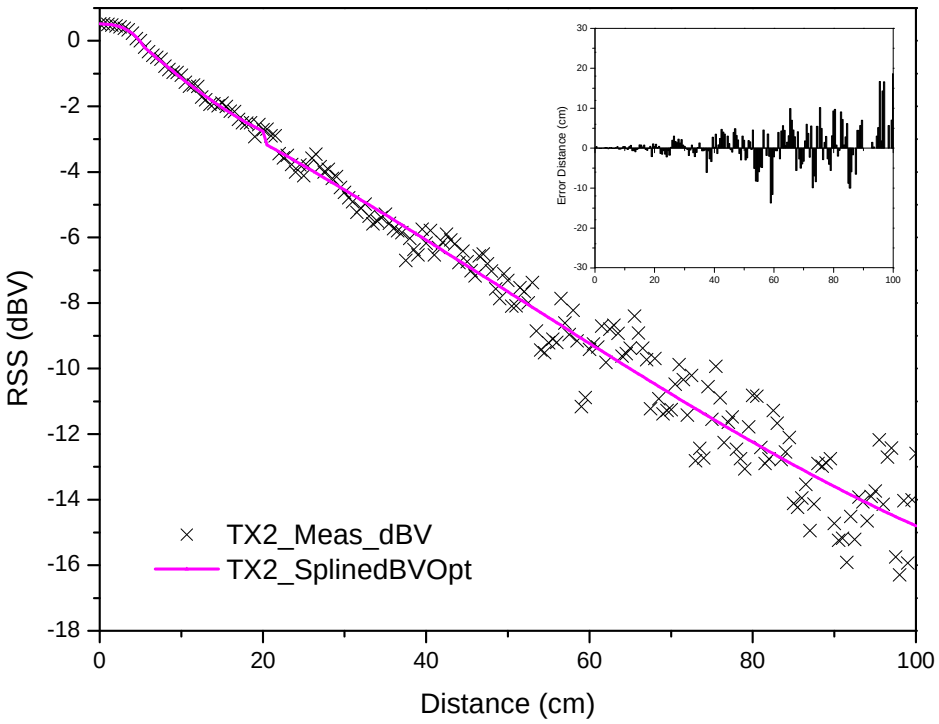

Figure A.14: Measured RSS and spline-fit of TX2 in dBV on Siepel mm-wave absorbers with inset showing the expected distance error.

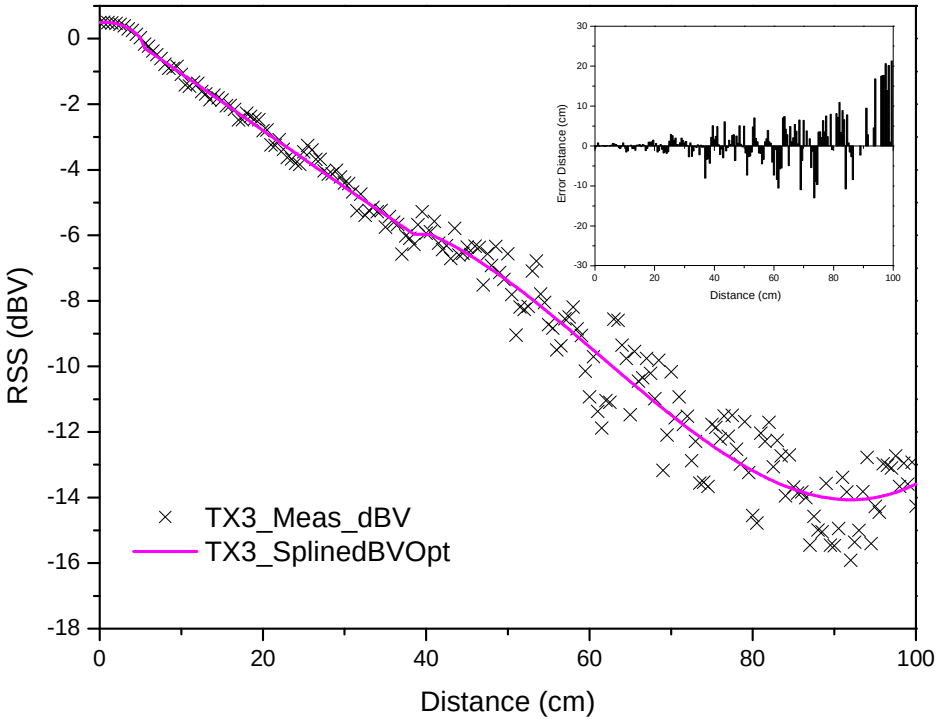

Figure A.15: Measured RSS and spline-fit of TX3 in dBV on Siepel mm-wave absorbers with inset showing the expected distance error.

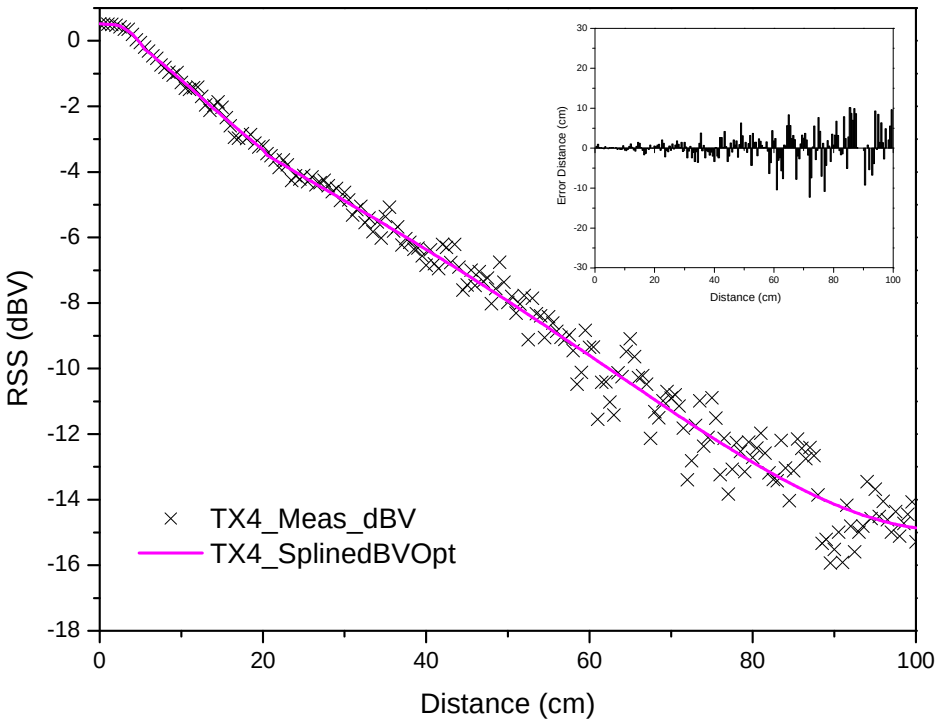

Figure A.16: Measured RSS and spline-fit of TX4 in dBV on Siepel mm-wave absorbers with inset showing the expected distance error.

APPENDIX B Time needed for transmitters to power-up

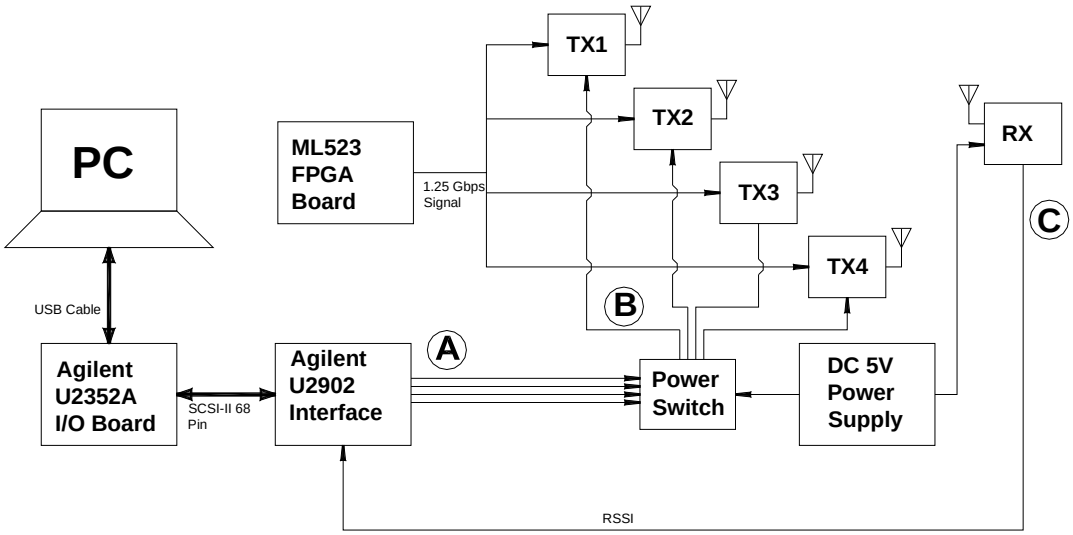

Figure B.1: Test points A, B and C to determine time needed for transmitter to turn on.

This test is performed by connecting the various outputs at test points A, B and C to the analog input of the data acquisition equipment and sending the required enable signal from the PC. The sample rate of the data acquisition equipment is set at 100 kSa/s. This equates to a sample time of 0.01 ms per sample.

The test points perform the following tests: (Note: change the font)

- Test point A: time needed for digital signal to reach power switches.
- Test point B: time delay caused by power switches.
- Test point C: total time needed for transmitters to power-up.

Note that test point C assumes that the time needed for the wave to reach the receiver from the transmitter is negligible.

The measured result at test point A is shown in Figure B.2. It shows that the time needed for the digital signal to reach the power switches is about 0.025 s (0.025 ms).

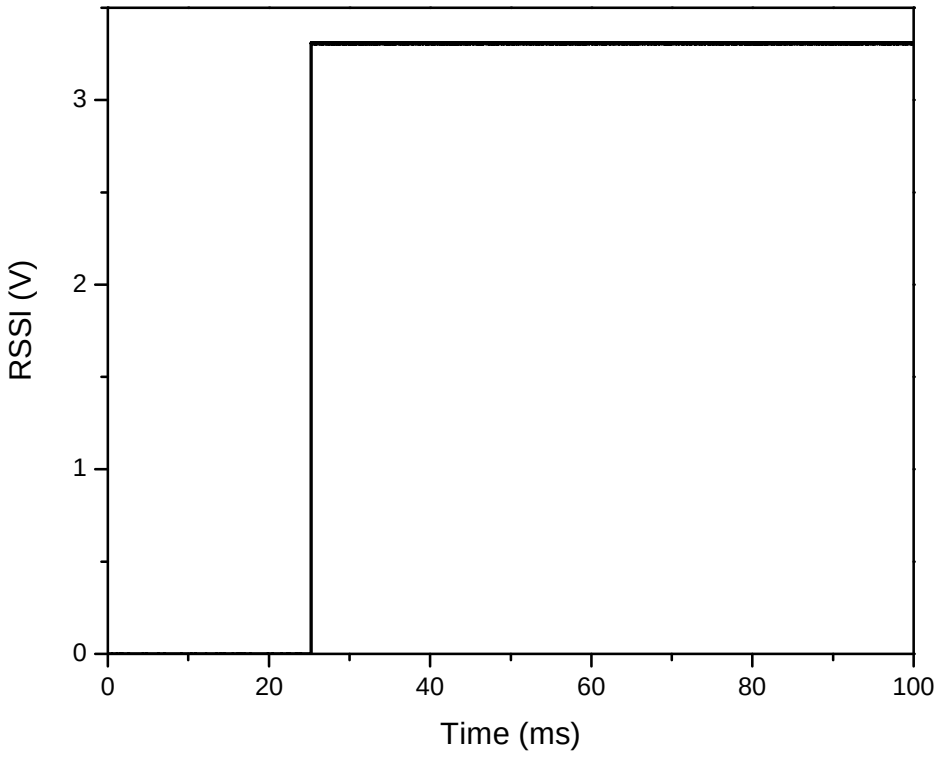

Figure B.2: Time needed for digital signal to reach power switches.

The measured result at test point B is shown in Figure B.3. It shows that the total time needed for the 5 V supply to reach the transmitters is 0.03 s (30 ms). After subtracting the delay caused by the digital output, the resultant 0.005 s (5 ms) is the delay caused by the power switch.

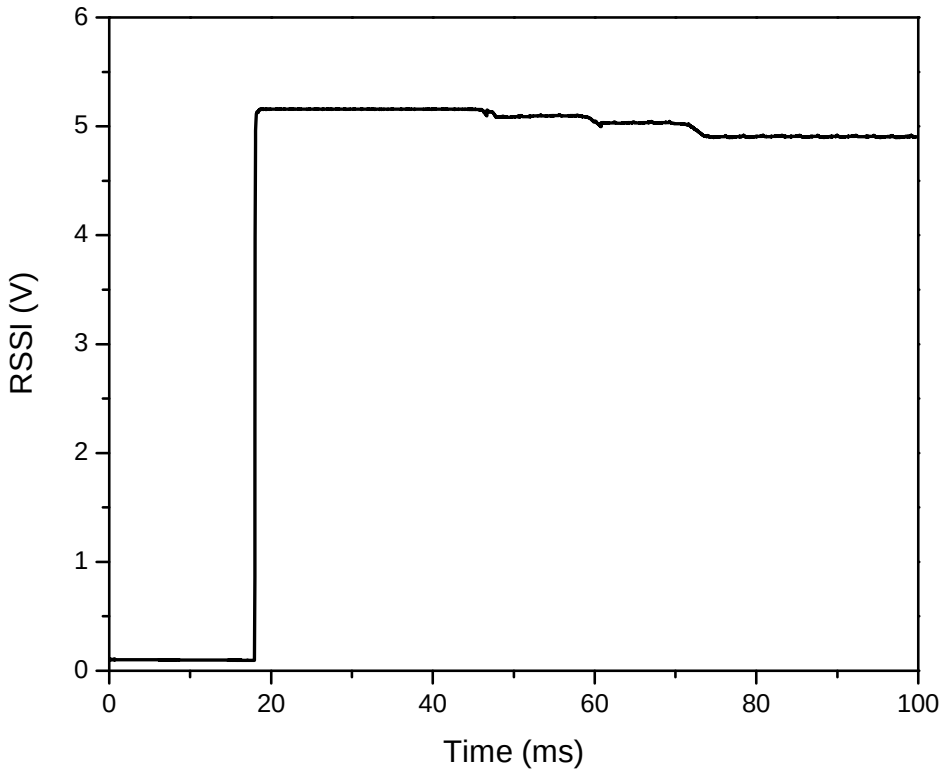

Figure B.3: Total time needed for 5 V supply to reach transmitters.

Figures B.4-7 shows the total time needed for transmitters 1, 2, 3 and 4 to turn on respectively. While TX2 and TX4 require less than 0.1 s (100 ms) to turn on, TX1 and TX3 require about 0.12 s (120 ms). Hence, a conservative estimated delay to impose before extracting the RSSI readings is taken to be 0.15 s (150 ms).

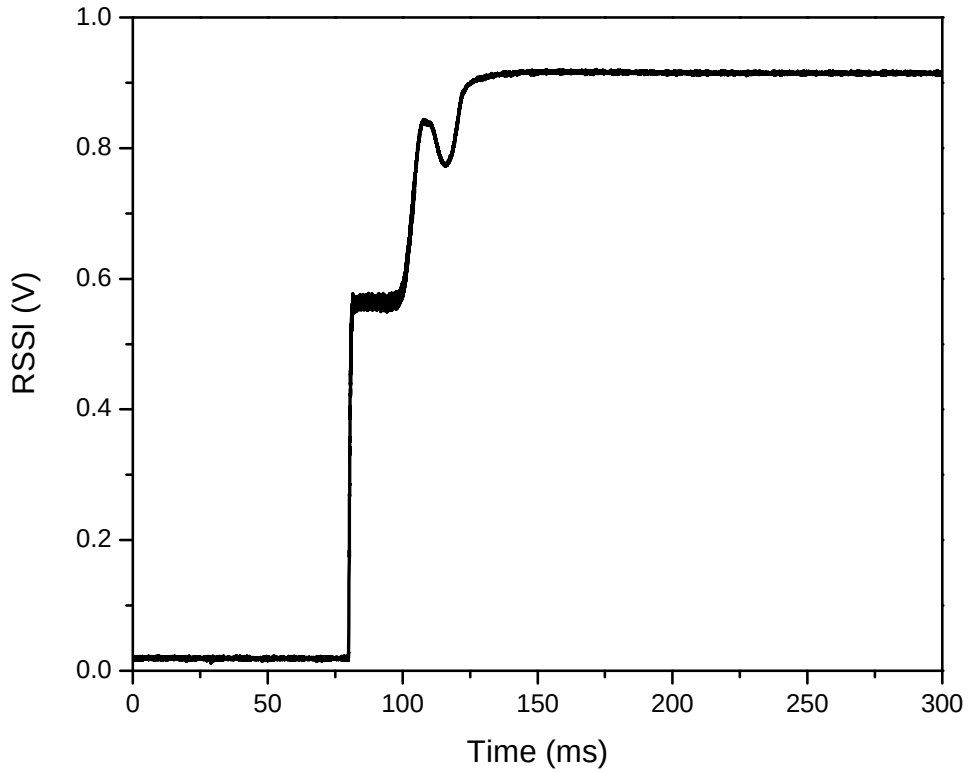

Figure B.4: Total time needed to power-up TX1.

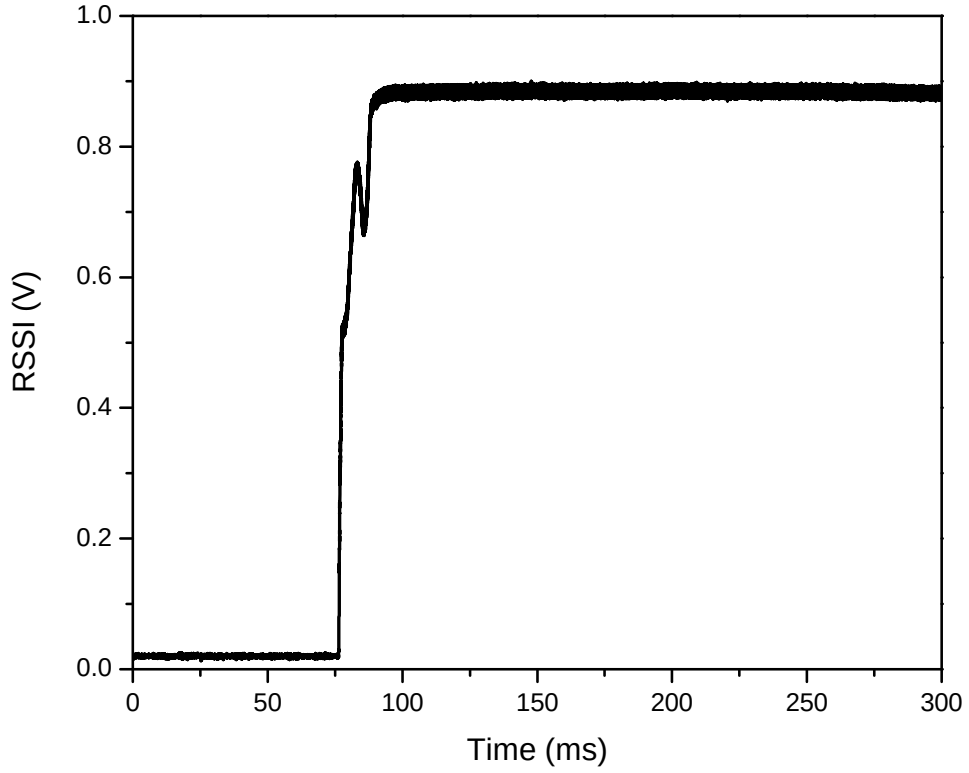

Figure B.5: Total time needed to power-up TX2.

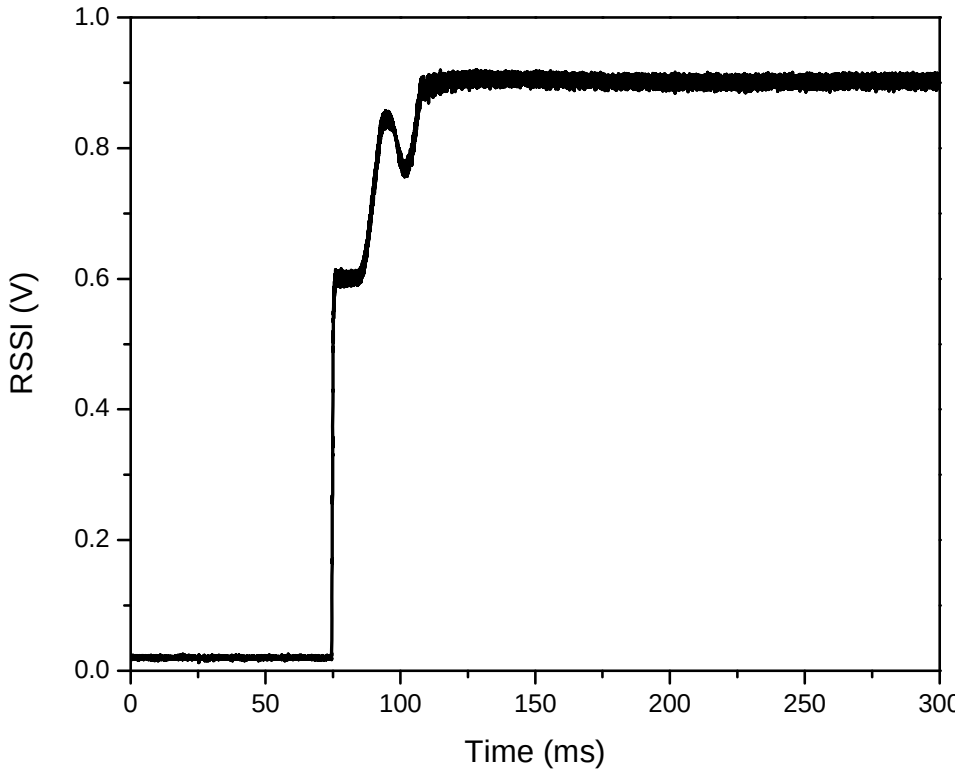

Figure B.6: Total time needed to power-up TX3.

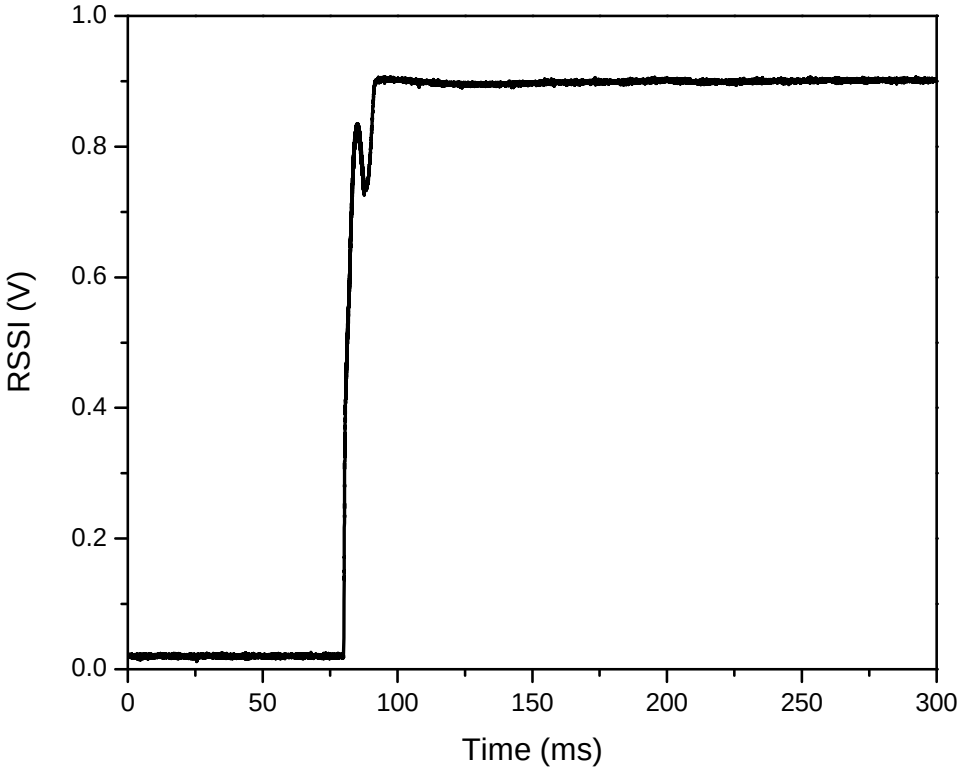

Figure B.7: Total time needed to power-up TX4.

APPENDIX C RSS surface plots belonging to the four transmitters mounted with AT6010H horn antennas at 45°, interpolated with a resolution of 0.5 cm from 437 measured points on a 5 cm grid

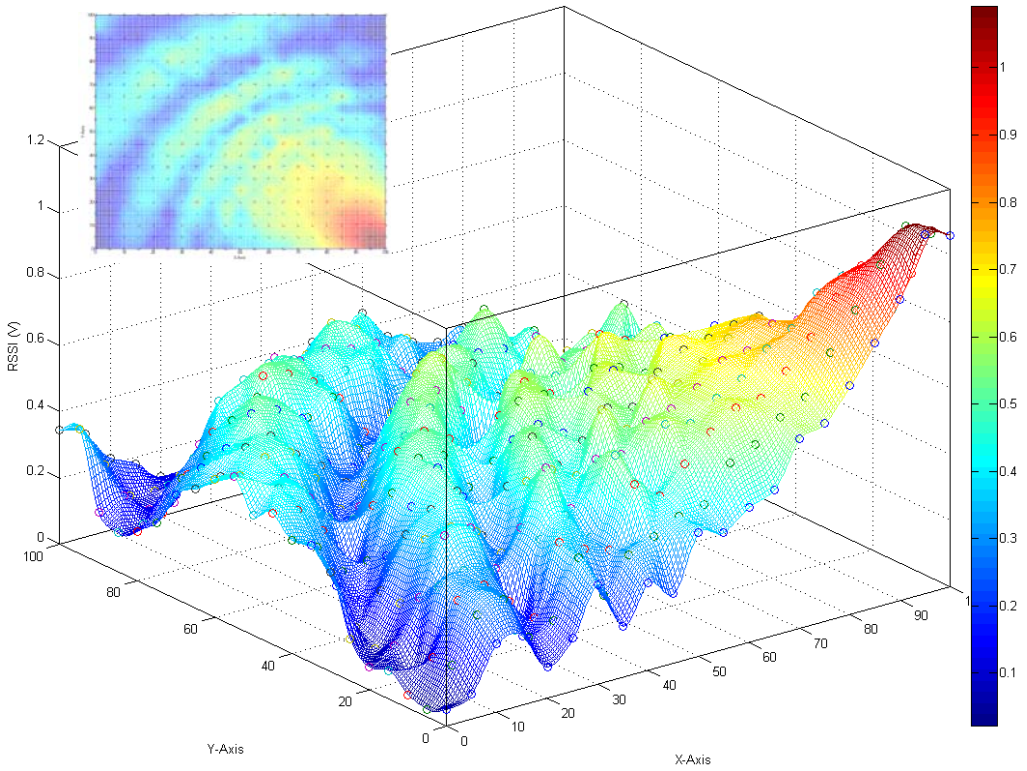

Figure C.1: Interpolated surface plot of TX1's measured RSS at an angle of 45° in V. Inset shows top view.

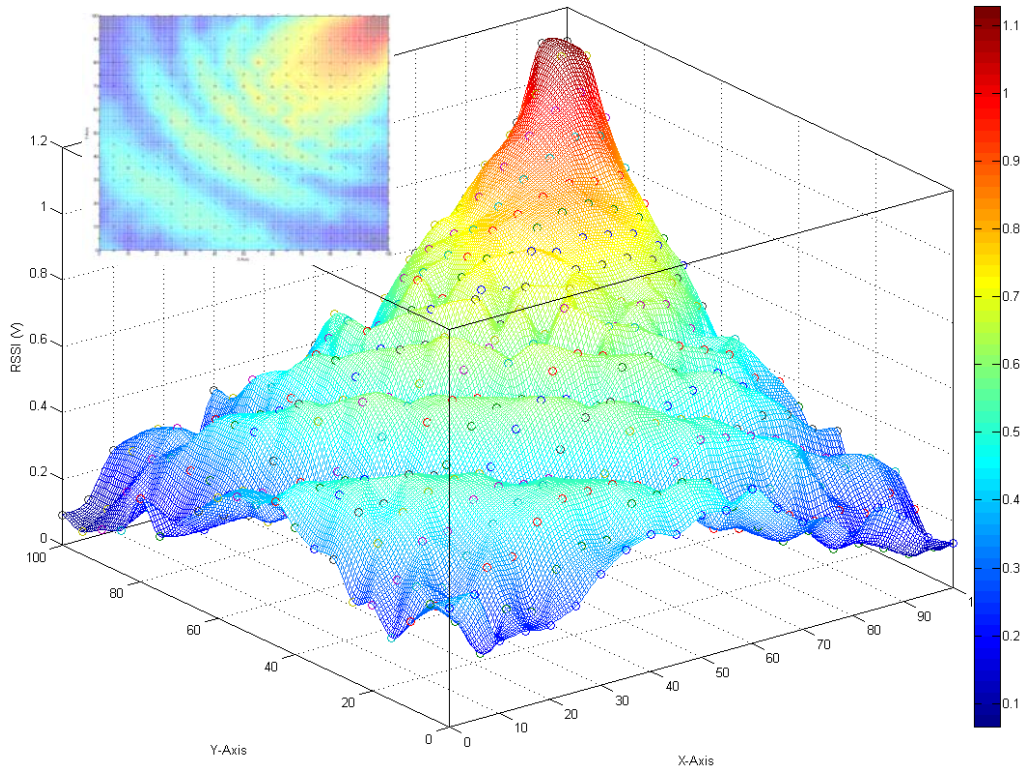

Figure C.2: Interpolated surface plot of TX2's measured RSS at an angle of 45° in V. Inset shows top view.

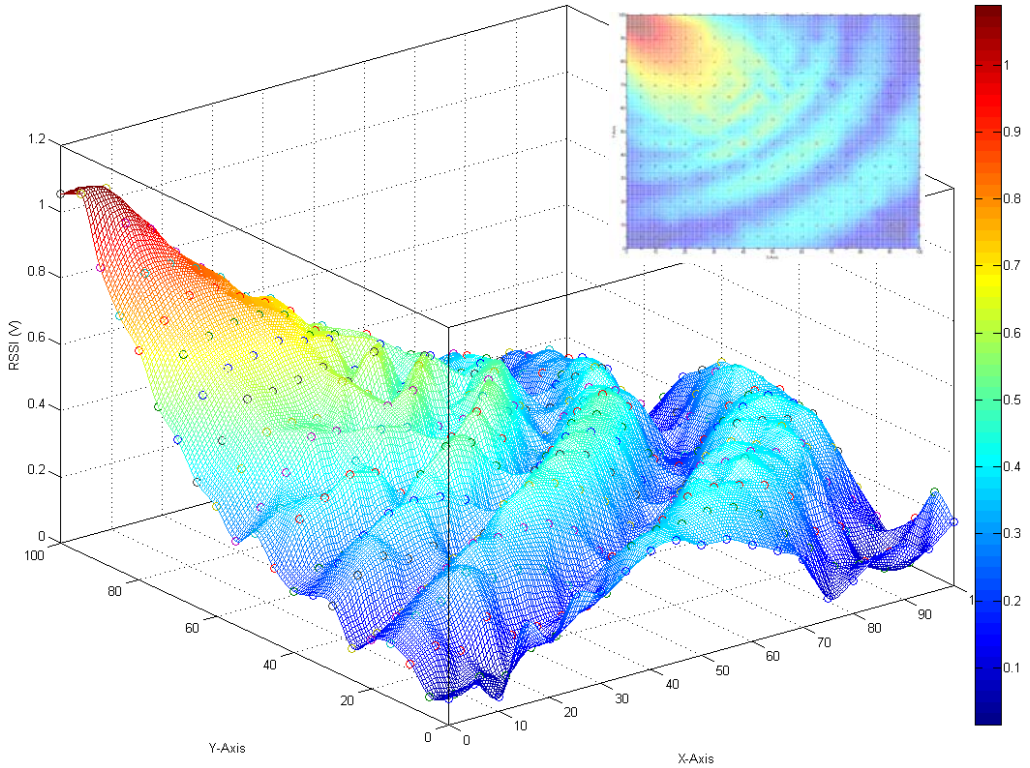

Figure C.3: Interpolated surface plot of TX3's measured RSS at an angle of 45° in V. Inset shows top view.

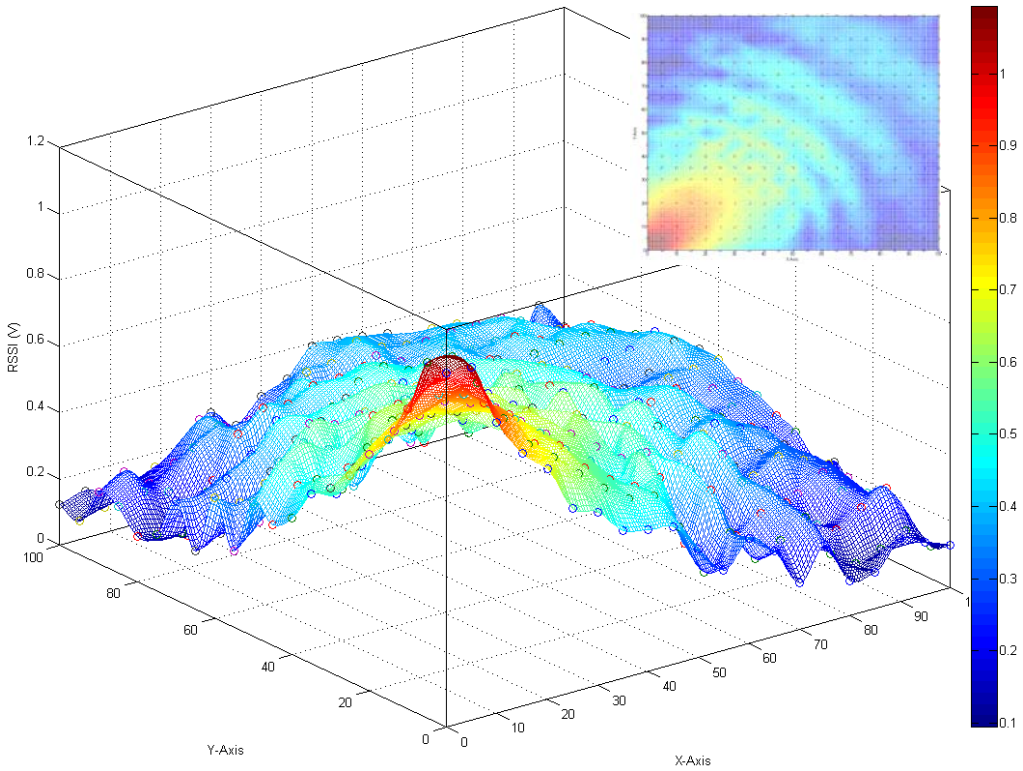

Figure C.4: Interpolated surface plot of TX4's measured RSS at an angle of 45° in V. Inset shows top view.

APPENDIX D Measured RSS surface plots of the four transmitters mounted with AT6010H horn antennas measured on a 5 cm grid

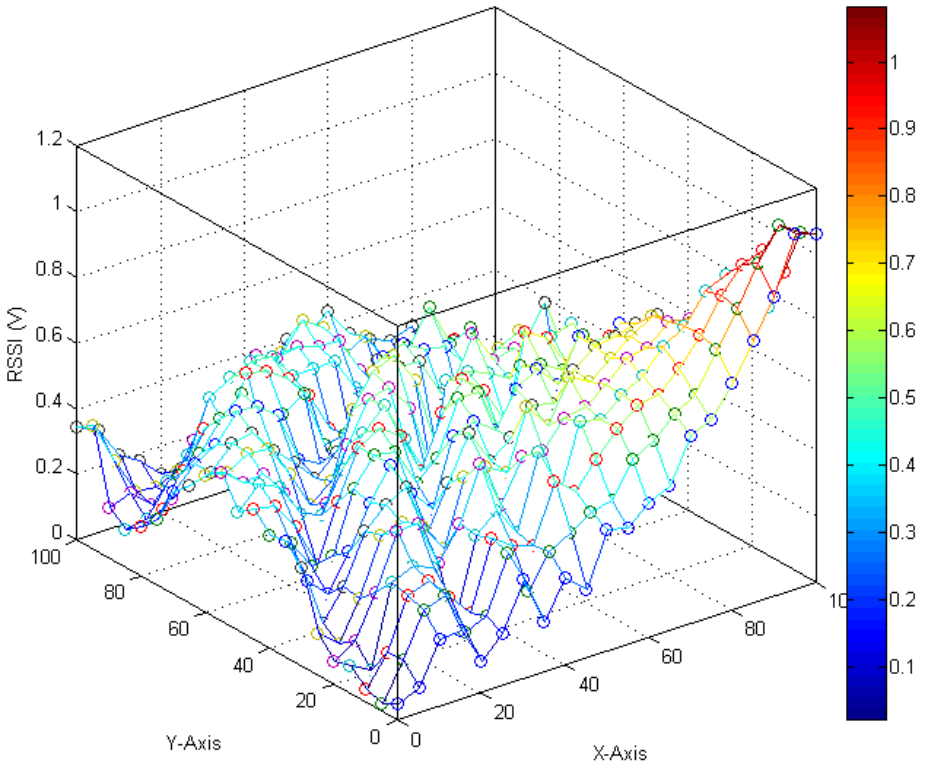

Figure D.1: Surface plot of TX1's measured RSS at an angle of 45° in V.

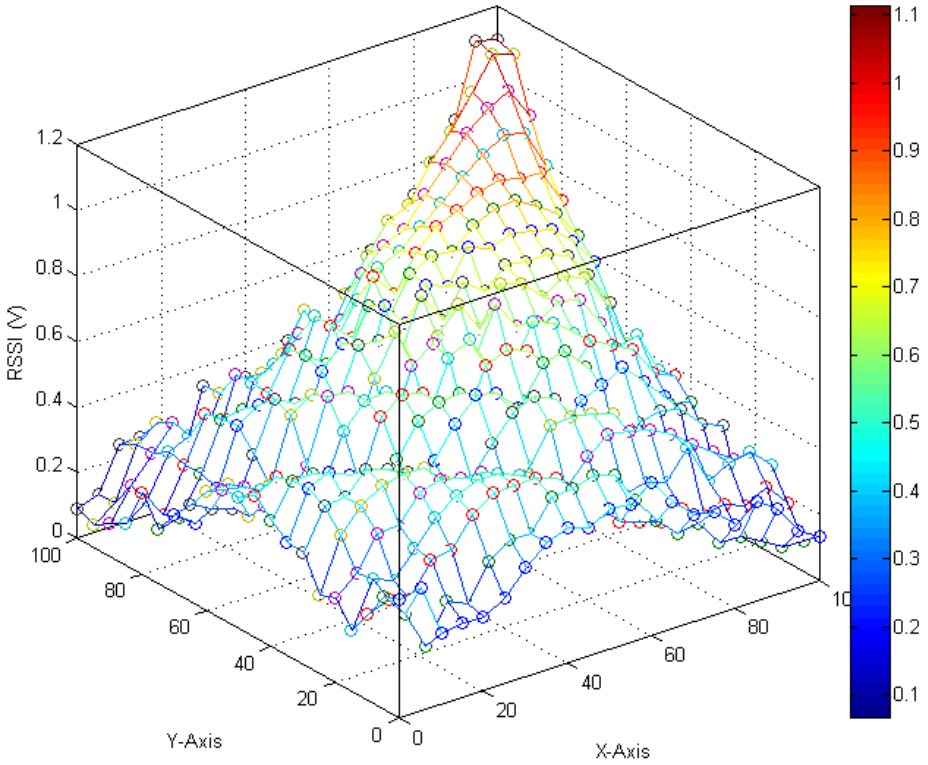

Figure D.2: Surface plot of TX2's measured RSS at an angle of 45° in V.

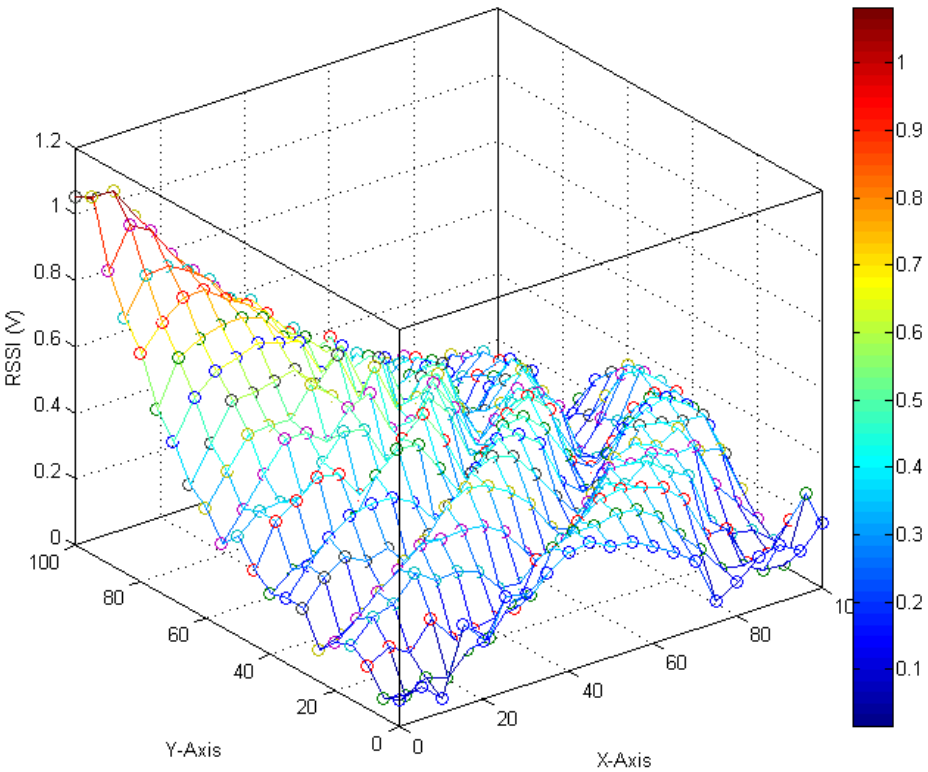

Figure D.3: Surface plot of TX3's measured RSS at an angle of 45° in V.

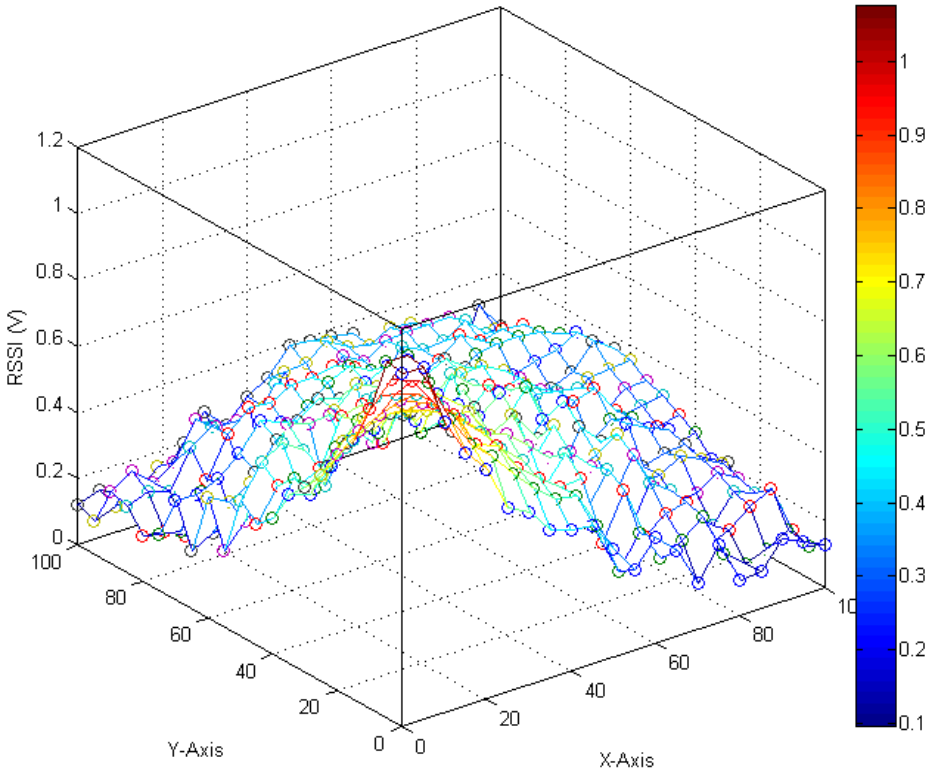

Figure D.4: Surface plot of TX4's measured RSS at an angle of 45° in V.

APPENDIX E Surface plots of measured RSS and spline-fit of the four transmitters mounted with AT6010H horn antennas at 27° (in V)

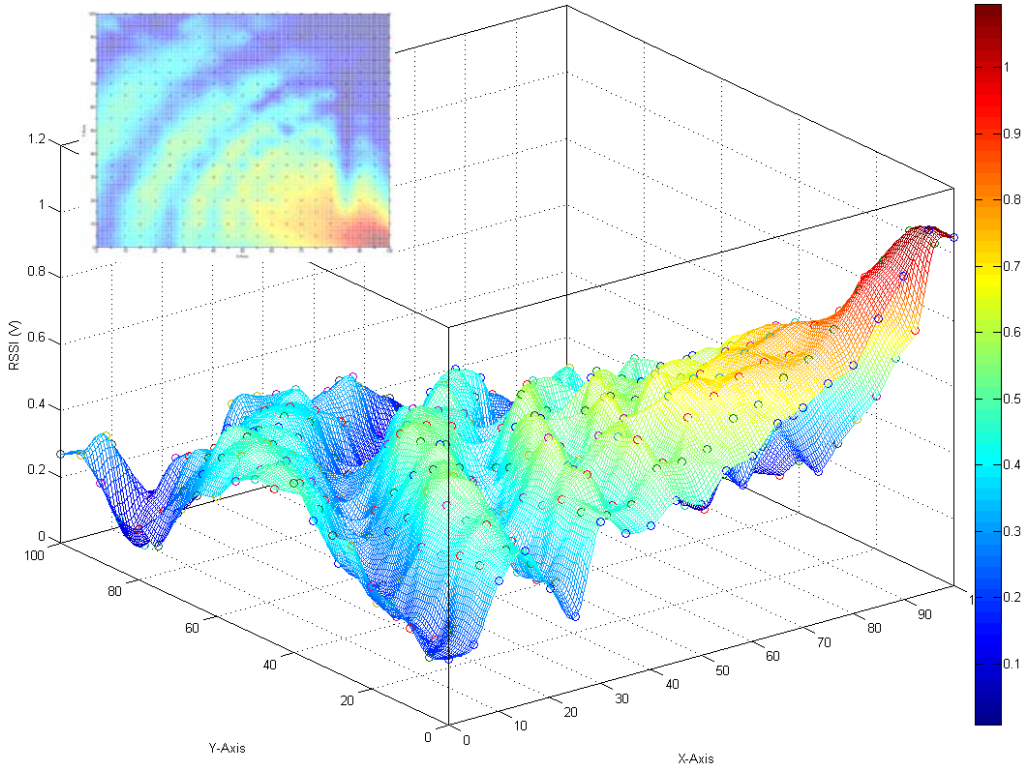

Figure E.1: Surface plot of TX1's measured RSS at an angle of 27° in V. Inset shows top view.

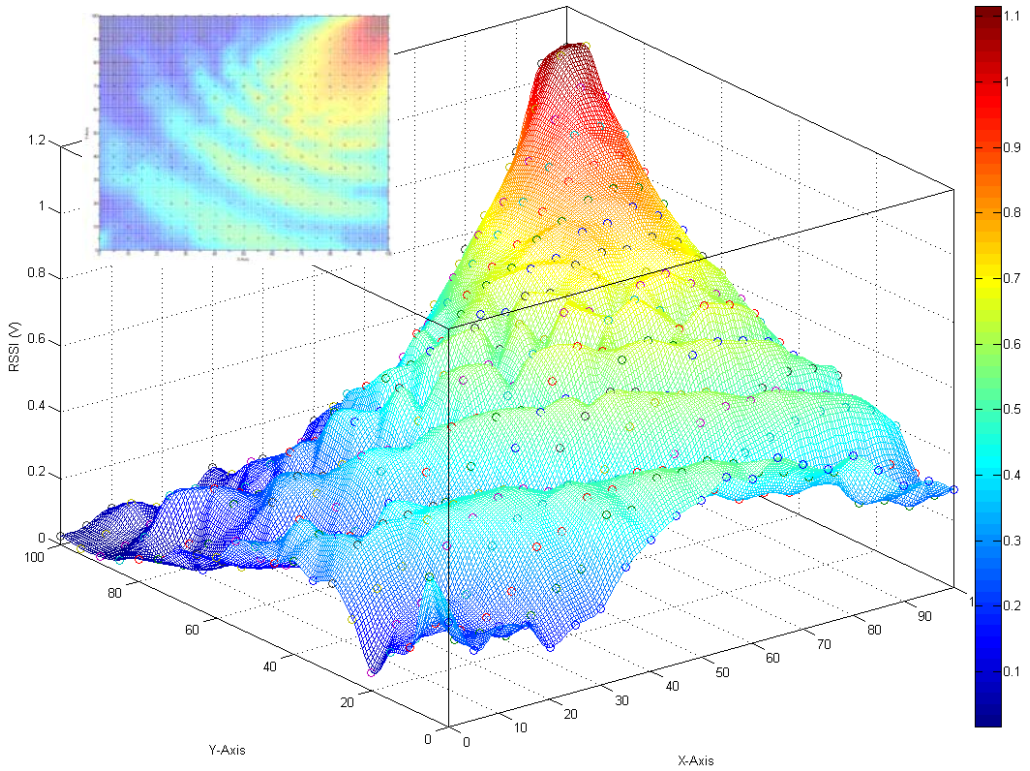

Figure E.2: Surface plot of TX2's measured RSS at an angle of 27° in V. Inset shows top view.

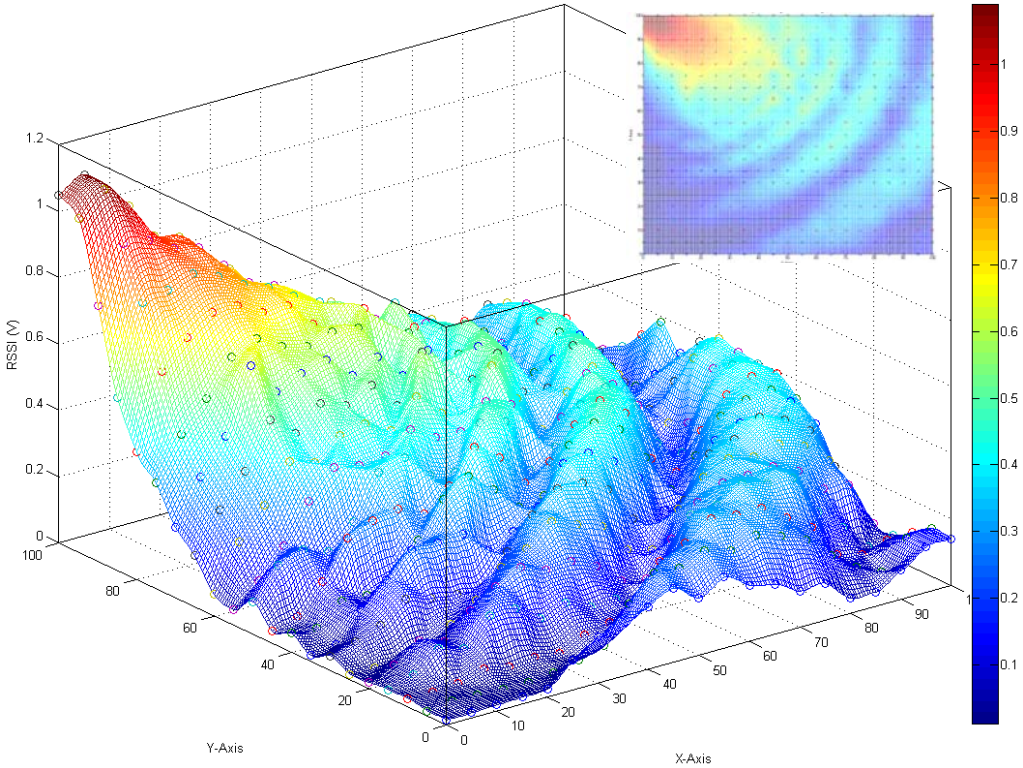

Figure E.3: Surface plot of TX3's measured RSS at an angle of 27° in V. Inset shows top view.

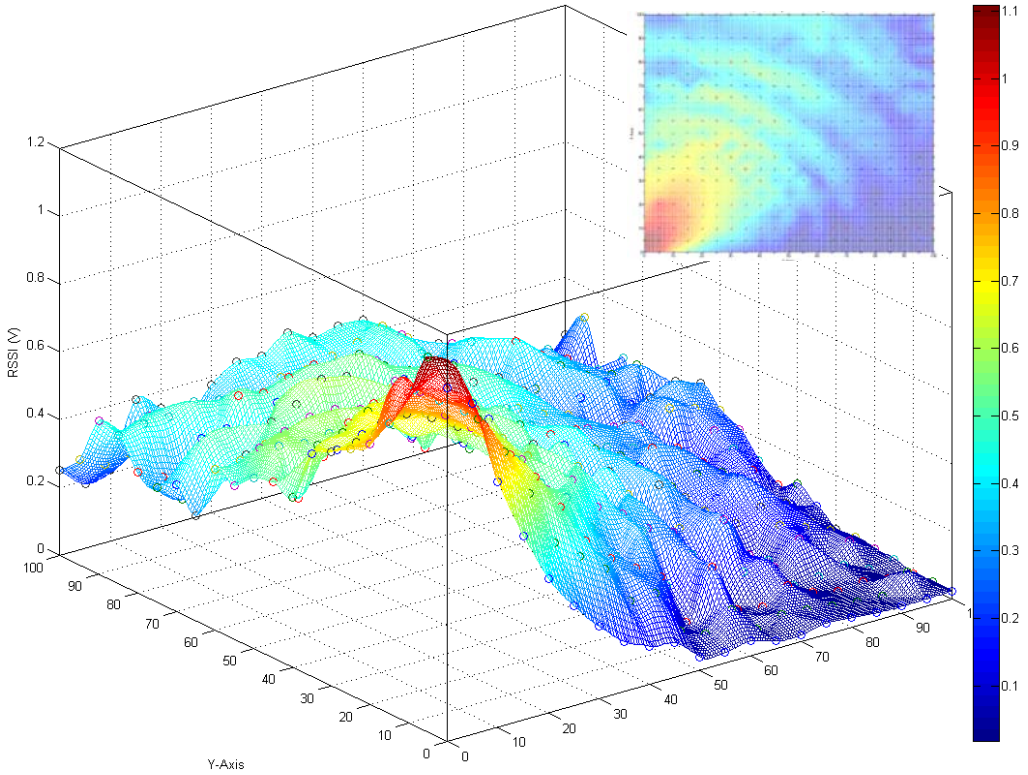

Figure E.4: Surface plot of TX4's measured RSS at an angle of 27° in V. Inset shows top view.

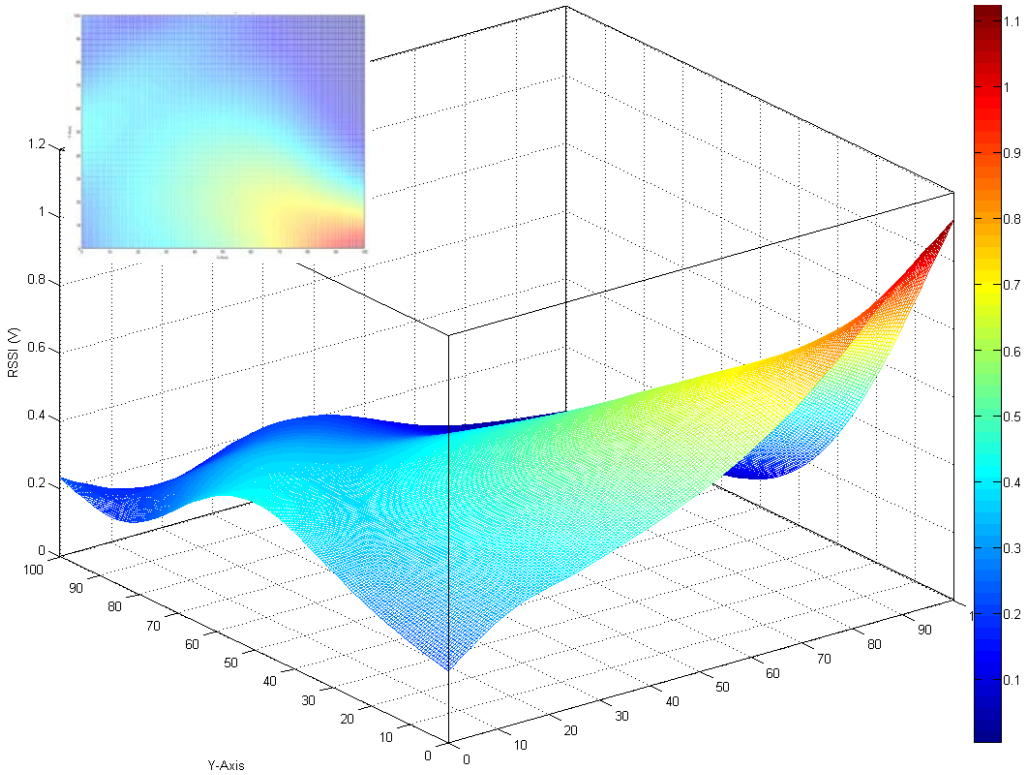

Figure E.5: Spline-fit of TX1's measured RSS at an angle of 27° in V. Inset shows top view.

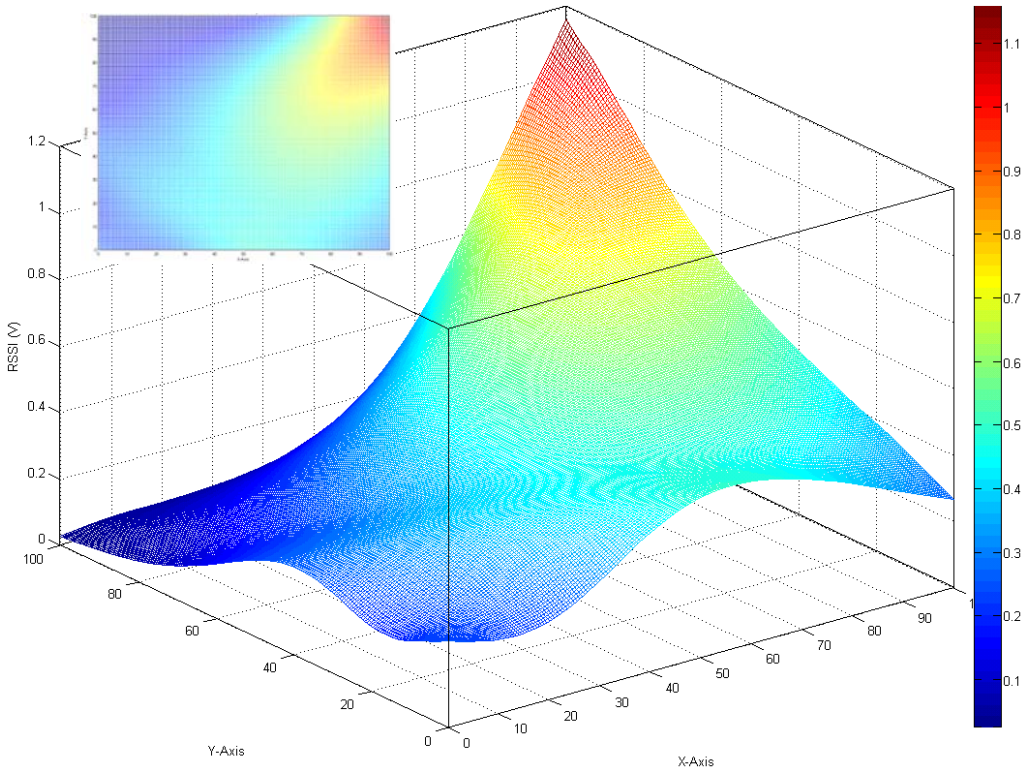

Figure E.6: Spline-fit of TX2's measured RSS at an angle of 27° in V. Inset shows top view.

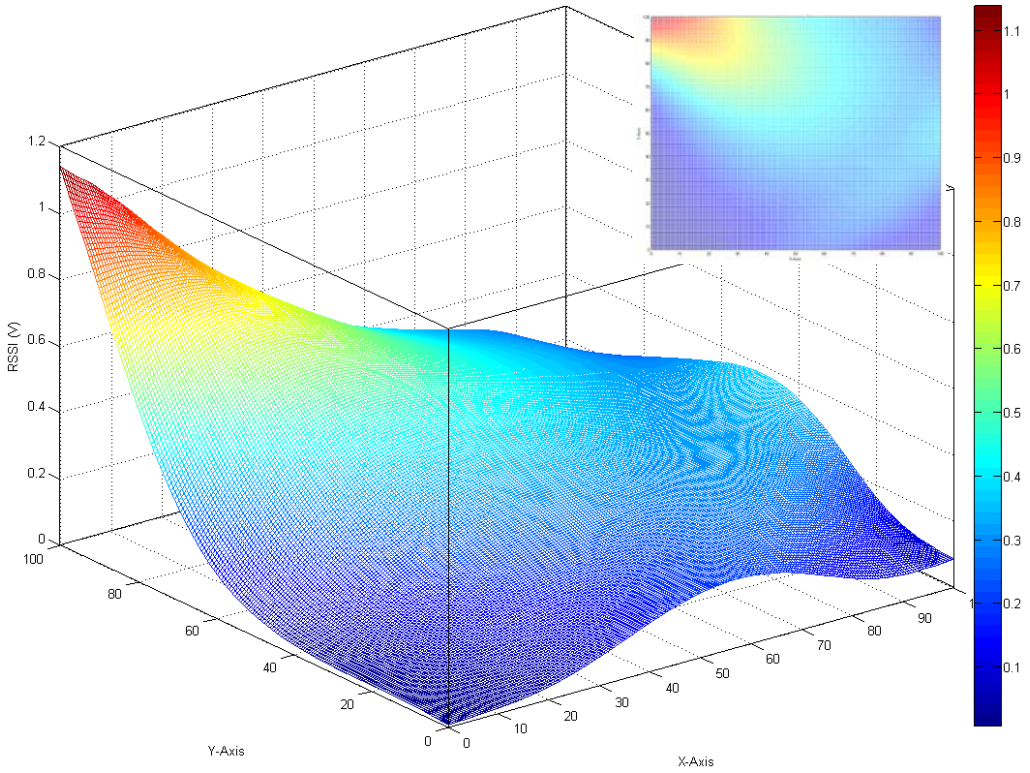

Figure E.7: Spline-fit of TX3's measured RSS at an angle of 27° in V. Inset shows top view.

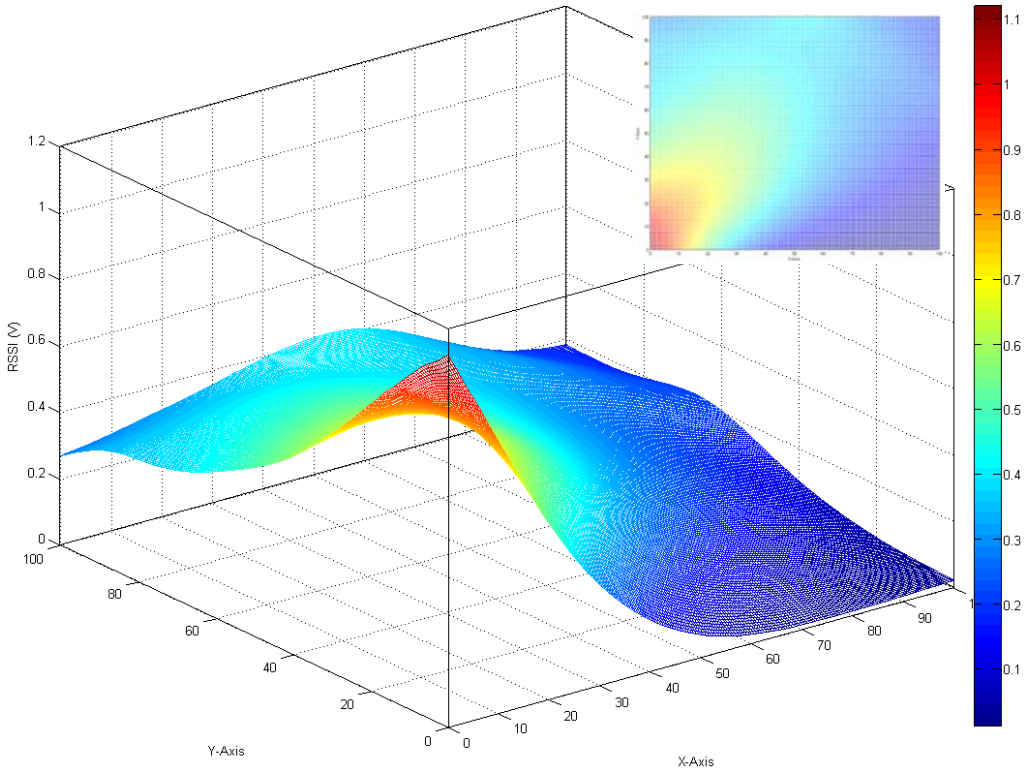

Figure E.8: Spline-fit of TX4's measured RSS at an angle of 27° in V. Inset shows top view.

APPENDIX F Surface plots of measured RSS and spline-fit of the four transmitters mounted with AT6010H horn antennas at 27° (in dBV)

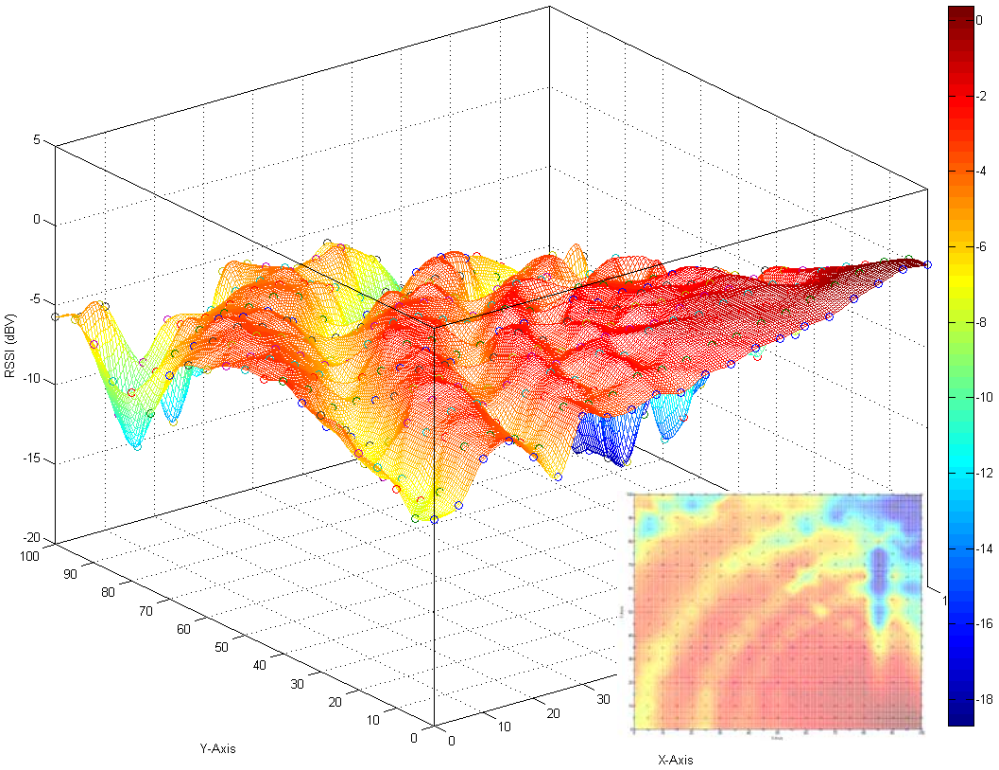

Figure F.1: Surface plot of TX1's measured RSS at an angle of 27° in dBV. Inset shows top view.

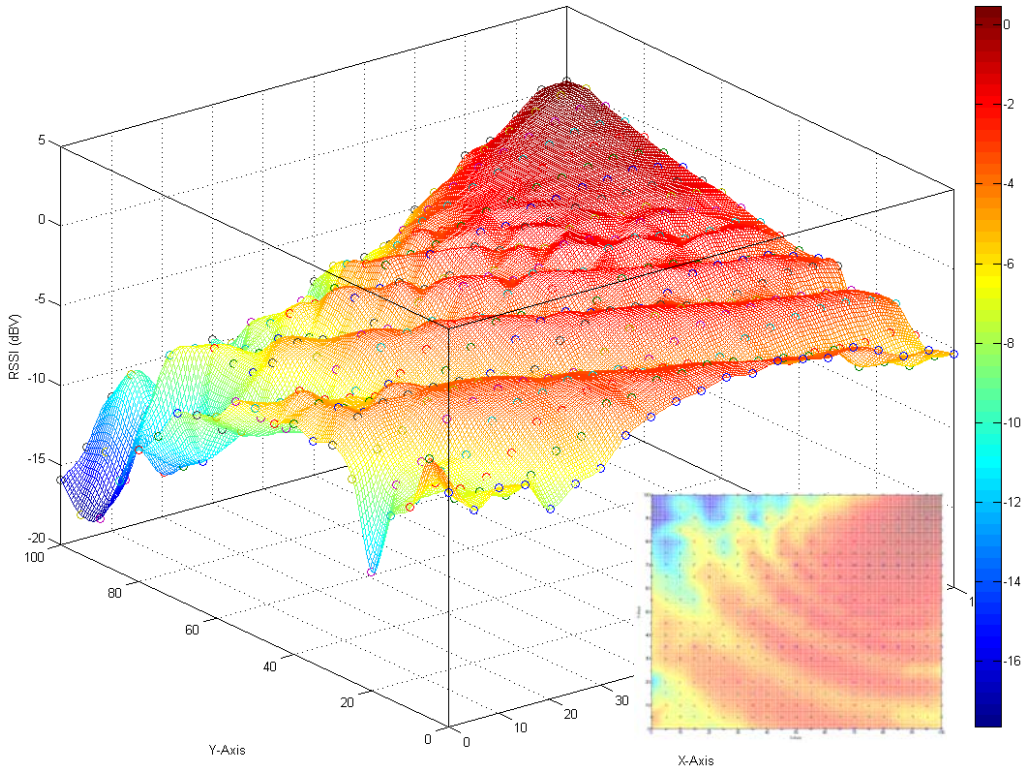

Figure F.2: Surface plot of TX2's measured RSS at an angle of 27° in dBV. Inset shows top view.

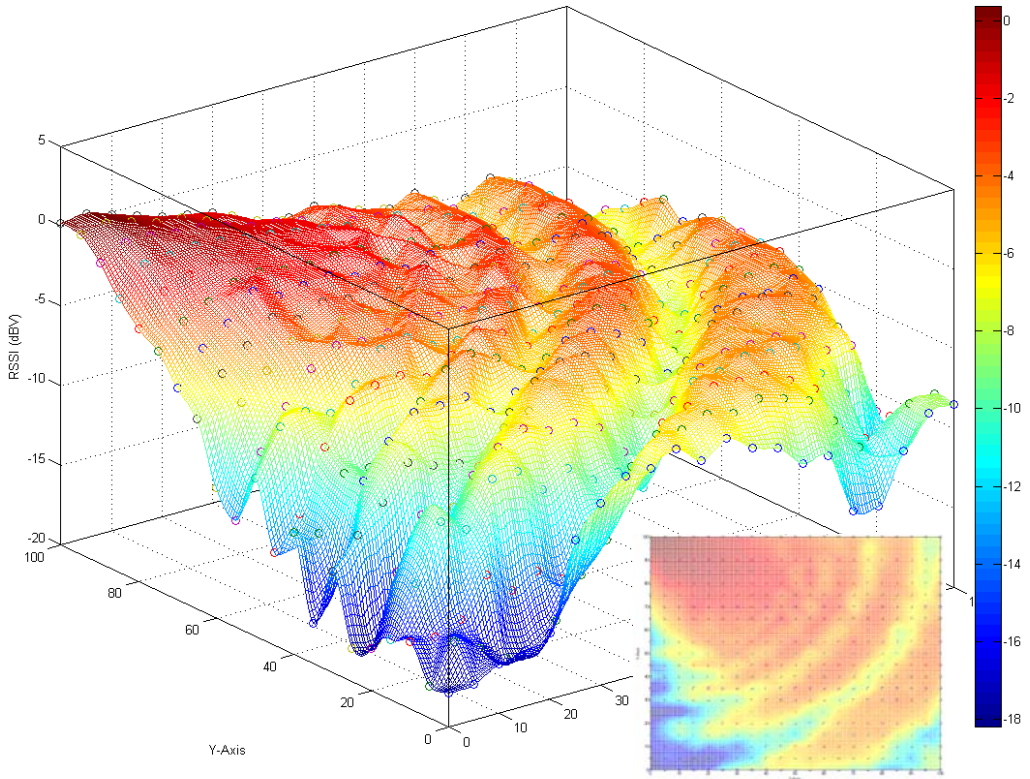

Figure F.3: Surface plot of TX3's measured RSS at an angle of 27° in dBV. Inset shows top view.

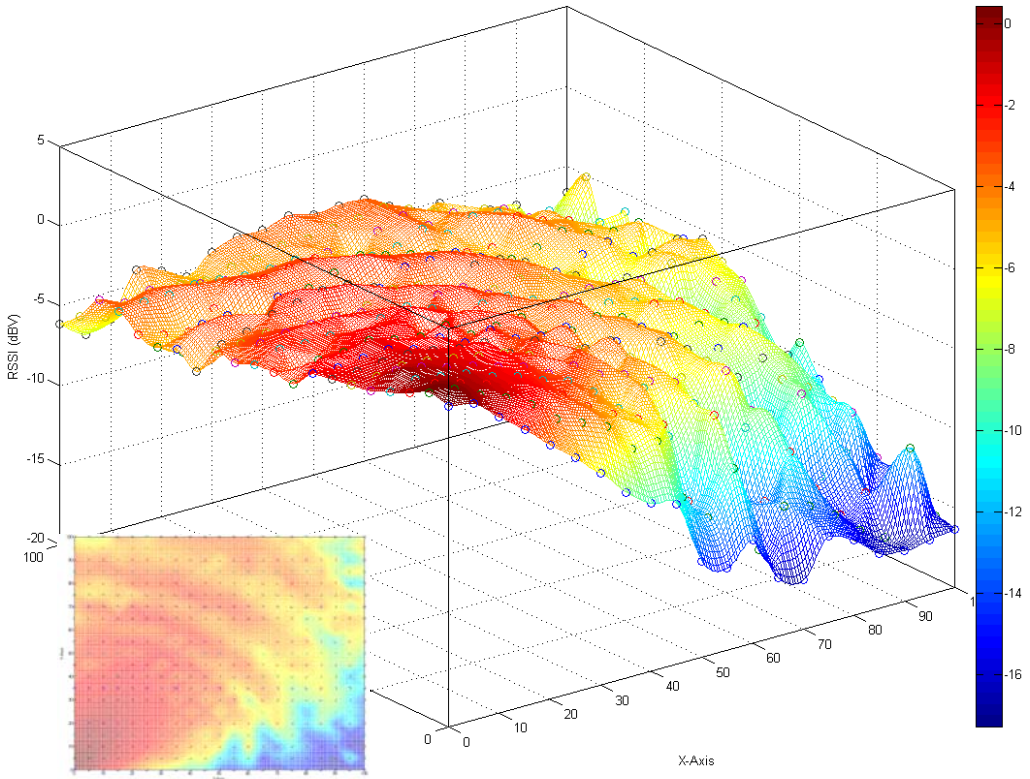

Figure F.4: Surface plot of TX4's measured RSS at an angle of 27° in dBV. Inset shows top view.

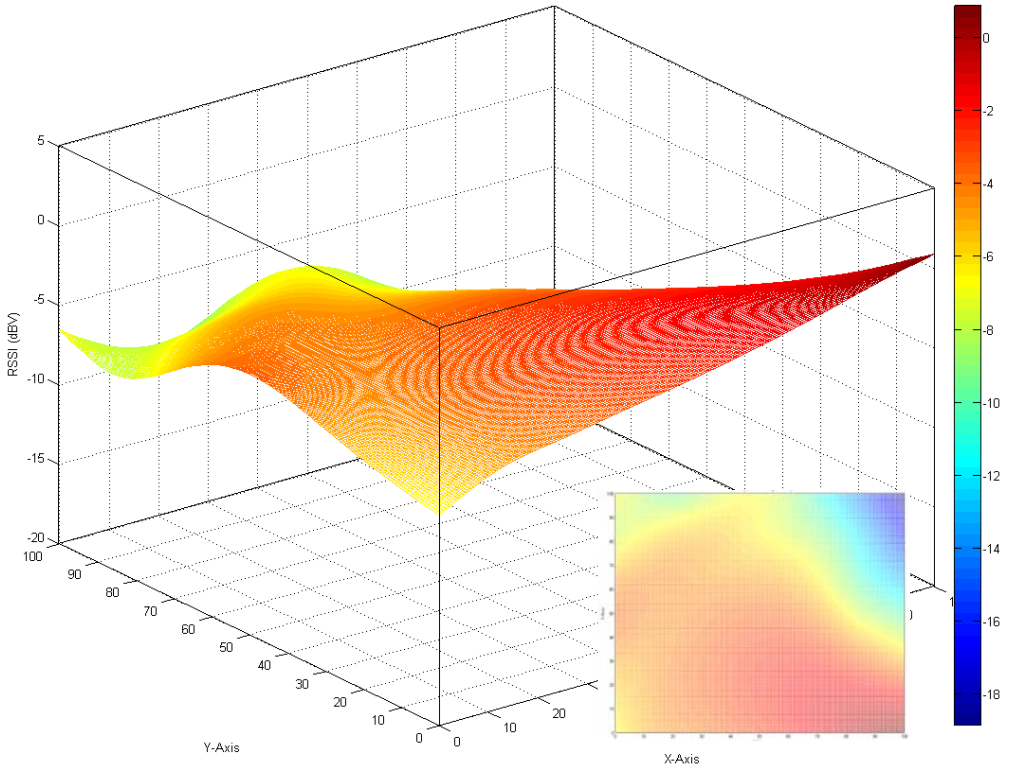

Figure F.5: Spline-fit of TX1's measured RSS at an angle of 27° in V. Inset shows top view.

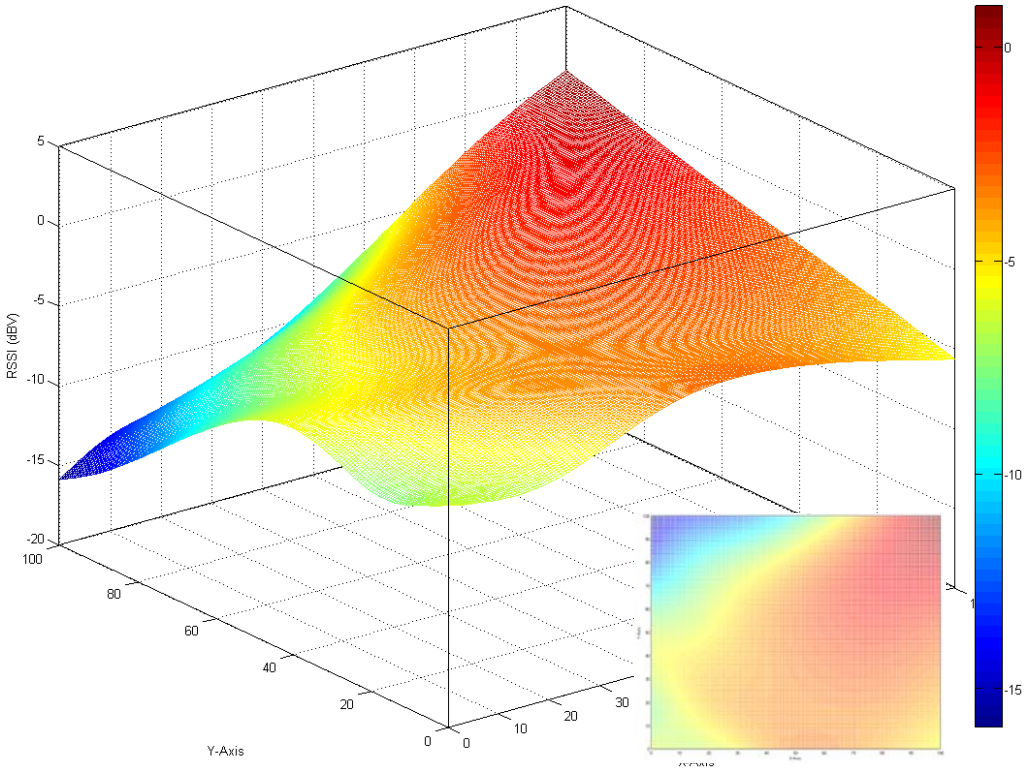

Figure F.6: Spline-fit of TX2's measured RSS at an angle of 27° in V. Inset shows top view.

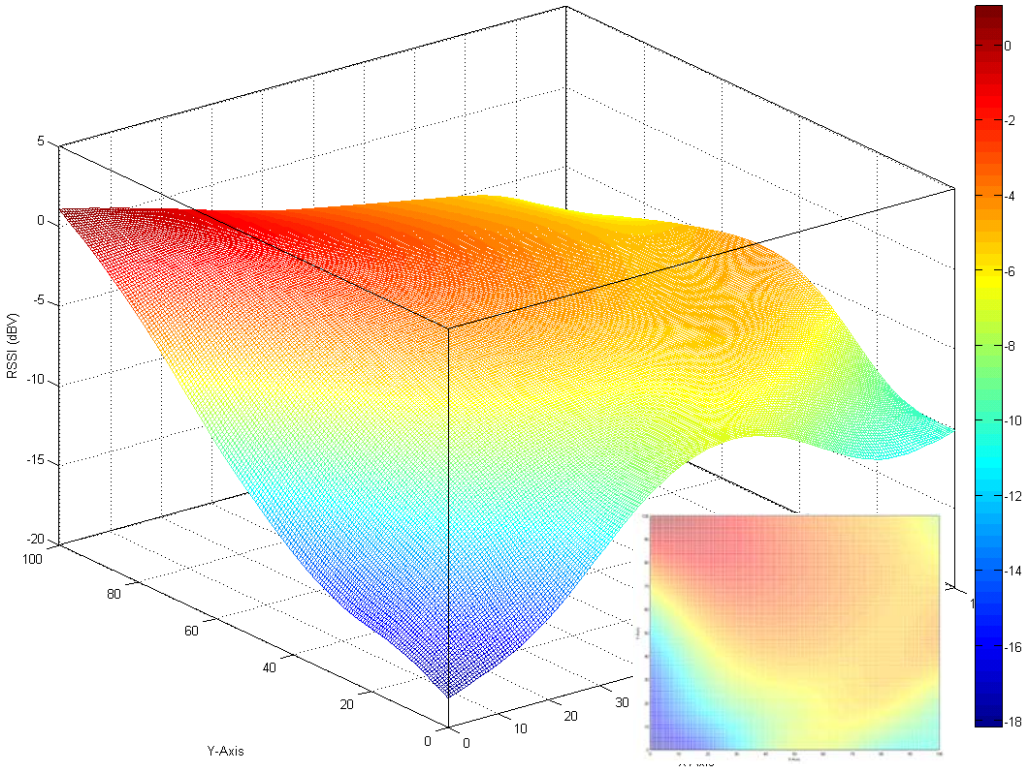

Figure F.7: Spline-fit of TX3's measured RSS at an angle of 27° in V. Inset shows top view.

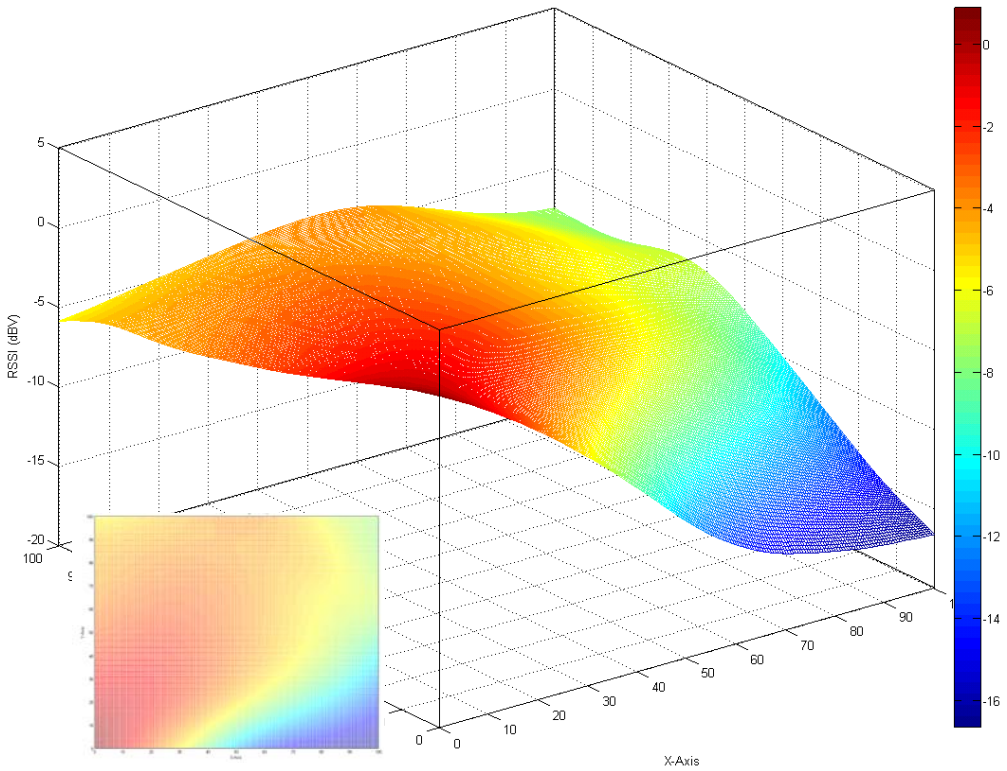

Figure F.8: Spline-fit of TX4's measured RSS at an angle of 27° in V. Inset shows top view.

APPENDIX G Surface plots of measured RSS and spline-fit of the four transmitters on Siepel mm-wave absorber mounted with AT6010H horn antennas at 27° (in dBV)

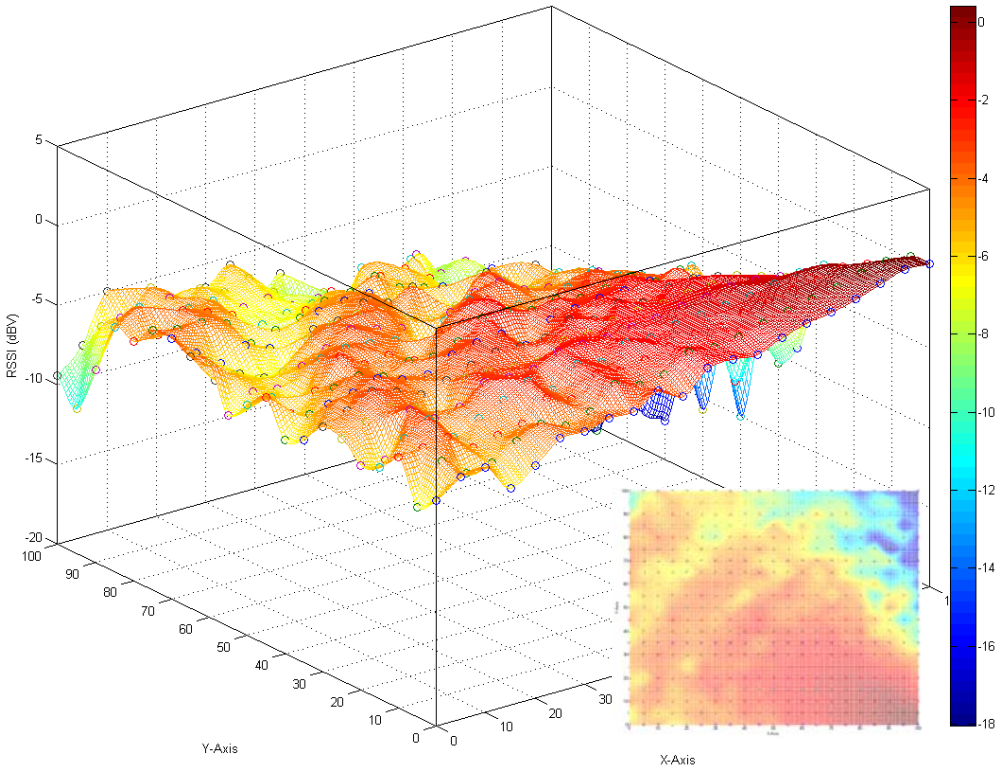

Figure G.1 Surface plot of TX1's measured RSS on Siepel mm-wave absorber at an angle of 27° in dBV. Inset shows top view.

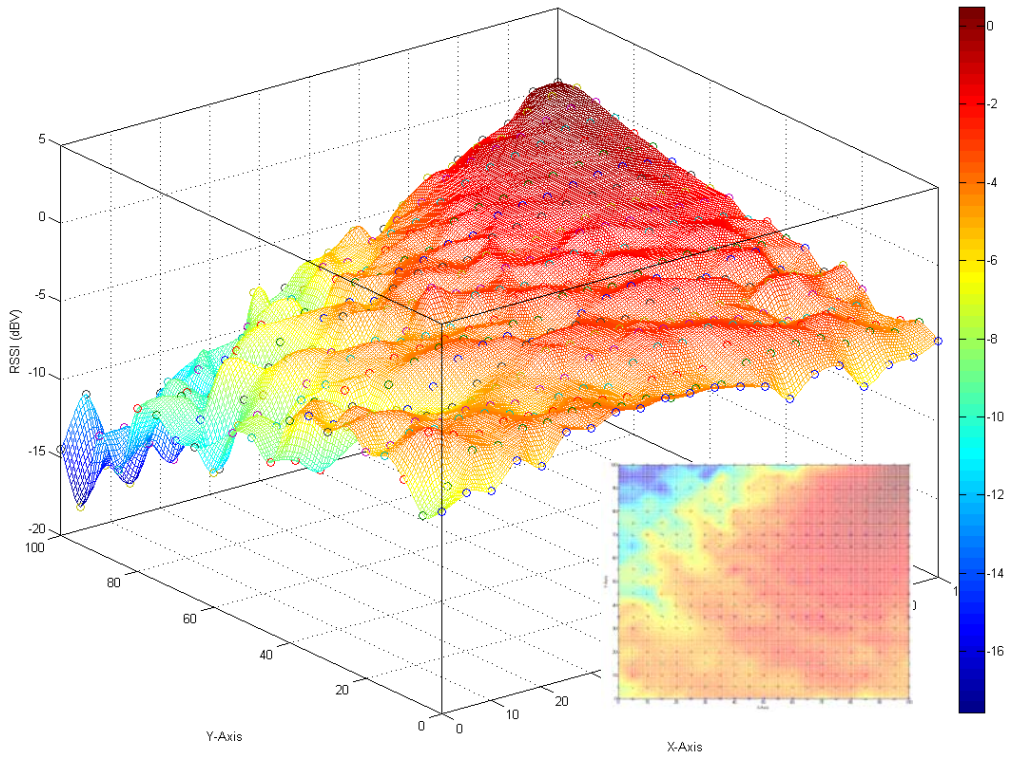

Figure G.2 Surface plot of TX2's measured RSS on Siepel mm-wave absorber at an angle of 27° in dBV. Inset shows top view.

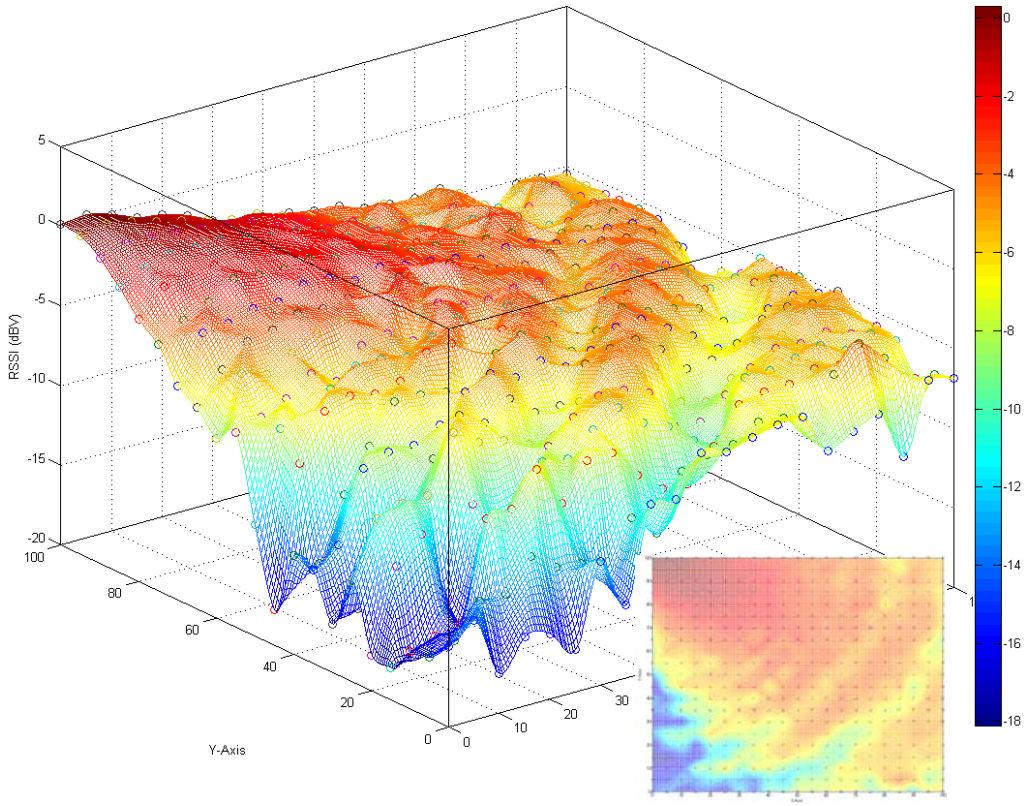

Figure G.3 Surface plot of TX3's measured RSS on Siepel mm-wave absorber at an angle of 27° in dBV. Inset shows top view.

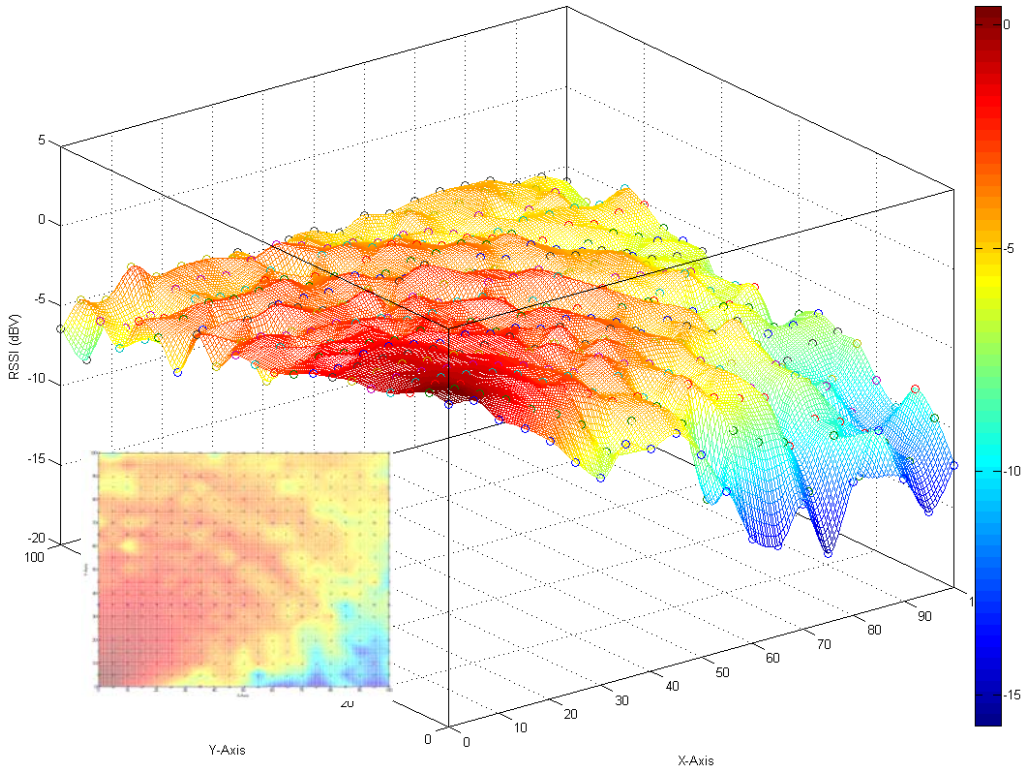

Figure G.4 Surface plot of TX4's measured RSS on Siepel mm-wave absorber at an angle of 27° in dBV. Inset shows top view.

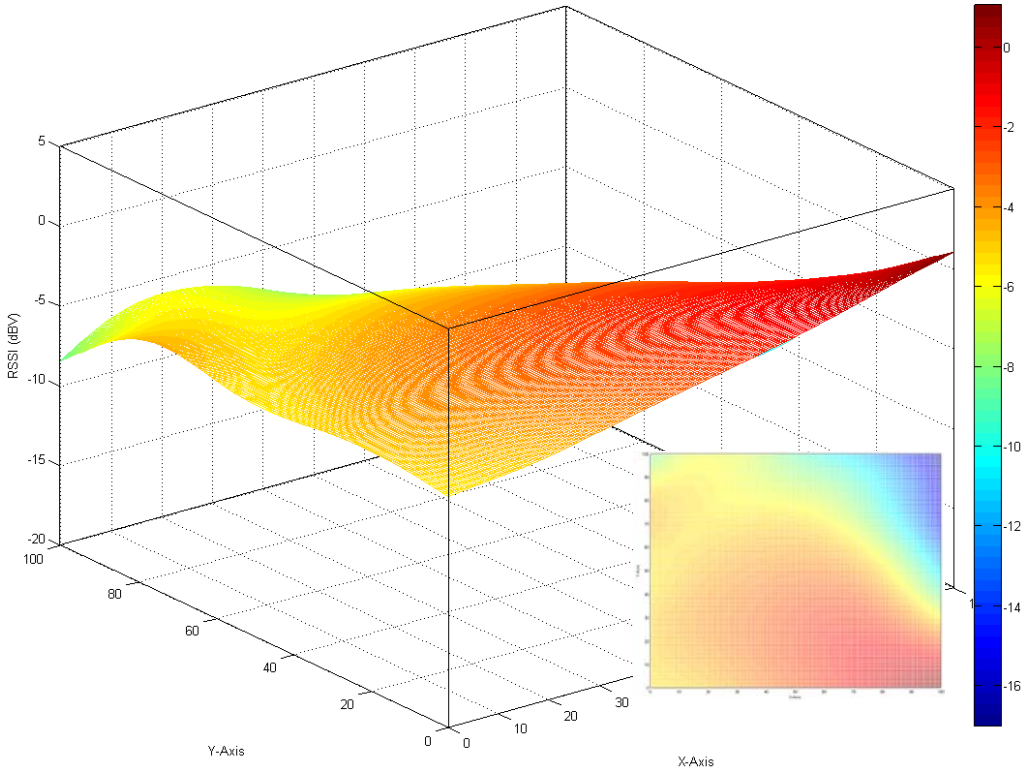

Figure G.5 Spline-fit of TX1's measured RSS on Siepel mm-wave absorber at an angle of 27° in dBV. Inset shows top view.

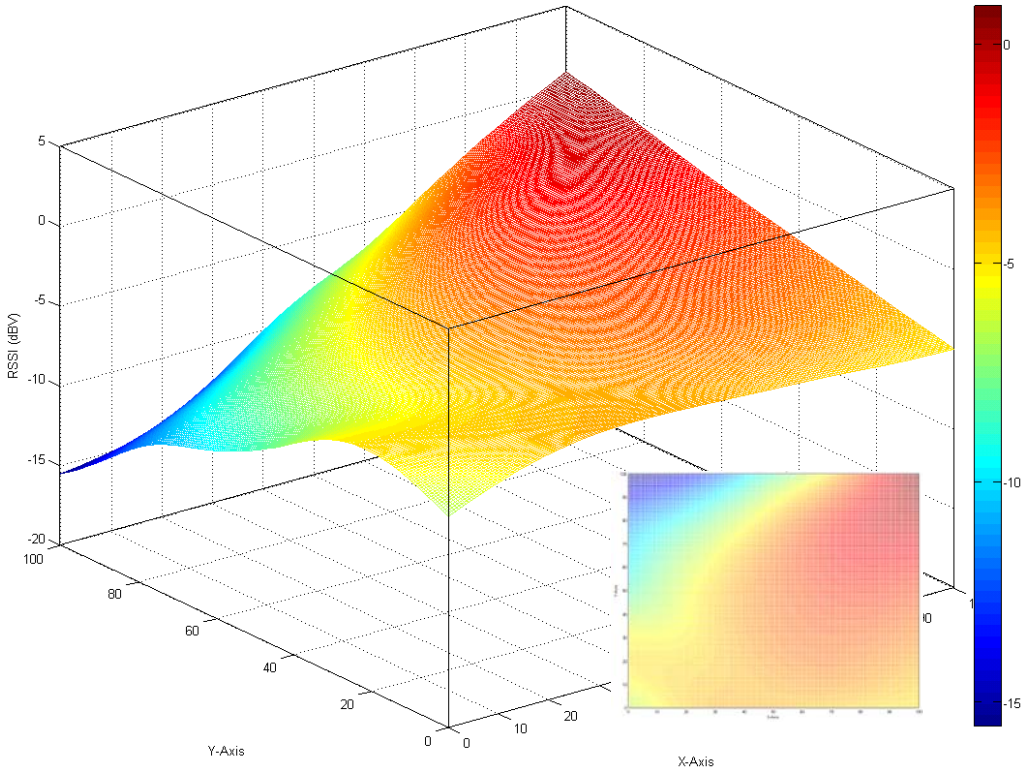

Figure G.6 Spline-fit of TX2's measured RSS on Siepel mm-wave absorber at an angle of 27° in dBV. Inset shows top view.

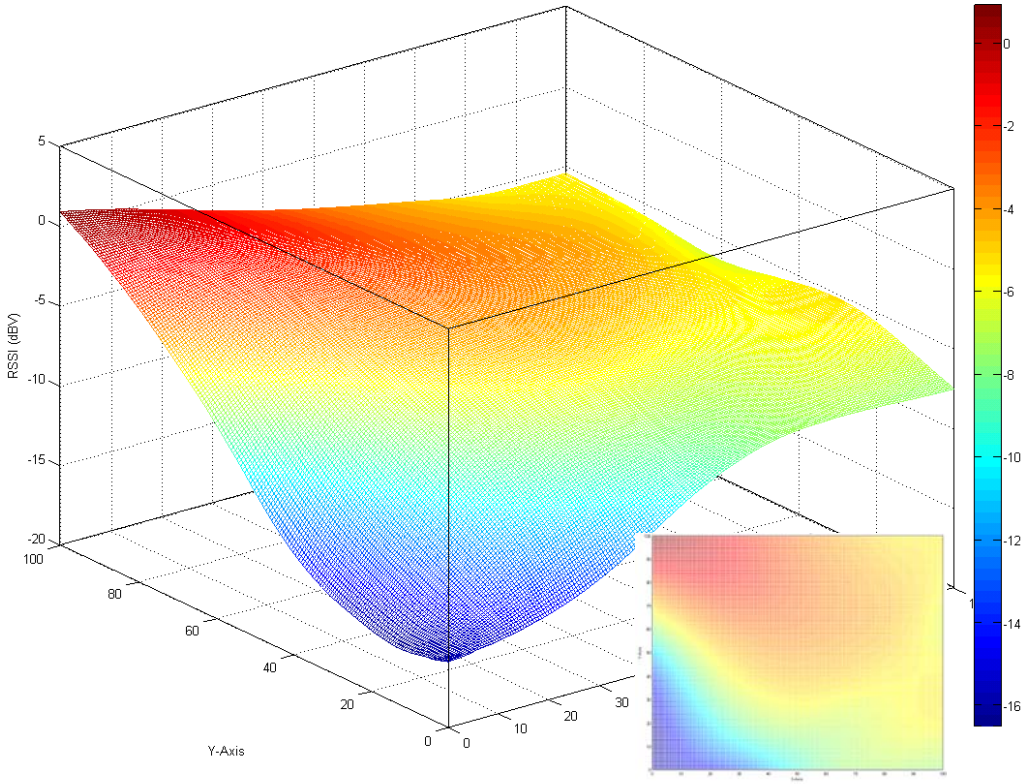

Figure G.7 Spline-fit of TX3's measured RSS on Siepel mm-wave absorber at an angle of 27° in dBV. Inset shows top view.

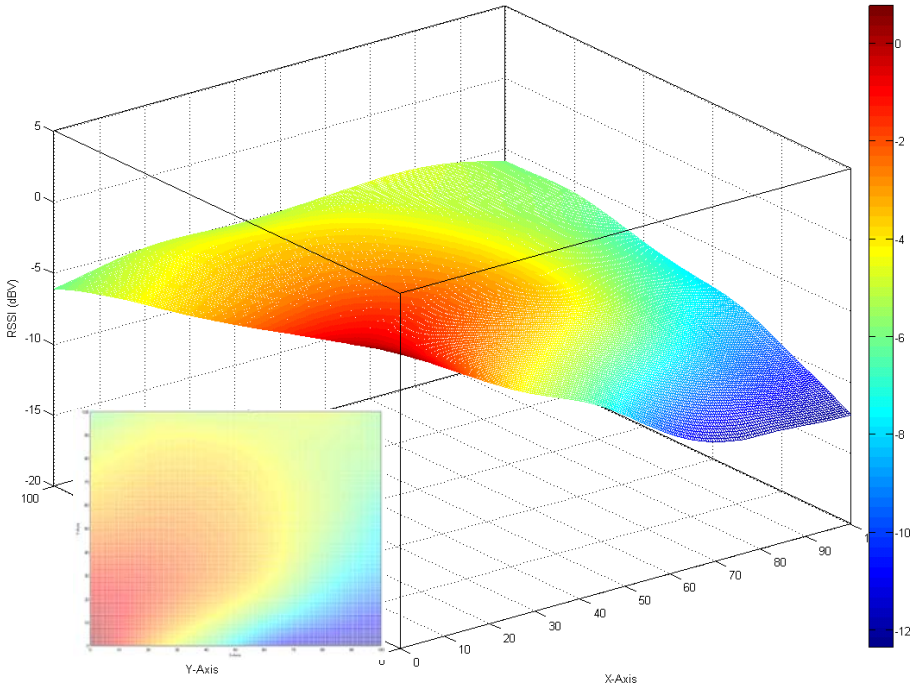

Figure G.8 Spline-fit of TX4's measured RSS on Siepel mm-wave absorber at an angle of 27° in dBV. Inset shows top view.